MODELING THE AVIAN CIRCADIAN SYSTEM WITH COUPLED NONLINEAR OSCILLATORS

A Dissertation
Presented to the Faculty of the Graduate School
of Cornell University
in Partial Fulfillment of the Requirements for the Degree of
Doctor of Philosophy

by

Kevin Robert Rompala

August 2008

MODELING THE AVIAN CIRCADIAN SYSTEM WITH COUPLED NONLINEAR OSCILLATORS

Kevin Robert Rompala, Ph.D.

Cornell University 2008

In this dissertation we propose several different qualitative mathematical models for the circadian system of the Japanese quail and investigate the dynamical behavior exhibited by each model via perturbation methods and numerical integration.

Each model consists of two identical (i.e. having the same natural frequency) nonlinear oscillators, x and y, and a third nonlinear oscillator, w, whose natural frequency is allowed to vary slightly from that of the other oscillators. The x- and y-oscillators are indirectly coupled via the w-oscillator, that is they form a 3-oscillator chain.

The first proposed model consists of three weakly coupled weakly-nonlinear ($\epsilon \ll 1$) van der Pol (VDP) oscillators and is given by

$$\begin{aligned} \ddot{x} - \epsilon\left(1 - x^2\right)\dot{x} + x &= \epsilon\mu\left(w - x\right) \\ \ddot{y} - \epsilon\left(1 - y^2\right)\dot{y} + y &= \epsilon\mu\left(w - y\right) \\ \ddot{w} - \epsilon\left(1 - w^2\right)\dot{w} + (1 + \epsilon\delta)^2 w &= \epsilon\mu\left(x + y - 2w\right) \end{aligned}$$

where the parameters δ and μ represent the detuning of the w-oscillator's frequency and the coupling strength between the oscillators respectively. The coupling and detuning in this system are considered "weak" as they are $O(\epsilon)$.

Next we propose two coupled phase oscillator models suggested by, but not derivable from, the VDP model. The first coupled phase oscillator system is given

by

$$
\begin{aligned}
\dot{\phi}_1 &= \frac{\mu}{2}\left[\cos\phi_2 - 1\right] - \delta \\
\dot{\phi}_2 &= \frac{\mu}{2}\left[\cos\phi_1 - 1\right] - \delta
\end{aligned}
$$

and the second by

$$
\begin{aligned}
\dot{\phi}_1 &= \frac{\mu}{2}\left[\frac{1}{A}\cos\phi_2 + (\frac{1}{A} - A)\cos\phi_1 - 1\right] - \delta \\
\dot{\phi}_2 &= \frac{\mu}{2}\left[\frac{1}{A}\cos\phi_1 + (\frac{1}{A} - A)\cos\phi_2 - 1\right] - \delta
\end{aligned}
$$

where ϕ_1 and ϕ_2 are the phase-differences between the w- and x- and w- and y- oscillators respectively. The first model is a special case of the second when $A = 1$ and therefore the second model can be considered a generalization of the first.

We then return to the VDP model but now consider the coupling and detuning as "strong" as they are $O(1)$. Finally we make a mathematical aside by investigating the presence of a 3:1 internal resonance in a system of two strongly coupled VDP oscillators.

The motivation for this work comes from the presence of circadian melatonin rhythms in the eyes of Japanese quail. Recent experiments showing these rhythms to be in-phase with each other and stable have strengthened the hypothesis that the eyes are the location of the central pacemaker for Japanese quail. We model these rhythms as the identical x- and y- oscillators, while the extra-ocular circadian system is modeled by the w-oscillator.

Mathematically we identify these stable phase-locked in-phase biological ocular melatonin rhythms with stable phase-locked in-phase modes for each model under study and then investigate the existence and stability of such motions for some set of parameter values. If such motions do exist for a model we conclude that the model in question exhibits behavior similar to that of the experiments. Our hope is that our results from these simple models might raise new questions for experimental biologists to investigate in a laboratory setting.

BIOGRAPHICAL SKETCH

Kevin Robert Rompala was born on December 12, 1980 in Berwyn, Illinois. He graduated from Lake Park High School in Roselle, IL in 1999 and received his Bachelor of Science degree in Systems Science & Engineering from Washington University in St. Louis in May 2003. In May 2006 he received a Master of Science degree from Cornell University. On October 6, 2007 he married his princess, Kathryn Reynold Stull, in Portland, Oregon.

This dissertation is dedicated to my princess.

ACKNOWLEDGMENTS

I would like to thank my dissertation advisor and committee chairman, Richard Rand, for all his support and encouragement during the last five years (and especially during these last five weeks). His patience with a graduate student whose research progresses on multiple timescales is greatly appreciated. I would also like to thank Steven Strogatz and Howard Howland for serving on my committee. Finally I would like to thank the faculty, staff, and my fellow graduate students in the Department of Theoretical & Applied Mechanics at Cornell University for everything else that made my graduate school experience what it was.

Table of Contents

List of Figures

List of Tables

Chapter 1
Introduction and Overview

In this dissertation we propose several different qualitative mathematical models for the circadian system of the Japanese quail and investigate the dynamical behavior exhibited by each model. We then synthesize our findings in the context of recent experimental results [22] to determine the appropriateness of each model. Our models are mathematical idealizations of the avian circadian system, derived not from biochemical fundamentals but chosen for their relative mathematical simplicity. Our hope is that our results might raise new questions for experimental biologists to investigate in the laboratory.

The Avian Circadian System

The circadian systems of all avian species consist of three primary oscillators (see Figure 1.1) – the ocular biological clocks in each eye that drive rhythmic melatonin production, the pineal gland which also rhythmically produces and secretes melatonin into the bloodstream, and a putative hypothalamic oscillator (here on referred to as the SCN, or suprachiasmatic nucleus) that most likely acts through neural signals (see [28] for review).

Experimental evidence suggests the relative importance of these oscillators as pacemakers in avian circadian systems varies from species to species. For example, in the house sparrow the pineal appears to be the only source of melatonin secretion into the bloodstream as pinealectomy (i.e. the complete removal of the pineal gland) abolishes all melatonin rhythms in the bloodstream, as well as many behavioral rhythms [9]. In other birds such as the Japanese quail the eyes are also sources of melatonin secretion into the bloodstream [27] since pinealectomy does not abolish body temperature rhythms, but complete enucleation (i.e. the complete

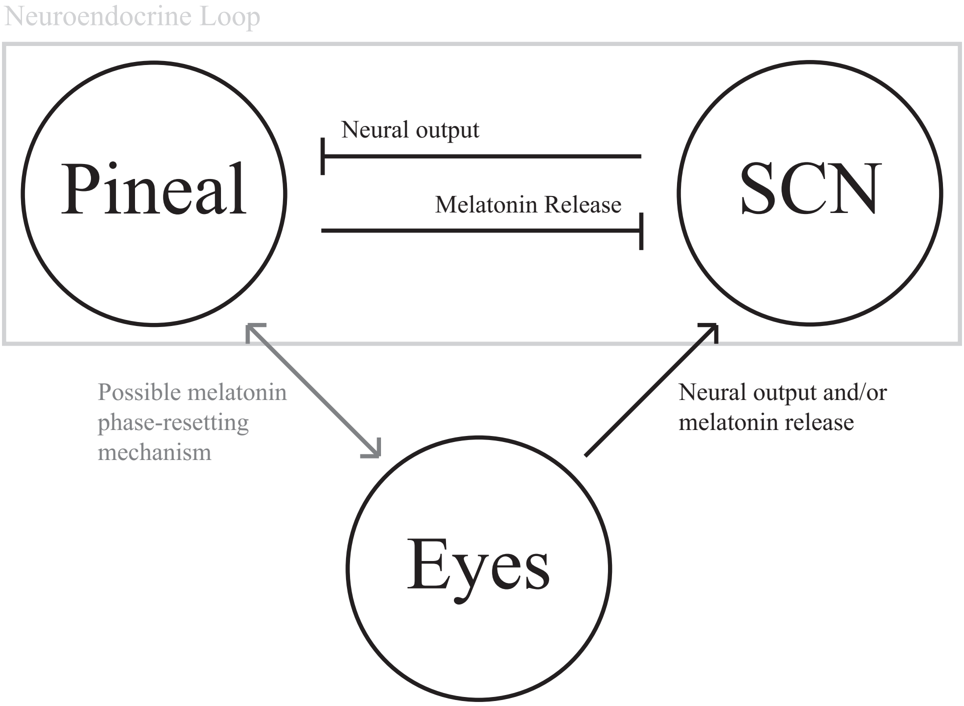

Figure 1.1: The circadian systems of all avian species consist of three primary oscillators [28] – the ocular biological clocks in each eye that drive rhythmic melatonin production, the pineal gland which also rhythmically produces and secretes melatonin into the bloodstream, and the SCN that most likely acts through neural signals. The pineal gland and SCN have been conjectured to be coupled together in a co-inhibitory "neuroendocrine loop" [2].

removal of the eyeballs) does [22]. Finally, in some birds such as the pigeon both pinealectomy and enucleation are necessary to abolish behavioral rhythms [28].

In terms of the organization of the avian circadian system, the pineal gland and SCN have been conjectured to be coupled together in a "neuroendocrine loop" [2] in which "a daily melatonin output from the pineal is required to maintain rhythmicity in the SCN, and a daily neural output from the SCN is required to maintain rhythmicity in the pineal." [22] That is, experimental results have indicated [28] that the respective rhythms of the pineal and SCN would damp out if not for the coupling between them. This relationship between the pineal and SCN is co-inhibitory – during the night the pineal produces and secretes melatonin into the bloodstream which inhibits SCN activity and during the day the SCN inhibits the production of melatonin by the pineal through neural signals. Such a relationship between the two oscillators should result in their respective rhythms being 180 degrees out-of-phase. Recent work on a mathematical model for the neuroendocrine loop in which the two oscillators are modeled as delay-coupled damped linear oscillators agrees with this [29].

In the Japanese quail complete enucleation abolishes body temperature rhythms thought to be controlled by the SCN [22]. Therefore in this species it appears that the ocular melatonin rhythms are *essential* for the sustainment of circadian rhythms in the SCN. This is most likely accomplished through both neural (the nature of which is still unknown) and hormonal outputs as severing the optic nerve only produces arrhythmia in approximately 25% of Japanese quail undergoing the procedure [22].

Recent experiments [22] have strengthened the conclusion that the ocular circadian rhythms in Japanese quail are the central pacemakers for their entire circadian system. Steele, et al. state [22]

> ...if the eyes are indeed the major circadian pacemakers in this system, the two ocular pacemakers in an individual bird must remain in phase with each other in prolonged DD [constant darkness]. If the two ocular pacemakers do not maintain phase, it would be difficult to argue that they are responsible for driving the robust, persistent body temperature rhythm that is characteristic of quail free-running in DD.

We note two of their experimental results in particular. First, when allowed to free-run in constant darkness for a period of over 40 days the melatonin levels in the eyes remained in-phase [22]. Secondly, when light-loaded (i.e. when the eyes are alternatingly covered by a patch to force their respective melatonin levels out-of-phase with each other) for 7 days and then placed in constant darkness the ocular melatonin rhythms regain their normal in-phase relationship within 5 days [22]. These results indicate robust stability properties for the in-phase ocular melatonin rhythms.

Modeling the Avian Circadian System

We propose a model of the avian circadian system under free-running conditions consisting of the three primary oscillators – the ocular biological clocks in each eye that drive rhythmic melatonin production and the neuroendocrine loop consisting of the pineal and SCN, and couple them together via the secretion of melatonin into the bloodstream. We combine the rhythmic melatonin production of the neuroendocrine loop and the melatonin in the bloodstream into a single "extra-ocular" oscillator and hypothesize that the ocular circadian rhythms are indirectly coupled via this extra-ocular oscillator (see Figure 1.2). While the true nature of the ocular coupling is unknown, the retinae possess melatonin receptors and so one could hypothesize that "if the eyes are driven out of phase, daily melatonin release by the eyes (or pineal) may cause mutual phase advances or delays of the two ocular pacemakers until they regain their normal phase relationship." [22] Note that we ignore any potential neural coupling between the eyes and the SCN since this would require the neuroendocrine loop be modeled as two distinct damped oscillators.

We propose 4 different mathematical models for the free-running behavior of the avian circadian system. In each model we identify the ocular melatonin rhythms with identical (i.e. having the same natural frequency) oscillators, x and y, and the extra-ocular system with a third oscillator, w, whose natural frequency is allowed to vary slightly from that of the ocular oscillators. The detuning of the w-oscillator

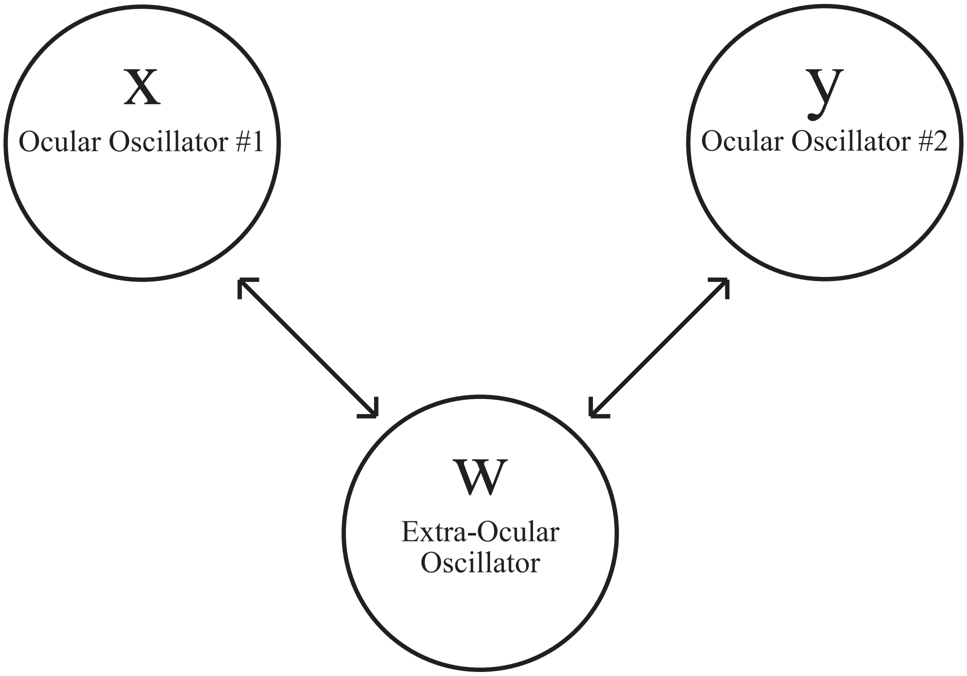

Figure 1.2: Model of avian circadian system under free-running conditions used in this dissertation. We identify the ocular melatonin rhythms with identical oscillators, x and y, and the extra-ocular system with a third oscillator, w, whose natural frequency is allowed to vary slightly from that of the ocular oscillators. The ocular rhythms are indirectly coupled together via the extra-ocular system. The extra-ocular system combines the rhythmic melatonin production of the neuroendocrine loop with the melatonin in the bloodstream to form a single oscillator.

is controlled by the parameter δ (or Δ in CHAPTER 5). We refer to the amplitudes and phases of these oscillators as R_1, R_2, R_3 and $\theta_1, \theta_2, \theta_3$ respectively. The x- and y-oscillators are indirectly coupled via the w-oscillator (see Figure 1.2). That is, they form a 3-oscillator chain. The strength of coupling between the oscillators is controlled by the parameter μ.

The first proposed model ([18], [19], [20]) consists of coupled weakly-nonlinear ($\epsilon \ll 1$) van der Pol (VDP) oscillators. VDP oscillators, as opposed to more general limit-cycle oscillators, were chosen because they are well-known and have been used for a wide range of biological modeling, including, but not limited to, modeling the human circadian timing system [13], ocular melatonin rhythms coupled via a non-oscillatory bloodstream [1], and neural patterns in jellyfish locomotion [12]. Furthermore, it has been shown [1] that with a few simple assumptions the biochemical basis of a circadian rhythm in free-running conditions can be reduced to such an oscillator with constant forcing. The system is given by

$$\begin{aligned} \ddot{x} - \epsilon\left(1 - x^2\right)\dot{x} + x &= \epsilon\mu\left(w - x\right) \\ \ddot{y} - \epsilon\left(1 - y^2\right)\dot{y} + y &= \epsilon\mu\left(w - y\right) \\ \ddot{w} - \epsilon\left(1 - w^2\right)\dot{w} + (1 + \epsilon\delta)^2 w &= \epsilon\mu\left(x + y - 2w\right) \end{aligned} \tag{1.1}$$

The coupling and detuning in this system are considered "weak" as they are $O(\epsilon)$. The decision to couple the oscillators via amplitudes and not velocities (or a combination of both) was made in agreement with earlier work ([24], [5], [1]) as we do not know of any biological arguments for choosing one over the other.

The mathematical complexity of weakly coupled VDP oscillators leads us to next propose two phase oscillator models suggested by, but not derivable from, (1.1). For the first model we assume the amplitudes of the three coupled VDP oscillators are equal to their approximate uncoupled amplitudes, that is $R_1 = R_2 = R_3 = 2$. The resulting phase oscillator system is given by

$$\begin{aligned} \dot{\phi}_1 &= \frac{\mu}{2}\left[\cos\phi_2 - 1\right] - \delta \\ \dot{\phi}_2 &= \frac{\mu}{2}\left[\cos\phi_1 - 1\right] - \delta \end{aligned} \tag{1.2}$$

where $\phi_1 = \theta_3 - \theta_1$ and $\phi_2 = \theta_3 - \theta_2$ are the phase-differences between the w- and x- and w- and y-oscillators respectively.

The second phase oscillator system is given by

$$\begin{aligned}\dot{\phi}_1 &= \frac{\mu}{2}\left[\frac{1}{A}\cos\phi_2 + (\frac{1}{A} - A)\cos\phi_1 - 1\right] - \delta \\ \dot{\phi}_2 &= \frac{\mu}{2}\left[\frac{1}{A}\cos\phi_1 + (\frac{1}{A} - A)\cos\phi_2 - 1\right] - \delta\end{aligned} \tag{1.3}$$

This system is a generalization of (1.2) in that we no longer assume $R_1 = R_2 = R_3 = 2$ but instead treat the ratios of amplitudes as a new system parameter, i.e. $\frac{R_3}{R_1} = \frac{R_3}{R_2} = A$. Note that (1.2) is a special case of (1.3) when $A = 1$.

Finally, we return to the original VDP oscillator model (1.1) and reinvestigate it for a different parameter regime. Our motivation comes from previous work on systems of two weakly coupled ([4],[5]) and two strongly coupled ([23], [24]) VDP oscillators indicating that a perturbation analysis on a strongly coupled system should be less mathematically complex. This system is given by

$$\begin{aligned}\ddot{x} - \epsilon(1 - x^2)\dot{x} + x &= \mu(w - x) \\ \ddot{y} - \epsilon(1 - y^2)\dot{y} + y &= \mu(w - y) \\ \ddot{w} - \epsilon(1 - w^2)\dot{w} + (1 + \Delta)w &= \mu(x + y - 2w)\end{aligned} \tag{1.4}$$

where the frequency of the w-oscillator is now defined as $\sqrt{1 + \Delta}$ and the coupling and detuning are now considered "strong" as they are $O(1)$.

For each system we want to ascertain whether it exhibits behavior like that found in the experiments. We identify the stable in-phase melatonin rhythm of the ocular oscillators with an exact solution called the in-phase mode, given by $x(t) = y(t) = f(t)$ for the VDP models and $\phi_1(t) = \phi_2(t) = \phi(t)$ for the phase oscillator models. The hypothesis that the ocular oscillators are the primary pacemakers for the Japanese quail's circadian system narrows our interest to in-phase modes that are phase-locked to the w-oscillator. The light-loadings performed in the laboratory to force the ocular melatonin rhythms approximately 180 degrees out-of-phase translate into initial conditions lying outside the in-phase subspace (defined by $x(t) = y(t)$ or $\phi_1(t) = \phi_2(t)$). The experimental result that the ocular oscillators eventually return to their original in-phase rhythm suggests that the corresponding phase-locked in-phase mode in the models be stable for some set of parameter values. Thus our criteria for a model to exhibit behavior like that found in the experiments is that it must exhibit a stable phase-locked in-phase mode for some set of parameter values.

Note that we could propose a stricter criteria for a model to exhibit behavior like that found in the experiments by also requiring that the model exhibit no other stable non-in-phase dynamical motions for parameters where a stable phase-locked in-phase mode exists. However, the experiments only indicate the existence of a stable in-phase ocular melatonin rhythm but not the non-existence of other possible stable motions. That is, we do not know that if the ocular melatonin rhythms were light-loaded to be 90 degrees out-of-phase they would not go to some other stable motion besides returning to an in-phase rhythm. Also, we do not require the existence of an out-of-phase mode in our models as we do not believe that light-loading is an accurate enough method to force the ocular melatonin rhythms into a true 180 degree out-of-phase motion, although we investigate the stability of out-of-phase modes when they do exist.

Dissertation Outline

We conclude this introduction by outlining the content of each chapter in this dissertation.

We begin in Chapter 2 by reviewing our earlier work ([18], [19], [20]) on the weakly coupled VDP system (1.1) where we investigated the dynamics in the in-phase subspace of (1.1). In Chapter 3 we complete the analysis on the phase-locked in-phase modes for (1.1) by investigating their stabilities outside the in-phase subspace via the perturbation results from Chapter 2 and numerical Floquet theory. We also investigate the existence and stability of out-of-phase modes for (1.1).

Next, in Chapter 4 we study the dynamics in the phase oscillator systems (1.2) and (1.3) and investigate the existence and stability of phase-locked in-phase modes for them. We ask whether these simpler systems can exhibit behavior qualitatively similar to (1.1).

In Chapter 5 we return to the VDP model of the circadian system and study the strongly coupled system (1.4) via the two-variable expansion perturbation method. Again we investigate the existence and stability of phase-locked in-phase modes. We also compare our bifurcation results for (1.4) with those for (1.1) and discuss the presence of internal resonances for (1.4).

In Chapter 6 we review earlier work ([23], [24]) on a system of two strongly coupled VDP oscillators before investigating the existence of an internal resonance for the system via the two-variable expansion perturbation method. We calculate an approximate boundary to the region of parameter space affected by the existence of this resonance.

Finally, we conclude this dissertation with a summary of our results in Chapter 7.

Chapter 2
Three Weakly Coupled VDP Oscillators

We begin this dissertation by reviewing our earlier work ([18],[19],[20]) on a model for the avian circadian system consisting of three weakly coupled VDP oscillators. The system is given by

$$\begin{aligned} \ddot{x} - \epsilon\left(1 - x^2\right)\dot{x} + x &= \epsilon\mu\left(w - x\right) \\ \ddot{y} - \epsilon\left(1 - y^2\right)\dot{y} + y &= \epsilon\mu\left(w - y\right) \\ \ddot{w} - \epsilon\left(1 - w^2\right)\dot{w} + (1 + \epsilon\delta)^2 w &= \epsilon\mu\left(x + y - 2w\right) \end{aligned} \tag{2.1}$$

The x- and y-oscillators have identical uncoupled natural frequencies of unity while the frequency of the w-oscillator is detuned by $\epsilon\delta$. A "dotted" quantity implies differentiation with respect to time t. The system depends on two parameters – μ, the coupling strength between the oscillators, and δ, the detuning of the w-oscillator's frequency. We assume $\mu > 0$ and $\epsilon \ll 1$. The coupling and detuning are considered "weak" as they are $O(\epsilon)$.

We are interested in the existence of stable phase-locked in-phase modes for (2.1). An in-phase mode for (2.1) will be an exact solution $x(t) = y(t) = f(t)$, $w(t) = g(t)$ living in the 4-dimensional invariant in-phase subspace of (2.1) defined by $x(t) = y(t)$, the flow in which is given by

$$\begin{aligned} \ddot{x} - \epsilon\left(1 - x^2\right)\dot{x} + x &= \epsilon\mu\left(w - x\right) \\ \ddot{w} - \epsilon\left(1 - w^2\right)\dot{w} + (1 + 2\epsilon\delta) w &= \epsilon 2\mu\left(x - w\right) \end{aligned} \tag{2.2}$$

A phase-locked in-phase mode will be a periodic solution for (2.2) (and thus (2.1) as well). In this chapter we investigate the existence of such motions and determine their stability within the in-phase subspace.

BIFURCATION AND STABILITY ANALYSIS

To investigate the existence and stability of these periodic motions we apply the two-variable expansion singular perturbation method to (2.1) to $O(\epsilon)$ (see CHAPTER 5 for a review of this perturbation method).

The resulting lowest-order asymptotic solutions to (2.1) are [19]

$$\begin{aligned} x_0(t) &= R_1(\eta)\cos(t-\theta_1(\eta)) \\ y_0(t) &= R_2(\eta)\cos(t-\theta_2(\eta)) \\ w_0(t) &= R_3(\eta)\cos(t-\theta_3(\eta)) \end{aligned}$$

where the amplitudes R_i and phases θ_i (for $i = 1, 2, 3$) are functionally dependent on slow-time $\eta = \epsilon t$. The slow-time evolution of the amplitudes and phases are given by the 5-dimensional slow-flow [19]

$$\begin{aligned} \frac{dR_1}{d\eta} &= -\frac{\mu R_3}{2}\sin\phi_1 + \frac{R_1}{2}\left(1-\frac{R_1^2}{4}\right) \\ \frac{dR_2}{d\eta} &= -\frac{\mu R_3}{2}\sin\phi_2 + \frac{R_2}{2}\left(1-\frac{R_2^2}{4}\right) \\ \frac{dR_3}{d\eta} &= \frac{\mu R_2}{2}\sin\phi_2 + \frac{\mu R_1}{2}\sin\phi_1 + \frac{R_3}{2}\left(1-\frac{R_3^2}{4}\right) \\ \frac{d\phi_1}{d\eta} &= \frac{\mu}{2}\left[\frac{R_2}{R_3}\cos\phi_2 + \left(\frac{R_1}{R_3}-\frac{R_3}{R_1}\right)\cos\phi_1 - 1\right] - \delta \\ \frac{d\phi_2}{d\eta} &= \frac{\mu}{2}\left[\frac{R_1}{R_3}\cos\phi_1 + \left(\frac{R_2}{R_3}-\frac{R_3}{R_2}\right)\cos\phi_2 - 1\right] - \delta \end{aligned} \tag{2.3}$$

where $\phi_1 = \theta_3 - \theta_1$ and $\phi_2 = \theta_3 - \theta_2$ are the phase-differences between the w- and x- and w- and y-oscillators respectively. The 3-dimensional in-phase slow-flow is found by substituting $R_1 = R_2$ and $\phi_1 = \phi_2 = \phi$ into (2.3) to get ([18], [19], [20])

$$\frac{dR_1}{d\eta} = -\frac{\mu R_3}{2}\sin\phi + \frac{R_1}{2}\left(1 - \frac{R_1^2}{4}\right) \tag{2.4}$$

$$\frac{dR_3}{d\eta} = \mu R_1 \sin\phi + \frac{R_3}{2}\left(1 - \frac{R_3^2}{4}\right) \tag{2.5}$$

$$\frac{d\phi}{d\eta} = \frac{\mu}{2}\left[\left(\frac{2R_1}{R_3} - \frac{R_3}{R_1}\right)\cos\phi - 1\right] - \delta \tag{2.6}$$

An equilibrium point of the in-phase slow-flow represents a periodic motion living in the in-phase subspace (2.2). Therefore questions on existence and stability of phase-locked in-phase modes for (2.2) reduce to a study on the existence and stability of equilibrium points for (2.4)-(2.6).

Unfortunately the nonlinear nature of the in-phase slow-flow equations does not allow us to solve for equilibrium points in closed-form. Instead we set the right-hand side of (2.4)-(2.6) equal to zero, and through algebraic manipulation of these equations in MACSYMA®, calculate analytic bifurcation curves in parameter space corresponding to saddle-node (or infinite-period) and Hopf bifurcations of in-phase slow-flow equilibrium points (see Appendix A for the derivations of these curves). We also numerically locate two other bifurcation curves corresponding to saddle-connection bifurcations and folds of limit cycles (see Figure 2.1).

DISCUSSION

Numerical integration of the in-phase slow-flow equations reveals three qualitatively different types of dynamical behavior exhibited by (2.1) – (1) in-phase phase drift, (2) weakly phase-locked in-phase motion, and (3) phase-locked in-phase motion. These motions are described as follows ([18],[19],[20]):

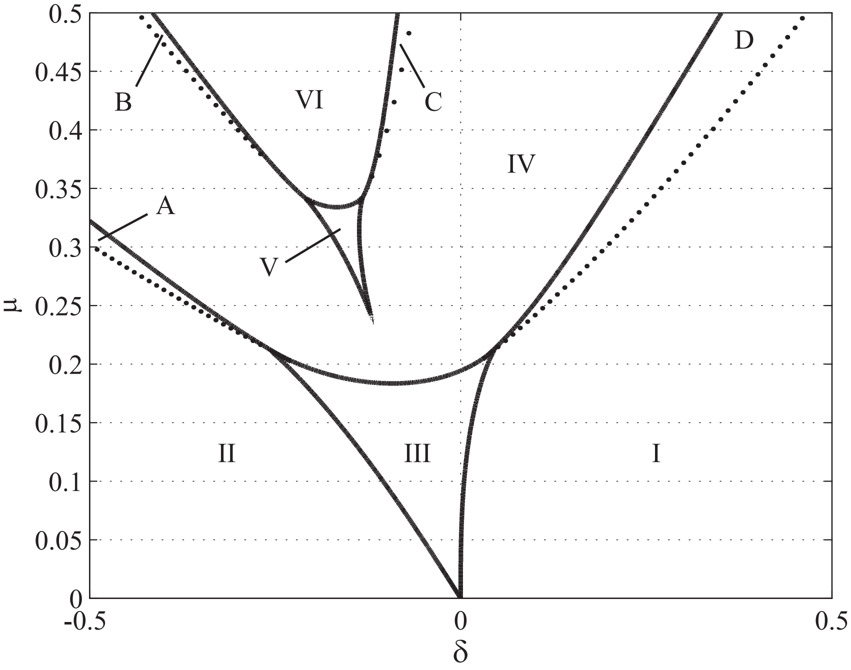

Figure 2.1: Bifurcation curves for the in-phase slow-flow (2.4)-(2.6) ([18],[19],[20]). Labels indicate regions of parameter space with distinct dynamical behavior (see Table 2.1). See Appendix A for derivations of analytic bifurcation curves. analytic saddle-node (or infinite-period) bifurcation curves = triangular region boundaries; analytic Hopf bifurcation curves = parabolic curves; numerical saddle-connection bifurcation curves = lower black dots; numerical limit-cycle fold bifurcation curves = upper black dots.

1. In-phase phase drift occurs when the phase difference $\phi(\eta)$ between the w-oscillator and the x- and y-oscillators increases (or decreases) without bound. In the in-phase slow-flow phase space this motion appears as a closed trajectory (a limit cycle) that is cyclic in ϕ (see Figure 2.2) and is referred to as an LCD.

2. A weakly phase-locked in-phase motion occurs when $\phi(\eta)$ is periodic. It is represented in the in-phase slow-flow phase space by a limit cycle that is topologically distinct from an LCD. Such motions are born in supercritical Hopf bifurcations or in folds of limit cycles and are referred to as LCW's.

3. A phase-locked in-phase mode is a motion where $\phi(\eta)$ remains constant. These motions correspond to equilibrium points in the slow-flow phase space.

The dynamical features of the in-phase slow-flow found in each distinct region (see Figure 2.1) of parameter space are summarized in Table 2.1.

We are interested in finding regions of δ-μ parameter space where stable phase-locked in-phase modes for (2.1) exist. However, in this chapter we have only investigated the dynamics found within the in-phase subspace (2.2). Therefore identifying regions of parameter space where stable equilibrium points of the in-phase slow-flow (2.4)-(2.6) exist does not provide sufficient information for us to make any conclusions about the appropriateness of the system (2.1) for modeling the experimental results. However, it does provide information about regions of parameter space that meet the necessary conditions for exhibiting stable phase-locked in-phase modes. That is, for a phase-locked in-phase mode to be stable it must be stable within the in-phase subspace.

From Table 2.1 we see that stable equilibrium points exist in Regions III, IV, V,

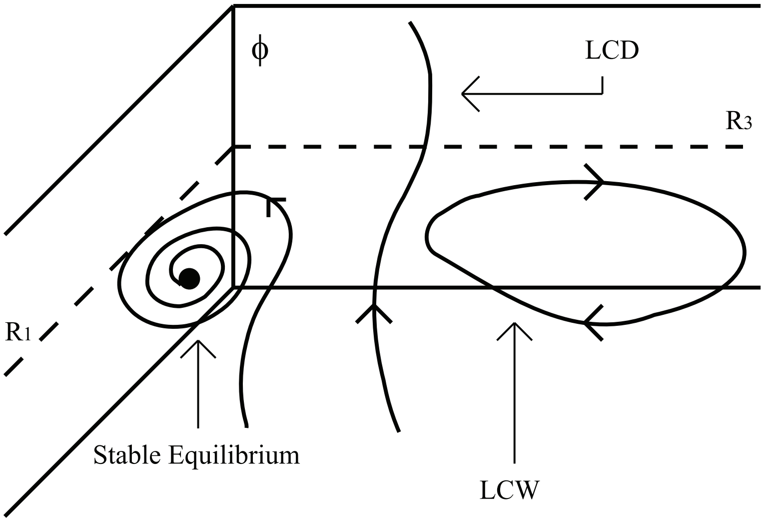

Figure 2.2: Three distinct types of dynamical features found in the in-phase slow-flow ([18],[19],[20]).

Table 2.1: Description of dynamical features of the in-phase slow-flow found in different regions (see Figure 2.1) of parameter space ([18],[19],[20]).

Region	Dynamical Features
I	Two unstable equilibrium points and one stable LCD.
II	Two unstable equilibrium points and one stable LCD.
III	One stable and three unstable equilibrium points.
IV	One stable and one unstable equilibrium point.
V	Two stable and two unstable equilibrium points.
VI	Two stable equilibrium points and an unstable LCD.
A & D	Two unstable equilibrium points and a stable LCW.
B & C	One stable and one unstable equilibrium point, a stable LCW, and an unstable LCD/LCW.

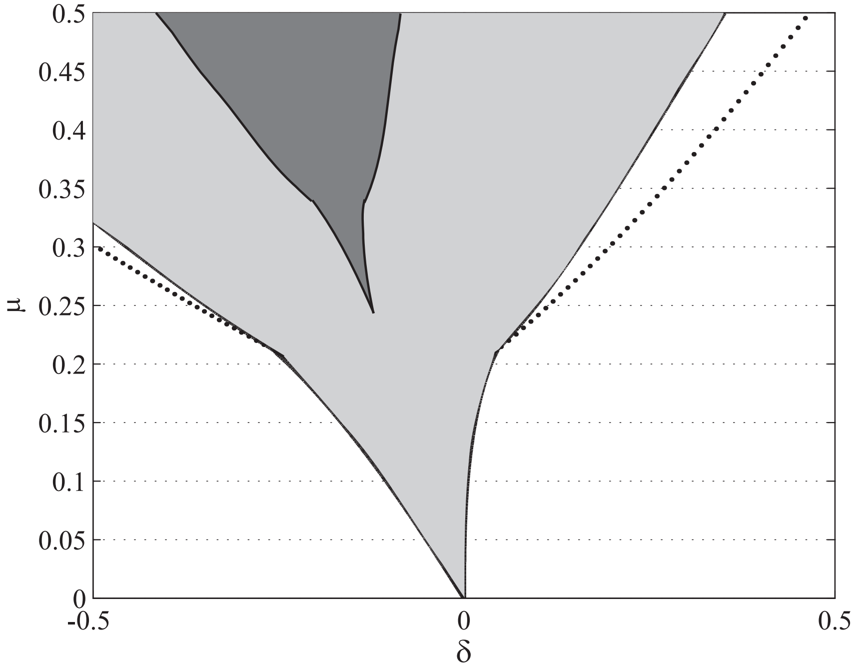

Figure 2.3: Regions of δ-μ parameter space where stable equilibrium points of the in-phase slow-flow exist ([18],[19],[20]). These regions satisfy the necessary condition for the existence of stable phase-locked in-phase modes for (2.1). light gray = 1 stable equilibrium point; dark gray = 2 stable equilibrium points.

VI, B, and C (see Figure 2.3). For a given coupling strength μ stable phase-locked in-phase modes can exist only if the frequency detuning δ is within a certain interval. Inversely, given a frequency detuning δ there exists a minimum coupling strength μ such that stable phase-locked in-phase modes can exist.

Note that in Regions V, VI, B, and C multiple stable phase-locked in-phase modes for (2.2) exist. These regions appear to exist exclusively for parameter values where the x- and y-oscillators have a higher natural frequency (and thus shorter period) than the w-oscillator. That is, they appear to exist only when $\delta < 0$. Biologically this would imply that the ocular melatonin rhythms should have a slightly shorter period of oscillation than the extra-ocular system ([18],[19],[20]). Also, the existence of multiple stable phase-locked in-phase modes indicates a dependence on initial conditions for which phase-locked in-phase mode the system eventually tends to. This would suggest that in future experiments multiple light-loadings be performed to place the ocular melatonin rhythms into different non-in-phase motions and not just 180 degree out-of-phase motion.

Chapter 3
Three Weakly Coupled VDP Oscillators: Stability of In-Phase and Out-of-Phase Modes

In Chapter 2 the scope of our work, including stability results, was limited to within the in-phase subspace (2.2). Unfortunately this is not sufficient to determine whether the weakly coupled and detuned VDP system (2.1) exhibits behavior like that found in the experiments. To make this determination we now investigate the stability of phase-locked in-phase modes for (2.1) in the full phase space.

We begin by investigating the stability of in-phase slow-flow equilibrium points via algebraic manipulation of the 5-dimensional slow-flow (2.3). Afterwards we verify our perturbation results via numerical integration of the original system (2.1) and Floquet theory. The result will be a reduced region of parameter space (from that shown in Figure 2.3) where we predict stable phase-locked in-phase modes to exist. Next we perform a numerical stability analysis on the out-of-phase mode and find that it is unstable for all parameter values under consideration. Finally we interpret our results within the context of the original experiments.

Stability Results via Perturbation Analysis

To investigate the full stability of a phase-locked in-phase mode let $(R_1, R_2, R_3, \phi_1, \phi_2) = (r_1, r_1, r_3, \phi, \phi)$ represent an undetermined in-phase slow-flow equilibrium point for the 5-dimensional slow-flow (2.3). We ask for what parameter values will this equilibrium point be stable. The linearization of the slow-flow in the neighborhood of this equilibrium point is given by the Jacobian matrix evaluated at this point. The characteristic polynomial of the Jacobian is of the form

$$\lambda^5 + c_4\lambda^4 + c_3\lambda^3 + c_2\lambda^2 + c_1\lambda + c_0 = 0 \tag{3.1}$$

where the coefficients c_i for $i = 0 \ldots 4$ are functions of r_1, r_3, and ϕ. The equilibrium point will be stable when all 5 roots of (3.1) have negative real parts. It will become unstable when either (1) an eigenvalue crosses the origin on the real axis or (2) a pair of complex eigenvalues crosses the imaginary axis.

An eigenvalue crosses the origin on the real axis when $\lambda = 0$ is a root of (3.1), i.e. $c_0 = 0$. We eliminate ϕ from this expression by solving (2.6) for $\cos\phi$ and then by multiplying (2.5) by r_1, subtracting from it r_3 times (2.4), and solving for $\sin\phi$ to get, respectively,

$$\cos\phi = \frac{-\left(\mu + 2\delta\right) r_1 r_3}{\mu\left(r_3^2 - 2r_1^2\right)} \tag{3.2}$$

$$\sin\phi = \frac{r_1 r_3 \left(r_3^2 - r_1^2\right)}{4\mu\left(r_3^2 + 2r_1^2\right)} \tag{3.3}$$

The resulting equation in terms of r_1 and r_3 only is

$$\begin{aligned}
&r_3^2 \left(3r_1^2r_3^6 - 4r_3^6 - 15r_1^4r_3^4 + 20r_1^2r_3^4 - 16\mu^2r_3^4 - 64\delta\mu r_3^4 - 64\delta^2r_3^4 + 24r_1^6r_3^2\right.\\
&\left.-32r_1^4r_3^2 - 32\mu^2r_1^2r_3^2 - 128\delta\mu r_1^2r_3^2 - 128\delta^2r_1^2r_3^2 - 12r_1^8 + 16r_1^6\right)\left(11r_1^2r_3^{14}\right.\\
&-12r_3^{14} - 45r_1^4r_3^{12} + 24r_1^2r_3^{12} - 48\mu^2r_3^{12} - 192\delta\mu r_3^{12} - 192\delta^2r_3^{12} + 16r_3^{12}\\
&+12r_1^6r_3^{10} + 108r_1^4r_3^{10} - 384\mu^2r_1^2r_3^{10} - 1536\delta\mu r_1^2r_3^{10} - 1536\delta^2r_1^2r_3^{10} - 48r_1^2r_3^{10}\\
&+64\mu^2r_3^{10} + 256\delta\mu r_3^{10} + 256\delta^2r_3^{10} + 90r_1^8r_3^8 - 216r_1^6r_3^8 - 1248\mu^2r_1^4r_3^8\\
&-4992\delta\mu r_1^4r_3^8 - 4992\delta^2r_1^4r_3^8 - 96r_1^4r_3^8 + 640\mu^2r_1^2r_3^8 + 2560\delta\mu r_1^2r_3^8 + 2560\delta^2r_1^2r_3^8\\
&+132r_1^{10}r_3^6 - 288r_1^8r_3^6 - 2304\mu^2r_1^6r_3^6 - 9216\delta\mu r_1^6r_3^6 - 9216\delta^2r_1^6r_3^6 + 384r_1^6r_3^6\\
&+2560\mu^2r_1^4r_3^6 + 10240\delta\mu r_1^4r_3^6 + 10240\delta^2r_1^4r_3^6 - 504r_1^{12}r_3^4 + 576r_1^{10}r_3^4 + \ldots
\end{aligned}$$

$$\begin{aligned}&\ldots - 3072\mu^2 r_1^8 r_3^4 - 12288\delta\mu r_1^8 r_3^4 - 12288\delta^2 r_1^8 r_3^4 + 5120\mu^2 r_1^6 r_3^4 + 20480\delta\mu r_1^6 r_3^4\\&+20480\delta^2 r_1^6 r_3^4 + 304 r_1^{14} r_3^2 + 192 r_1^{12} r_3^2 - 3072\mu^2 r_1^{10} r_3^2 - 12288\delta\mu r_1^{10} r_3^2\\&-12288\delta^2 r_1^{10} r_3^2 - 768 r_1^{10} r_3^2 + 5120\mu^2 r_1^8 r_3^2 + 20480\delta\mu r_1^8 r_3^2 + 20480\delta^2 r_1^8 r_3^2\\&-384 r_1^{14} - 1536\mu^2 r_1^{12} - 6144\delta\mu r_1^{12} - 6144\delta^2 r_1^{12} + 512 r_1^{12} + 2048\mu^2 r_1^{10})\\&+8192\delta\mu r_1^{10} + 8192\delta^2 r_1^{10} = 0 \qquad (3.4)\end{aligned}$$

Next we eliminate the amplitude variables r_1 and r_3 from this equation to give us an equation that depends only on the parameters δ and μ. To accomplish this we need two more independent equations that are satisfied by in-phase slow-flow equilibrium points. The first equation comes from using the trigonometric identity $\cos^2\phi + \sin^2\phi = 1$ on (3.2) and (3.3) to get

$$\frac{r_1^2 r_3^2 (\mu + 2\delta)^2}{\mu^2 \left(r_3^2 - 2r_1^2\right)^2} + \frac{r_1^2 r_3^2 \left(r_3^2 - r_1^2\right)^2}{16\mu^2 \left(r_3^2 + 2r_1^2\right)^2} = 1 \qquad (3.5)$$

The second equation results from multiplying (2.4) by $2r_1$ and adding to it r_3 times (2.5) to get

$$r_3^2 + 2r_1^2 = \frac{1}{4}\left(r_3^4 + 2r_1^4\right) \qquad (3.6)$$

The process of eliminating r_1 and r_3 then proceeds as follows:

1. Simplify all three equations by substituting $r_1 = \sqrt{\rho_1}$ and $r_3 = \sqrt{\rho_3}$.
2. Eliminate ρ_3 from equations (3.4) and (3.6) and then from (3.5) and (3.6).
3. Eliminate ρ_1 from the two resulting equations and factor.

This yields 6 equations that represent possible bifurcation curves in δ-μ parameter space. However, some of these equations will be extraneous solutions created during the elimination of variables, while others will represent bifurcation curves we are not interested in (e.g. they will correspond to situations where there is already an eigenvalue with positive real part and thus do not represent a change in stability). In the end we are interested in only a single curve given by (see Figure 3.1)

$$\begin{aligned}
&11449\mu^{10} + 23968\delta\mu^9 + 43360\delta^2\mu^8 + 2518\mu^8 + 45952\delta^3\mu^7 + 17708\delta\mu^7 \\
&+41920\delta^4\mu^6 + 38572\delta^2\mu^6 - 709\mu^6 + 25600\delta^5\mu^5 + 49920\delta^3\mu^5 + 2428\delta\mu^5 \\
&+13312\delta^6\mu^4 + 46464\delta^4\mu^4 + 8316\delta^2\mu^4 + 76\mu^4 + 4096\delta^7\mu^3 + 28672\delta^5\mu^3 \\
&+13312\delta^3\mu^3 - 560\delta\mu^3 + 1024\delta^8\mu^2 + 14336\delta^6\mu^2 + 10496\delta^4\mu^2 + 16\delta^2\mu^2 \\
&+4096\delta^7\mu + 4608\delta^5\mu + 1152\delta^3\mu + 64\delta\mu + 1024\delta^8 + 1536\delta^6 + 576\delta^4 \\
&+64\delta^2 = 0
\end{aligned} \tag{3.7}$$

Next we investigate whether the equilibrium point can lose its stability via a Hopf bifurcation. Requiring a pair of purely imaginary roots for (3.1) requires its coefficients to satisfy

$$c_1^2c_4^2 + c_0c_3^2c_4 - c_1c_2c_3c_4 - 2c_0c_1c_4 - c_0c_2c_3 + c_1c_2^2 + c_0^2 = 0 \tag{3.8}$$

We follow the same procedure as before to eliminate the amplitudes r_1 and r_3 from (3.8). After substituting $r_1 = \sqrt{\rho_1}$ and $r_3 = \sqrt{\rho_3}$ we eliminate ρ_3 from (3.5) and (3.6). Then eliminating ρ_3 from (3.6) and (3.8) results in an equation with 3 different factors. One of these factors (see (3.18) on page 24 in [19]) we can ignore because it is satisfied by equilibrium points undergoing a Hopf bifurcation *within* the invariant in-phase slow-flow subspace. Finally, eliminating ρ_1 from the final 2 equations results in 3 equations representing possible Hopf bifurcation curves. However, numerical investigation reveals that none of these equations represent bifurcation curves we are interested in. Therefore Figure 3.1 shows the complete

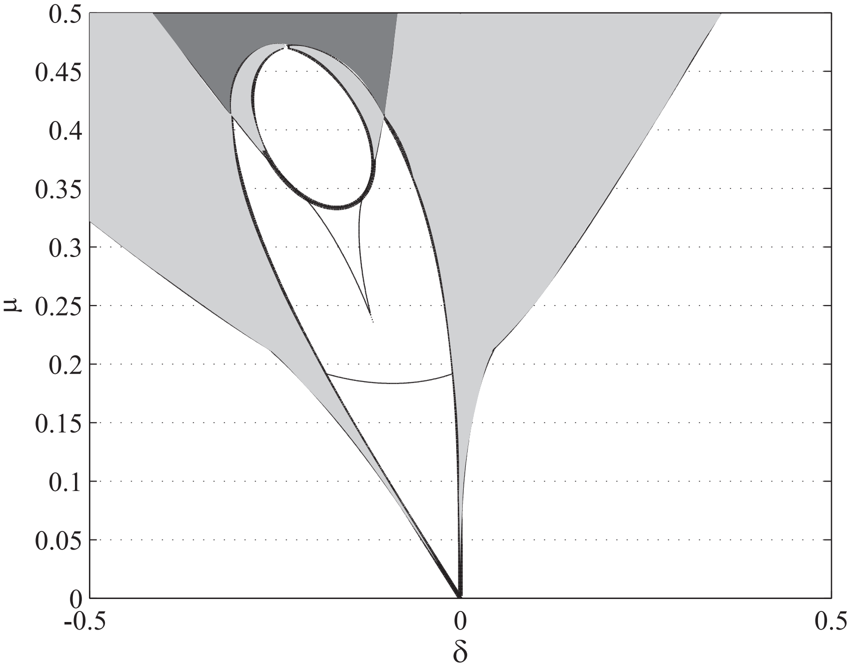

Figure 3.1: New bifurcation curve (3.7) (thick black line) for in-phase slow-flow equilibrium points when considering stability in the full 5-dimensional slow-flow phase space. Number of stable in-phase equilibrium points in each region determined via numerical investigation. light gray = 1 stable in-phase equilibrium point; dark gray = 2 stable in-phase equilibrium points.

stability results for in-phase slow-flow equilibrium points.

The Variational Equations

We now compare our perturbation results to numerical integrations of the original system (2.1). We want to know if within our predicted regions of stability there really do exist stable phase-locked in-phase modes for (2.1).

Let $x(t) = y(t) = f(t)$ and $w(t) = g(t)$ represent a phase-locked in-phase mode for (2.1) with period τ. We now define a small perturbation to this motion as $\alpha(t) = x(t) - f(t)$, $\beta(t) = y(t) - f(t)$ and $\chi(t) = w(t) - g(t)$ and substitute this into the system. Linearizing the resulting flow (since we assume small perturbations) and using the fact that $f(t)$ and $g(t)$ are exact solutions to (2.1), we get the in-phase variational equations

$$\begin{aligned}
\ddot{\alpha} - \epsilon\left(1 - f^2\right)\dot{\alpha} + \left(1 + 2\epsilon f\dot{f}\right)\alpha &= \epsilon\mu\left(\chi - \alpha\right) \\
\ddot{\beta} - \epsilon\left(1 - f^2\right)\dot{\beta} + \left(1 + 2\epsilon f\dot{f}\right)\beta &= \epsilon\mu\left(\chi - \beta\right) \\
\ddot{\chi} - \epsilon\left(1 - g^2\right)\dot{\chi} + \left(p^2 + 2\epsilon g\dot{g}\right)\chi &= \epsilon\mu\left(\alpha + \beta - 2\chi\right)
\end{aligned}$$

where $p = 1 + \epsilon\delta$. We can rewrite this system in matrix-vector form (3.11), or more compactly as

$$\underline{\dot{\mathbf{u}}} = [\mathbf{A}(t)]\underline{\mathbf{u}} \tag{3.9}$$

where $\underline{\mathbf{u}} = \begin{bmatrix} \alpha(t) & \dot{\alpha}(t) & \beta(t) & \dot{\beta}(t) & \chi(t) & \dot{\chi}(t) \end{bmatrix}^T$ and $[A(t)]$ is periodic with period τ. The study of such linear systems with periodic coefficients is known as Floquet Theory (see [17] or [3] for review). We are interested in the boundedness of the trivial solution to (3.9) as this determines the stability of the phase-locked in-phase mode we are perturbing off of.

NUMERICAL FLOQUET THEORY

To motivate our numerical investigation of (3.9) we now briefly review the basics of Floquet Theory. We follow the discussion given in [17].

Let $X(t)$ be a fundamental solution matrix for (3.9) with $X(0) = I$, where I is the 6×6 identity matrix. Due to the periodic nature of the matrix $A(t)$, substituting $t = t + \tau$ into $X(t)$ produces a new fundamental solution matrix $X(t + \tau)$. These two fundamental solution matrices can be related via an invertible matrix C such that

$$X(t + \tau) = X(t)C \tag{3.10}$$

Substituting $t = 0$ into (3.10) yields the monodromy matrix $C = X(\tau)$, i.e. the invertible matrix C can be found column-by-column via numerical integration of

$$\frac{d}{dt}\begin{bmatrix}\alpha\\ \dot{\alpha}\\ \beta\\ \dot{\beta}\\ \chi\\ \dot{\chi}\end{bmatrix}=\begin{bmatrix}0 & 1 & 0 & 0 & 0 & 0\\ -\epsilon\mu-(1+2\epsilon f\dot{f}) & \epsilon(1-f^2) & 0 & 0 & \epsilon\mu & 0\\ 0 & 0 & 0 & 1 & 0 & 0\\ 0 & 0 & -\epsilon\mu-(1+2\epsilon f\dot{f}) & \epsilon(1-f^2) & \epsilon\mu & 0\\ 0 & 0 & 0 & 0 & 0 & 1\\ \epsilon\mu & 0 & \epsilon\mu & 0 & -2\epsilon\mu-(p^2+2\epsilon g\dot{g}) & \epsilon(1-g^2)\end{bmatrix}\begin{bmatrix}\alpha\\ \dot{\alpha}\\ \beta\\ \dot{\beta}\\ \chi\\ \dot{\chi}\end{bmatrix} \tag{3.11}$$

the system on the interval $[0, \tau]$ for the six linearly independent initial conditions given by the columns of the identity matrix. Substituting $t = \tau$ into (3.10) yields $X(2\tau) = C^2$. If we continue this for n-periods we find that $X(n\tau) = C^n$. Therefore the long-term behavior of solutions to the system is intimately connected with the matrix C.

We now assume that the matrix C has 6 linearly independent eigenvectors. Let $Y(t)$ be yet another fundamental solution matrix such that $Y(t) = X(t)R$, where the columns of R are the 6 linearly independent eigenvectors of the matrix C. Rewriting (3.10) in terms of $Y(t)$ yields

$$Y(t+\tau) = Y(t)R^{-1}CR = Y(t)\Lambda \tag{3.12}$$

where Λ is a diagonal matrix with the eigenvalues of C on its diagonal. Thus the i^{th} column of (3.12) can be written as

$$Y_i(t+\tau) = \lambda_i Y_i(t) \tag{3.13}$$

We now look for a solution to (3.13) of the form $Y_i(t) = \lambda_i^{kt} p_i(t)$ where k is an unknown constant and p_i is an unknown function. Substituting this into (3.13) yields

$$\lambda_i^{k(t+\tau)} p_i(t+\tau) = \lambda_i \left(\lambda_i^{kt} p_i(t)\right)$$

This is satisfied when $k = \frac{1}{\tau}$ and $p_i(t)$ is some periodic function with period τ. Thus our solution becomes $Y_i(t) = \lambda_i^{\frac{t}{\tau}} p_i(t)$ where $p_i(t+\tau) = p_i(t)$.

Recall that (3.9) governs the behavior of perturbations to a phase-locked in-phase mode for (2.1). For this mode to be considered stable the perturbations must remain bounded as $t \to \infty$. From the discussion above we see that the boundedness of the perturbations will be determined by the eigenvalues λ_i of the matrix C. If $|\lambda_i| < 1$ then $Y_i(t) \to 0$ as $t \to \infty$. Likewise, if $|\lambda_i| > 1$ then $Y_i(t) \to \infty$ as $t \to \infty$. Therefore we require every eigenvalue of the matrix C to have norm less than or equal to unity in order for the phase-locked in-phase mode to be stable.

To numerically determine the stability of a phase-locked in-phase mode we follow the procedure set forth in [17]. We use MATLAB® to perform our numerical integrations. For each point in δ-μ parameter space we must perform the following tasks:

1. Numerically calculate the phase-locked in-phase mode.
2. Calculate the period of this motion and store the data.
3. Compute the monodromy matrix.
4. Check the norm of the eigenvalues of the monodromy matrix.

We now briefly describe the code used to perform each of these steps. See Appendix B for our complete MATLAB code.

Step 1: Numerically calculate the phase-locked in-phase mode.

We begin by numerically integrating the in-phase subspace equations (2.2) using MATLAB's `ode45` numerical integrator, with decreased tolerances and event location (see Figure 3.2).

```
options = odeset('Events',@EVENTS,'AbsTol',1e-7,'RelTol',1e-4);
sol = ode45(@inphase,[0 1250],[0;2;-2;-.1],options,parameters);
```

Figure 3.2: MATLAB code for numerically calculating the phase-locked in-phase mode.

```
function [value, isterminal, direction] = EVENTS(t,y,p)

value = y(1);
isterminal = 0;
direction = +1;
```

Figure 3.3: MATLAB code for the `EVENT` function.

The `EVENT` function (see Figure 3.3) is defined to detect every time the x-oscillator equals zero. The recorded events will be used to determine when the integrator has reached a steady-state solution. The function returns three values – `value = y(1)` signifies that we are interested in when the first state variable, i.e. $x(t)$, crosses zero, `isterminal = 0` tells the integrator not to stop when the event is encountered, and `direction = +1` tells the integrator only to record instances where the event occurs with a positive slope.

The subfunction `inphase` defines the differential equations (2.2). The timespan for integration and initial conditions were chosen because they start the integration close to the in-phase mode for a wide range of parameter values and allow enough time for steady-state motion to be reached. The numerically computed solution is then stored in the structure `sol`.

Step 2. Calculate the period of this motion and store the data.

The second step is to calculate the period of the in-phase mode using the `calculate_period` function (see Figure 3.4). The function takes as input the output of a Matlab numerical integrator in structure format. We place as much of our code as possible into separate subfunctions, as opposed to creating a script file with one large `for` loop, for purposes of efficiency [11]. This is particularly important since we will be calling many of our subfunctions multiple times.

```
function [period,begin_time] = calculate_period(sol)

intervals = abs(diff(sol.ye,1,2));
indices = find(vnorm(intervals,1) < 1e-3);

if ~isempty(indices)
    period = sol.xe(indices(end)) - sol.xe(indices(end)-1);
    begin_time = sol.xe(indices(end)-1);
else
    period = 0;
    begin_time = 0;
end
```

Figure 3.4: MATLAB code for the `calculate_period` function.

The solution structure `sol` contains two important fields - `sol.ye` is a `4 x n` vector where each column represents the state of the system when an event was encountered and `sol.xe` is a `1 x n` vector containing the times at which the events occured. Here `n` represents the number of times the specified event occurred during the numerical integration performed in the first step.

First we calculate the absolute values of the differences between state variables at successive event occurrences and store the result in `intervals`. In theory the first row of `intervals` should be all zeros since an event occurrence is defined by the first state variable vanishing. Next we find the indices of `intervals` where the norm of the state variable differences is less than `1e-3`. This is our criteria for when a steady-state periodic motion has been reached and was chosen via trial-and-error to balance computational time and numerical accuracy. The function `vnorm` allows for easy computation of vector norms column-by-column [21].

Assuming the numerical integration reached a steady-state periodic motion we calculate the period of the motion and the time at which the motion begins. The `begin_time` variable will be used in the next step. If no steady-state is found we return a period and beginning time equal to 0 and then skip to the next parameter pair.

Step 3. Compute the monodromy matrix.

Before computing the monodromy matrix we first compute a numerical representation of the phase-locked in-phase mode (see Figure 3.5).

```
interval = [begin_time-.01:.01:begin_time+period+.01];
inphase_mode = [interval' deval(sol,interval)'];
```

Figure 3.5: MATLAB code for computing a numerical representation of the phase-locked in-phase mode.

The variable `interval` contains a vector of times for one period of the periodic motion. We input this vector along with the solution structure `sol` into the built-in MATLAB function `deval`. `deval` will evaluate the in-phase mode at .01 time intervals using the solution structure. We save the result in `inphase_mode`.

Now we can compute the monodromy matrix using the `monodromy_matrix` function (see Figure 3.6). This function takes as input the computed in-phase mode and its computed period, the time at which the motion begins, and the system parameters required for numerically integrating the variational equations (3.11) (i.e. ϵ, δ, and μ).

```
function C = monodromy_matrix(period, begin_time, ...
    inphase_mode, parameters)

C = zeros(6,6);
I = eye(6);
options = odeset('AbsTol',1e-7,'RelTol',1e-4);

for i = 1:6
    [T,Y] = ode45(@inphase_variational,[0 period],I(:,i),...
        options, begin_time, inphase_mode, parameters);
    C(:,i) = Y(end,:)';
end
```

Figure 3.6: MATLAB code for the `monodromy_matrix` function.

For the numerical integration of the linearized variational equations we use the same tolerances as before. From Floquet theory we know that the i^{th} column of the monodromy matrix can be found by integrating the variational equations for one period with an initial condition equal to the i^{th} column of the identity matrix.

We pass the numerically computed in-phase mode to the function `inphase_variational` since the coefficients in (3.11) involve the steady-state solution. Inside this function we need to linearly interpolate points within the steady-state solution at each step of the integration (see Figure 3.7).

```
temp = interp1q(inphase_mode(:,1),inphase_mode(:,2:5),...
    begin_time+t);
```

Figure 3.7: MATLAB code for linearly interpolating points within the steady-state solution.

An alternative approach would be to pass the solution structure `sol` to the function and use `deval`. While this would be a more precise method of interpolation, it is much more computationally expensive. Therefore we instead use the built-in function `interp1q`, which is a fast version of linear interpolation.

Step 4. Check the norm of the eigenvalues of the monodromy matrix. Finally we check the eigenvalues of the monodromy matrix to determine boundedness (see Figure 3.8). Our criteria for boundedness is that the largest eigenvalue must have modulus less than `1e-3` greater than unity.

```
eigenvalues = sort(eig(C));

if((abs(eigenvalues(end))-1) > 1e-3)
    results(counter,:) = [delta mu 1 period...
    abs(eigenvalues(end))];
    counter = counter + 1;
else
    results(counter,:) = [delta mu 2 period...
    abs(eigenvalues(end))];
    counter = counter + 1;
end
```

Figure 3.8: MATLAB code for computing the eigenvalues of the monodromy matrix C and checking the norm of the largest eigenvalue.

No matter if our criteria for stability is met or not we record the parameter pair, the stability result, the period of the computed in-phase mode, and the absolute value of largest eigenvalue before moving on to the next parameter pair.

Discussion

The initial results from our numerical Floquet analysis are shown in Figure 3.9. Recall from Table 2.1 that Regions V and VI contain two stable equilibrium points and therefore are expected to contain two distinct phase-locked in-phase modes. Unfortunately our MATLAB code was written to test only the stability of a single phase-locked in-phase mode for each pair of parameters. Therefore we modify our code slightly so that it tests for two distinct modes in these regions (see Figure 3.10).

There is excellent agreement between our numerical and perturbation results for $\delta < 0$. Comparing Figures 3.1 and 3.9 shows that the perturbation results accurately predict the transition between stable drift motion and stable phase-locked in-phase motion (e.g. the transition from Region II to Region IV, see Figure 2.1). Furthermore, (3.7) appears to correctly predicts the loss of stability for the in-phase mode. For $\delta > 0$ our results start to differ as μ increases. Specifically, it appears that the Hopf bifurcation curve (A.6) does not predict the transition from stable drift to stable phase-locking accurately for $\mu > 0.2$. However, this discrepancy might also be explained by the initial integration interval used in our MATLAB code to calculate the phase-locked in-phase mode being too small for these parameter values.

Another discrepancy between our numerical and analytical results can be seen in Figure 3.10. While our analytic results predict a transition from 0 to 2 stable in-phase modes in Regions V and VI, the computed bifurcation curve does not accurately separate the various transition regions. Furthermore we did not predict such a transition between Regions IV and VI while the numerical results indicate such a transition exits.

Our numerical Floquet results support the conclusions of our perturbation analysis. From Figure 3.1 we see that the regions of parameter space where phase-locked in-phase modes exist for (2.1) is reduced from that shown in Figure 2.3. This is expected since our results from Chapter 2 only considered stability within the in-phase subspace (2.2). We can now conclude that the weakly coupled VDP system (2.1) does exhibit behavior similar to that seen in the experiments. Furthermore there are parameter regions where (2.1) exhibits two different stable phase-locked in-phase modes and these regions appear to exist exclusively for $\delta < 0$.

Existence and Stability of the Out-of-Phase Mode

We now turn our attention to the existence and stability of the out-of-phase mode

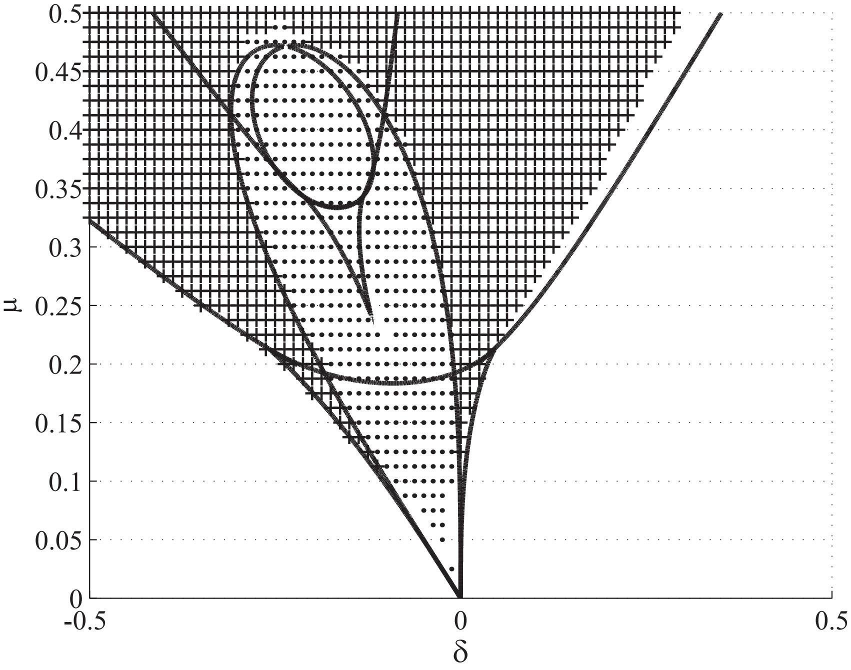

Figure 3.9: Initial results from numerical Floquet analysis. Black curves represent saddle-node (or infinite-period) and Hopf bifurcation curves for the in-phase slow-flow (2.4). stable in-phase mode = plus sign; unstable in-phase mode = dot; no in-phase mode exists = blank.

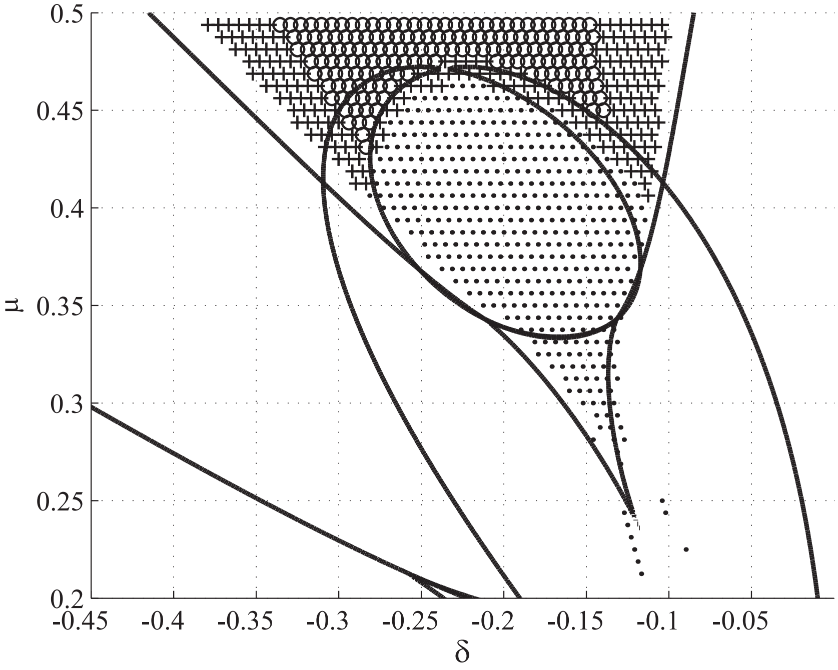

Figure 3.10: Results from second numerical Floquet analysis concentrating on regions where two stable phase-locked in-phase modes are predicted to exist. 2 stable in-phase modes = circle; 1 stable in-phase mode = plus sign; 0 stable in-phase modes = dot; 1 or fewer in-phase modes exist = blank.

for (2.1). The out-of-phase subspace is defined by setting $x\left(t\right) = -y\left(t\right)$ in (2.1). However, for (2.1) to remain consistent we must also require $w(t) = 0$ for all time t. Therefore the dynamics of the out-of-phase subspace are governed by the reduced 2-dimensional flow

$$\ddot{x} - \epsilon\left(1 - x^2\right)\dot{x} + \left(1 + \epsilon\mu\right)x = 0 \tag{3.14}$$

The out-of-phase mode will be an exact periodic solution for (3.14). Since (3.14) is the equation of motion for an uncoupled VDP oscillator with frequency $\sqrt{1+\epsilon\mu}$, the out-of-phase mode exists for all $\epsilon > 0$ [25]. Here we assume that the frequency remains positive. It is interesting to note that if we relax this assumption the existence of the out-of-phase mode depends on an inversely-proportional relationship between the parameters ϵ and μ that must be satisfied.

With existence proven, we now investigate the stability of the out-of-phase mode. Unfortunately we cannot use the 5-dimensional slow-flow (2.3) since it is not properly defined when $w(t) = 0$. Therefore we only undertake a numerical stability analysis via Floquet theory (following the same procedure and using essentially the same MATLAB code as previously described).

Let $x(t) = f(t)$, $y(t) = -f(t)$ and $w(t) = 0$ be an out-of-phase mode for (2.1) with period τ. We now define a small perturbation to this motion as $\alpha(t) = x(t) - f(t)$, $\beta(t) = y(t) + f(t)$ and $\chi(t) = w(t) - 0$ and substitute this into the system. Linearizing the resulting flow (once again assuming small perturbations) and using the fact that the out-of-phase mode is an exact solution for (2.1) we get

$$\frac{d}{dt}\begin{bmatrix}\alpha\\ \dot{\alpha}\\ \beta\\ \dot{\beta}\\ \chi\\ \dot{\chi}\end{bmatrix}=\begin{bmatrix}0 & 1 & 0 & 0 & 0 & 0\\ -\epsilon\mu-(1+2\epsilon f\dot{f}) & \epsilon(1-f^2) & 0 & 0 & \epsilon\mu & 0\\ 0 & 0 & 0 & 1 & 0 & 0\\ 0 & 0 & -\epsilon\mu-(1+2\epsilon f\dot{f}) & \epsilon(1-f^2) & \epsilon\mu & 0\\ 0 & 0 & 0 & 0 & 0 & 1\\ \epsilon\mu & 0 & \epsilon\mu & 0 & -2\epsilon\mu-p^2 & \epsilon\end{bmatrix}\begin{bmatrix}\alpha\\ \dot{\alpha}\\ \beta\\ \dot{\beta}\\ \chi\\ \dot{\chi}\end{bmatrix} \qquad (3.15)$$

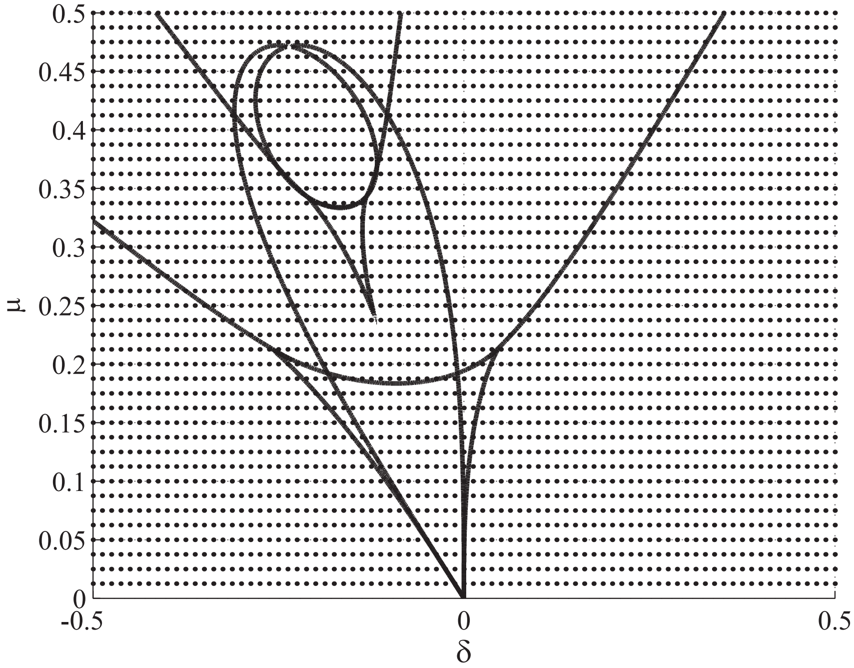

Figure 3.11: Stability results for the out-of-phase mode via numerical Floquet theory for $\epsilon = 0.1$. The out-of-phase mode exists and is unstable for all tested parameter values. unstable = dot.

the out-of-phase variational equations

$$\begin{aligned}\ddot{\alpha} - \epsilon\left(1 - f^2\right)\dot{\alpha} + \left(1 + 2\epsilon f\dot{f}\right)\alpha &= \epsilon\mu\left(\chi - \alpha\right)\\ \ddot{\beta} - \epsilon\left(1 - f^2\right)\dot{\beta} + \left(1 + 2\epsilon f\dot{f}\right)\beta &= \epsilon\mu\left(\chi - \beta\right)\\ \ddot{\chi} - \epsilon\dot{\chi} + p^2\chi &= \epsilon\mu\left(\alpha + \beta - 2\chi\right)\end{aligned}$$

where $p = 1 + \epsilon\delta$. We rewrite the system in vector form (3.15) or more compactly as

$$\underline{\dot{\mathbf{u}}} = [\mathbf{A}(t)]\underline{\mathbf{u}} \tag{3.16}$$

where $\underline{\mathbf{u}} = \begin{bmatrix}\alpha(t) & \dot{\alpha}(t) & \beta(t) & \dot{\beta}(t) & \chi(t) & \dot{\chi}(t)\end{bmatrix}^T$ and $[A(t)]$ is periodic with period τ. After modifying our MATLAB code to work with the out-of-phase variational equations we perform numerical Floquet analyses for $\epsilon = 0.1$ and $\epsilon = 0.7$. Our first analysis shows that for all tested parameter values in δ-μ parameter space the out-of-phase mode exists and is unstable (see Figure 3.11). Furthermore, increasing the nonlinearity parameter ϵ to $\epsilon = 0.7$ does not alter this conclusion.

CHAPTER 4
THREE COUPLED PHASE OSCILLATORS

In CHAPTERS 2 and 3 VDP oscillators were used to model the avian circadian system mainly because of their ubiquitous use in biological modeling. Also, it has been shown [1] that with a few simple assumptions the biochemical basis of a circadian rhythm in free-running conditions can be reduced to such an oscillator with constant forcing. However, we have no other biological basis for assuming such an oscillator is the best model for the endogenous melatonin rhythms found in the eyes of Japanese quail or for the neuroendocrine loop [2], consisting of the pineal and SCN, considered here to be a single extra-ocular oscillator.

In this chapter we focus on two simpler, lower dimensional models for the avian circadian system where each melatonin rhythm is mathematically modeled as a phase oscillator, i.e. a one degree-of-freedom oscillator whose current state is determined by its phase relative to some origin and whose amplitude is eliminated from consideration.

Considering simpler, lower dimensional models allows us to investigate the dynamics of the system more completely and accurately. That is, we will not be limited to the study of in-phase modes alone, but all solutions, including those not within the in-phase subspace. This will provide us with more information for determining if these models exhibit behavior like that found in the experiments.

FIRST COUPLED PHASE OSCILLATOR MODEL

For our first coupled phase oscillator model we return to the 5-dimensional slow-flow (2.3) derived from the weakly coupled VDP system (2.1) and drop the slow-flow amplitude equations from consideration and focus only on the slow-flow phase equations

$$
\begin{aligned}
\dot{\phi}_1 &= \frac{\mu}{2}\left[\frac{R_2}{R_3}\cos\phi_2 + \left(\frac{R_1}{R_3} - \frac{R_3}{R_1}\right)\cos\phi_1 - 1\right] - \delta \\
\dot{\phi}_2 &= \frac{\mu}{2}\left[\frac{R_1}{R_3}\cos\phi_1 + \left(\frac{R_2}{R_3} - \frac{R_3}{R_2}\right)\cos\phi_2 - 1\right] - \delta
\end{aligned}
\tag{4.1}
$$

where $\phi_1 = \theta_3 - \theta_1$ and $\phi_2 = \theta_3 - \theta_2$ are the phase-differences between the w- and x- and w- and y-oscillators respectively. We now consider the phase-differences to evolve on the normal time-scale (as opposed to slow-time) and thus a "dot" denotes differentiation with respect to time t. We simplify (4.1) by assuming the "amplitudes" are equal to a VDP oscillator's uncoupled amplitude, i.e. $R_1 = R_2 = R_3 = 2$, giving us the reduced 2-dimensional coupled phase oscillator system

$$
\begin{aligned}
\dot{\phi}_1 &= \frac{\mu}{2}\left[\cos\phi_2 - 1\right] - \delta \\
\dot{\phi}_2 &= \frac{\mu}{2}\left[\cos\phi_1 - 1\right] - \delta
\end{aligned}
\tag{4.2}
$$

Note that this system is suggested by but not derivable from the weakly coupled VDP system (2.1) (i.e. $R_1 = R_2 = R_3 = 2$ is not in general a solution to (2.3)).

An exact solution to (4.2) evolves on a torus since both ϕ_1 and ϕ_2 are cyclic with period 2π. An equilibrium point $(\phi_1, \phi_2) = (\phi_1^*, \phi_2^*)$ for (4.2) represents a phase-locked motion. An in-phase mode for (4.2) will be an exact solution with $\phi_1(t) = \phi_2(t) = \phi(t)$. Therefore a phase-locked in-phase mode for (4.2) will be represented by an equilibrium point with $\phi_1^* = \phi_2^* = \phi^*$.

We begin by investigating under what conditions do there exist equilibrium points for (4.2). Setting the right-hand side of (4.2) equal to zero, we solve for $\cos\phi_i^*$ (for $i = 1, 2$) to get

$$\cos\phi_i^* = 1 + \frac{2\delta}{\mu}$$

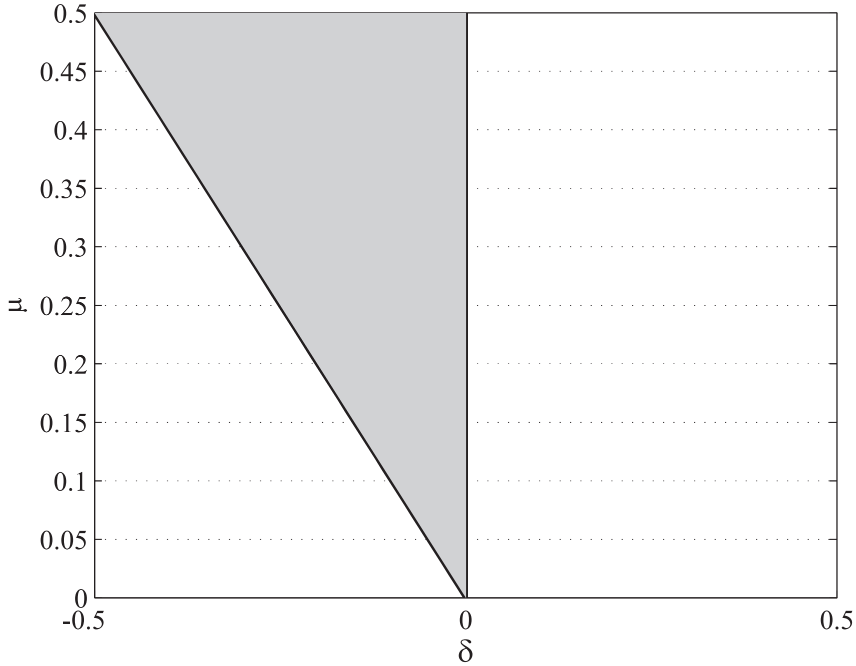

Figure 4.1: Region of δ-μ parameter space defined by (4.4) where phase-locked motions for (4.2) exist. Outside this region there exist only drift motions. phase-locking region = gray.

This equation results in a pair of values for ϕ_i^* if and only if

$$\left|1 + \frac{2\delta}{\mu}\right| < 1 \tag{4.3}$$

By rewriting this as the interval

$$-\mu < \delta < 0 \tag{4.4}$$

we see that (4.3) defines a region of δ-μ parameter space within which equilibrium points for (4.2) exist. That is, it defines the phase-locking region (i.e. the region where phase-locked motions for (4.2) exist) of δ-μ parameter space (see Figure 4.1). Outside this region there are no equilibrium points for (4.2) and there exist only drift motions.

We now solve for the equilibrium points of (4.2) in closed-form (see Table 4.1). Note that $\phi_1^* = \phi_2^* = \phi^*$ for EQPT1 and EQPT2 and therefore these two equilibrium points represent distinct phase-locked in-phase modes for (4.2), while EQPT3 and EQPT4 represent non-in-phase solutions.

To determine the stability of an equilibrium point (ϕ_1^*, ϕ_2^*) we linearize the flow (4.2) about the equilibrium point. This linearized flow is given by the Jacobian matrix evaluated at the equilibrium point.

$$\begin{bmatrix} 0 & -\frac{\mu}{2}\sin\phi_2^* \\ -\frac{\mu}{2}\sin\phi_1^* & 0 \end{bmatrix} \tag{4.5}$$

The stability of the equilibrium point is determined by the eigenvalues of (4.5) which are given in Table 4.2.

From Table 4.2 we see that $\lambda_1 = -\lambda_2$ for all 4 equilibrium points. Furthermore, since the existence of equilibrium points implies (4.3), we conclude that EQPT1 and EQPT2 have two real eigenvalues of opposite sign and therefore are saddles while EQPT3 and EQPT4 have purely imaginary eigenvalues and thus are nonlinear centers (see Figure 4.2). Numerical integration of (4.2) for parameters within the phase-locking region defined by (4.4) reveals that all solution trajectories exhibit either drift motion or a weakly phase-locked motion (see Figure 4.3).

From our analysis we must conclude that (4.2) is an inappropriate model for the experiments. We have shown that within the phase-locking region of parameter space defined by (4.4) all phase-locked in-phase modes are unstable. There exist stable non-in-phase motions as well. Therefore the model does not meet the necessary criteria for it to exhibit behavior like that in the experiments.

Table 4.1: The 4 equilibrium points of the system (4.2).

EQPT	(ϕ_1^*,ϕ_2^*)
1	$\left(\cos^{-1}\left(1+\frac{2\delta}{\mu}\right), \cos^{-1}\left(1+\frac{2\delta}{\mu}\right)\right)$
2	$\left(2\pi-\cos^{-1}\left(1+\frac{2\delta}{\mu}\right), 2\pi-\cos^{-1}\left(1+\frac{2\delta}{\mu}\right)\right)$
3	$\left(2\pi-\cos^{-1}\left(1+\frac{2\delta}{\mu}\right), \cos^{-1}\left(1+\frac{2\delta}{\mu}\right)\right)$
4	$\left(\cos^{-1}\left(1+\frac{2\delta}{\mu}\right), 2\pi-\cos^{-1}\left(1+\frac{2\delta}{\mu}\right)\right)$

Table 4.2: The eigenvalues of the 4 equilibrium points of the system (4.2).

EQPT	λ_1	λ_2
1,2	$-\frac{\mu}{2}\sqrt{1-\left(\frac{2\delta}{\mu}+1\right)^2}$	$\frac{\mu}{2}\sqrt{1-\left(\frac{2\delta}{\mu}+1\right)^2}$
3,4	$-\frac{\mu}{2}\sqrt{\left(\frac{2\delta}{\mu}+1\right)^2-1}$	$\frac{\mu}{2}\sqrt{\left(\frac{2\delta}{\mu}+1\right)^2-1}$

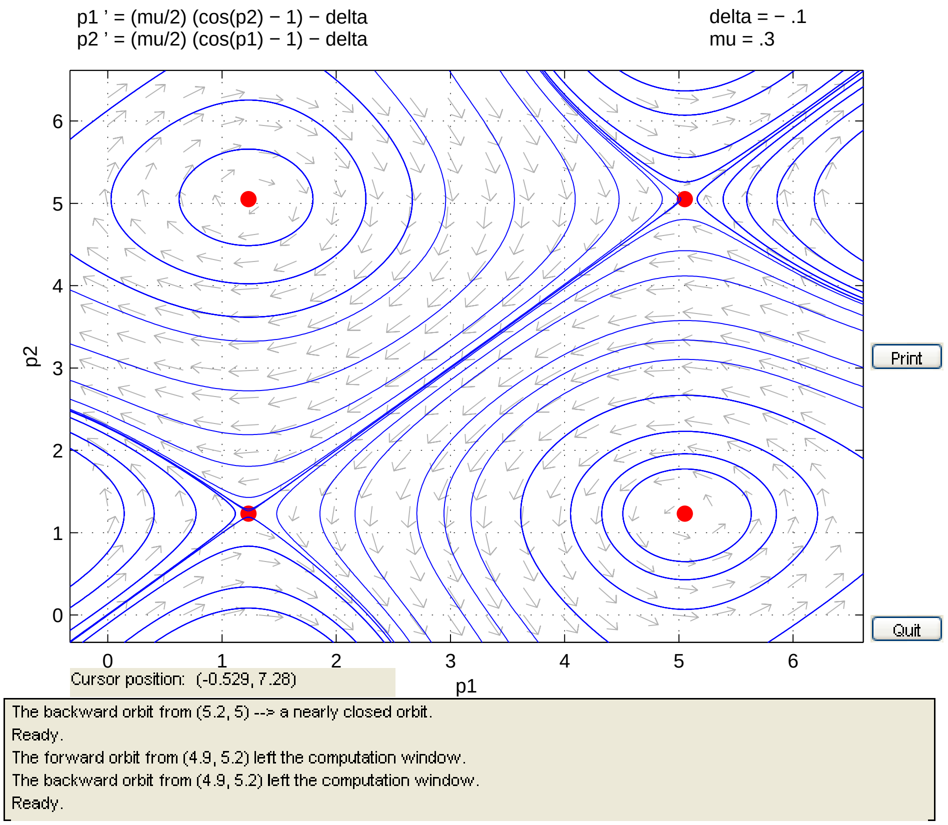

p1 ' = (mu/2) (cos(p2) − 1) − delta
p2 ' = (mu/2) (cos(p1) − 1) − delta

delta = − .1
mu = .3

Cursor position: (-0.529, 7.28)

```
The backward orbit from (5.2, 5) --> a nearly closed orbit.
Ready.
The forward orbit from (4.9, 5.2) left the computation window.
The backward orbit from (4.9, 5.2) left the computation window.
Ready.
```

Figure 4.2: Phase diagram [15] for (4.2) with parameter values $\delta = -0.1$, $\mu = 0.3$. There exist 4 equilibrium points – 2 in-phase saddles (EQPT1 and EQPT2) and 2 non-in-phase nonlinear centers (EQPT3 and EQPT4).

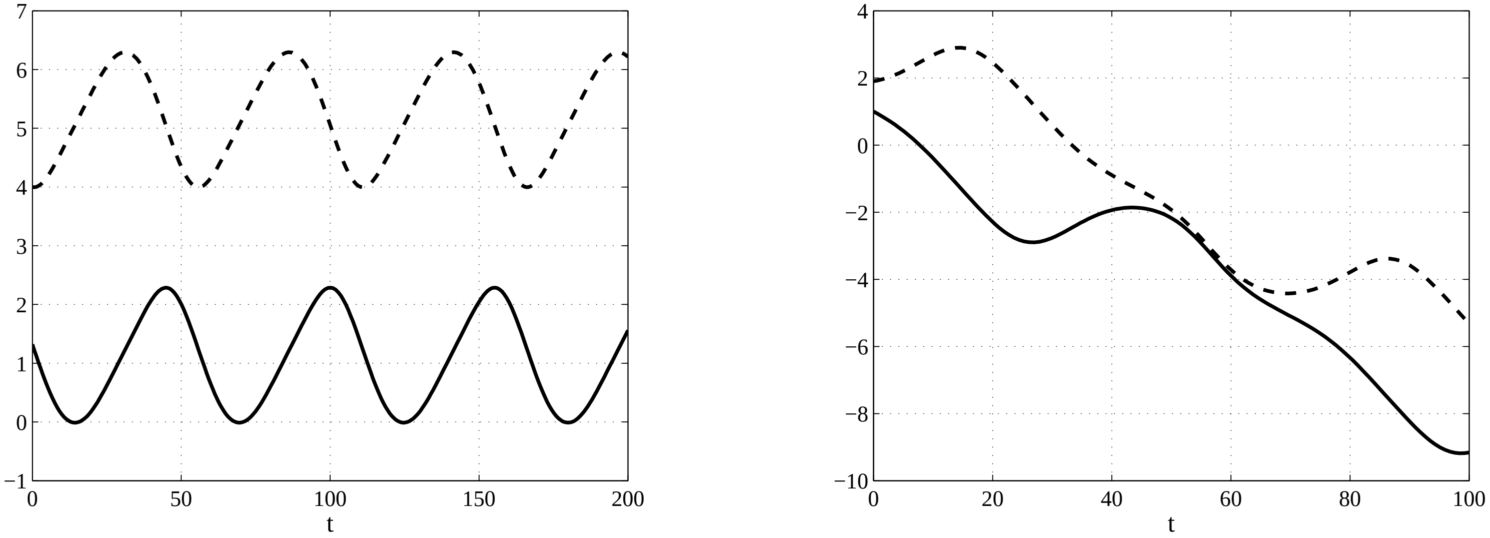

Figure 4.3: Numerical integrations for the system (4.2) with parameter values $\delta = -0.1$, $\mu = 0.3$. This parameter pair lies inside the phase-locking region defined by (4.4) and the plots represent stable weakly phase-locked and drift motion respectively. $\phi_1(t)$ = solid line; $\phi_2(t)$ = dashed line.

Second Phase Oscillator Model

We now investigate a second coupled phase oscillator model based off the slow-flow phase equations (4.1). We modify our approach from the first coupled phase oscillator model (4.2) by no longer assuming $R_1 = R_2 = R_3 = 2$ since we have shown this leads to an inappropriate model for the experiments. Instead, we introduce two new parameters, A and B, defined as the ratios of the "amplitudes" in (4.1), i.e.

$$\begin{aligned} A &= \frac{R_3}{R_1} \\ B &= \frac{R_3}{R_2} \end{aligned}$$

The resulting 2-dimensional coupled phase oscillator system is given by

$$\begin{aligned} \dot{\phi}_1 &= \frac{\mu}{2}\left[\frac{1}{B}\cos\phi_2 + (\frac{1}{A} - A)\cos\phi_1 - 1\right] - \delta \\ \dot{\phi}_2 &= \frac{\mu}{2}\left[\frac{1}{A}\cos\phi_1 + (\frac{1}{B} - B)\cos\phi_2 - 1\right] - \delta \end{aligned} \qquad (4.6)$$

where $\phi_1 = \theta_3 - \theta_1$ and $\phi_2 = \theta_3 - \theta_2$ are the phase-differences between the w- and x- and w- and y-oscillators respectively and a "dot" denotes differentiation with respect to time t. For our modeling purposes we require the existence of an in-phase mode for (4.6). Substituting $\phi_1(t) = \phi_2(t) = \phi(t)$ into (4.6) we find that $B = A$. Thus our final 2-dimensional coupled phase oscillator system is given by

$$\begin{aligned} \dot{\phi}_1 &= \frac{\mu}{2}\left[\frac{1}{A}\cos\phi_2 + (\frac{1}{A} - A)\cos\phi_1 - 1\right] - \delta \\ \dot{\phi}_2 &= \frac{\mu}{2}\left[\frac{1}{A}\cos\phi_1 + (\frac{1}{A} - A)\cos\phi_2 - 1\right] - \delta \end{aligned} \qquad (4.7)$$

and depends on the three parameters A, δ, and μ. We restrict our analysis to $\mu > 0$

and $A > 0$. An exact solution to (4.7) evolves on a torus since both ϕ_1 and ϕ_2 are cyclic with period 2π. An equilibrium point $(\phi_1, \phi_2) = (\phi_1^*, \phi_2^*)$ for (4.7) represents a phase-locked motion. An in-phase mode for (4.7) will be an exact solution with $\phi_1(t) = \phi_2(t) = \phi(t)$. Therefore a phase-locked in-phase mode will be represented by an equilibrium point with $\phi_1^* = \phi_2^* = \phi^*$.

The following analysis closely follows that for the first coupled phase oscillator model. Once again we begin by investigating under what conditions do there exist equilibrium points for (4.7). Setting the right-hand side of (4.7) equal to zero, we solve for $\cos\phi_i^*$ (for $i = 1, 2$) to get

$$\cos\phi_i^* = -\frac{A(\mu + 2\delta)}{(A^2 - 2)\mu}$$

This equation results in a pair of values for ϕ_i^* if and only if

$$\left| -\frac{A(\mu + 2\delta)}{(A^2 - 2)\mu} \right| < 1 \tag{4.8}$$

By rewriting this as the intervals

$$f_2(A)\mu < \delta < f_1(A)\mu \tag{4.9}$$

for $A < \sqrt{2}$, and

$$f_1(A)\mu < \delta < f_2(A)\mu \tag{4.10}$$

for $A > \sqrt{2}$, where

$$\begin{aligned} f_1(A) &= -\frac{(A-1)(A+2)}{2A} \\ f_2(A) &= \frac{(A-2)(A+1)}{2A} \end{aligned}$$

we see that (4.8) defines a region of δ-μ parameter space within which equilibrium points for (4.7) exist. That is, given the parameter A, (4.10) or (4.9) (depending on the value of A) defines the phase-locking region of δ-μ parameter space (see Figure 4.4). Outside this region there are no equilibrium points for (4.7) and there exist only drift motions. Note that substituting $A = 1$ into (4.9) defines a phase-locking region equal to (4.4). That is, the first coupled phase oscillator model (4.2) is a special case for (4.7) when $A = 1$.

We now solve for the equilibrium points of (4.7) in closed-form (see Table 4.3). Note that $\phi_1^* = \phi_2^* = \phi^*$ for EQPT1 and EQPT2 and therefore these two equilibrium points represent distinct phase-locked in-phase modes for (4.7), while EQPT3 and EQPT4 represent non-in-phase solutions.

To determine the stability of an equilibrium point (ϕ_1^*, ϕ_2^*) we linearize the flow (4.7) about the equilibrium point. This linearized flow is given by the Jacobian matrix evaluated at the equilibrium point.

$$\begin{bmatrix} \frac{A^2-1}{2A}\mu \sin\phi_1^* & -\frac{\mu}{2A}\sin\phi_2^* \\ -\frac{\mu}{2A}\sin\phi_1^* & \frac{A^2-1}{2A}\mu\sin\phi_2^* \end{bmatrix} \tag{4.11}$$

The stability of the equilibrium point is determined by the eigenvalues of (4.11). Since we are most interested in the stability of phase-locked in-phase modes we investigate the stabilities of EQPT1 and EQPT2 first. Substituting $\phi_1^* = \phi_2^* = \phi^*$ in (4.11) its eigenvalues are

$$\begin{aligned} \lambda_1 &= \frac{A^2-2}{2A}\mu\sin\phi^* \\ \lambda_2 &= \frac{A}{2}\mu\sin\phi^* \end{aligned}$$

Recall that we have restricted our analysis to $\mu > 0$ and $A > 0$. Also notice that both eigenvalues have the common factor $\mu \sin \phi^*$. There are two cases to consider - $A < \sqrt{2}$ and $A > \sqrt{2}$. For the former case the coefficients of $\mu \sin \phi_1^*$ have opposite signs and therefore both equilibrium points will be saddles. In the latter case the coefficients will both be positive and stability will be determined via the sign of $\sin \phi^*$. From Table 4.3 we see that for EQPT1 $\phi^* < \pi$ (since the range of the arccosine function is $[0, \pi]$) and so both its eigenvalues will be positive while for EQPT2 $\phi^* > \pi$ and therefore both its eigenvalues will be negative. We conclude that there exists a stable in-phase mode (EQPT2) for (4.7) when $A > \sqrt{2}$ and δ and μ lie within the phase-locking region defined by (4.10) (see Figure 4.5). It is also worth noting that the region defined by (4.10) where stable phase-locked in-phase modes are found exists exclusively for $\delta < 0$ when $\sqrt{2} < A < 2$.

Next we investigate the stability of the non-in-phase equilibrium points EQPT3 and EQPT4. The eigenvalues of (4.11) are

$$\begin{aligned}
\lambda_1 &= -\frac{\mu}{4\sqrt{2}A}\Big[\big((2A^4 - 4A^2 - 2)\cos(\phi_2^* + \phi_1^*) + (-2A^4 + 4A^2 + 2)\cos(\phi_2^* - \phi_1^*) \\
&\quad +(-A^4 + 2A^2 - 1)\cos(2\phi_2^*) + (-A^4 + 2A^2 - 1)\cos(2\phi_1^*) + 2A^4 - 4A^2 \\
&\quad +2\big)^{\frac{1}{2}} - \sqrt{2}A^2\sin\phi_2^* + \sqrt{2}\sin\phi_2^* - \sqrt{2}A^2\sin\phi_1^* + \sqrt{2}\sin\phi_2^*\Big] \\
\lambda_2 &= \frac{\mu}{4\sqrt{2}A}\Big[\big((2A^4 - 4A^2 - 2)\cos(\phi_2^* + \phi_1^*) + (-2A^4 + 4A^2 + 2)\cos(\phi_2^* - \phi_1^*) \\
&\quad +(-A^4 + 2A^2 - 1)\cos(2\phi_2^*) + (-A^4 + 2A^2 - 1)\cos(2\phi_1^*) + 2A^4 - 4A^2 \\
&\quad +2\big)^{\frac{1}{2}} + \sqrt{2}A^2\sin\phi_2^* - \sqrt{2}\sin\phi_2^* + \sqrt{2}A^2\sin\phi_1^* - \sqrt{2}\sin\phi_2^*\Big]
\end{aligned}$$

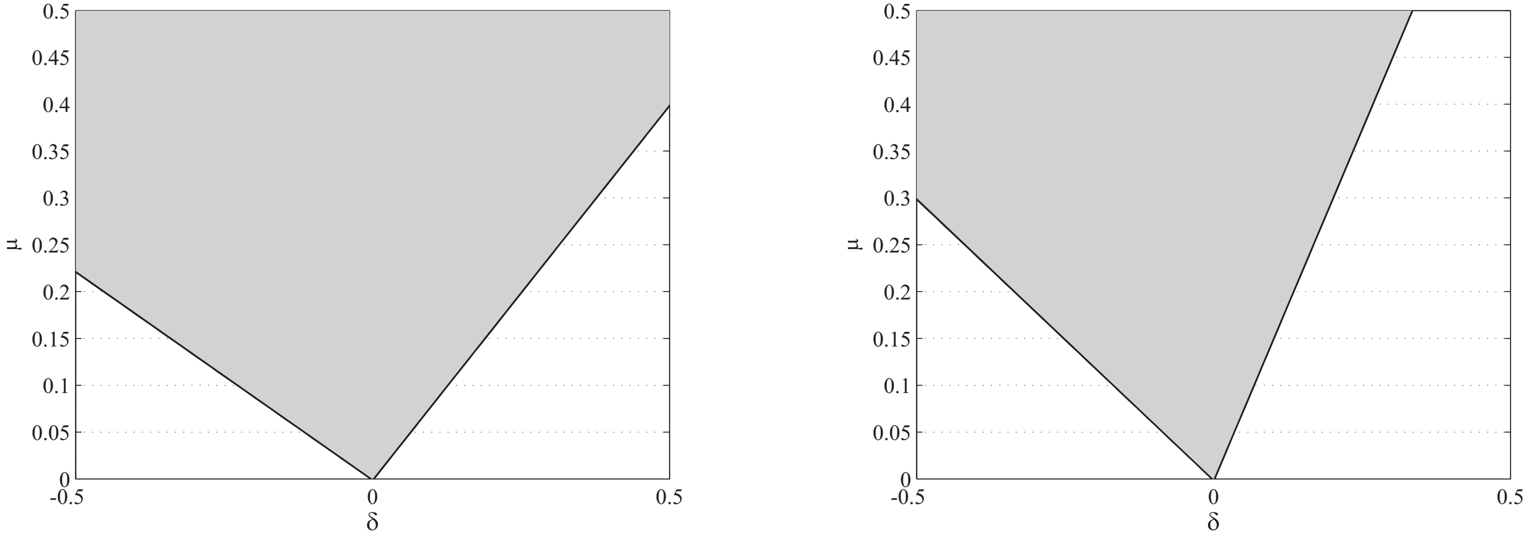

Figure 4.4: Regions of δ-μ parameter space where phase-locked motions exist for (4.7) when $A = \frac{1}{2}$ (left) and $A = 3$ (right). Outside these regions there exist only drift motions. phase-locking region = gray.

Table 4.3: The 4 equilibrium points of the flow (4.7).

EQPT	(ϕ_1^*,ϕ_2^*)
1	$\left(\pi - \cos^{-1}\left(\frac{A(\mu+2\delta)}{(A^2-2)\mu}\right), \pi - \cos^{-1}\left(\frac{A(\mu+2\delta)}{(A^2-2)\mu}\right)\right)$
2	$\left(\pi + \cos^{-1}\left(\frac{A(\mu+2\delta)}{(A^2-2)\mu}\right), \pi + \cos^{-1}\left(\frac{A(\mu+2\delta)}{(A^2-2)\mu}\right)\right)$
3	$\left(\pi - \cos^{-1}\left(\frac{A(\mu+2\delta)}{(A^2-2)\mu}\right), \pi + \cos^{-1}\left(\frac{A(\mu+2\delta)}{(A^2-2)\mu}\right)\right)$
4	$\left(\pi + \cos^{-1}\left(\frac{A(\mu+2\delta)}{(A^2-2)\mu}\right), \pi - \cos^{-1}\left(\frac{A(\mu+2\delta)}{(A^2-2)\mu}\right)\right)$

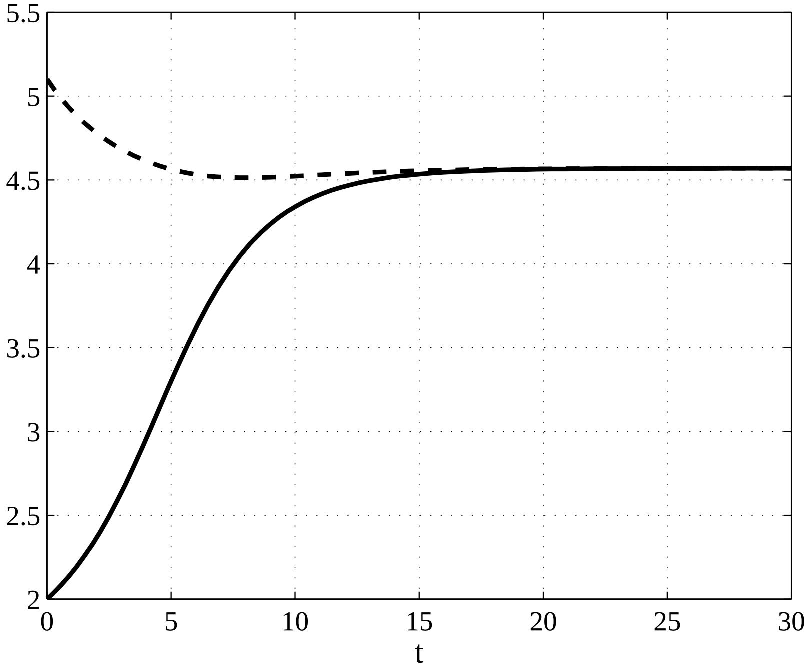

Figure 4.5: Numerical integration for (4.7) with parameter values $A = 3, \delta = -0.1$, $\mu = 0.3$ exhibiting a stable phase-locked in-phase mode (EQPT2). $\phi_1(t)$ = solid line; $\phi_2(t)$ = dashed line.

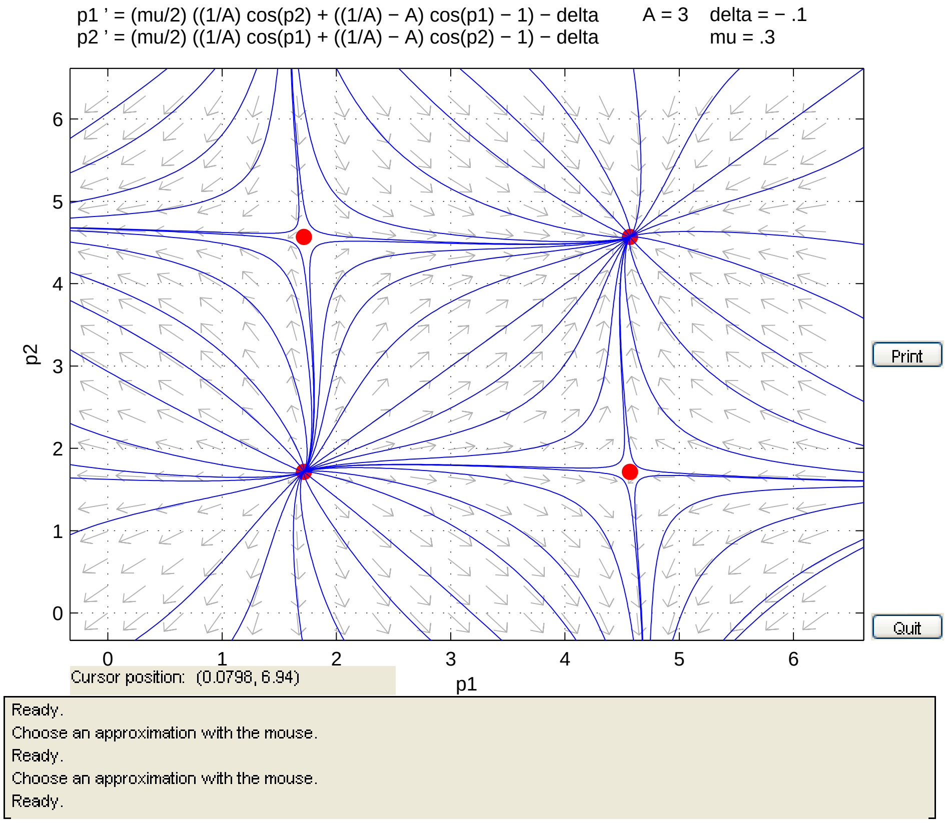

p1 ' = (mu/2) ((1/A) cos(p2) + ((1/A) − A) cos(p1) − 1) − delta   A = 3   delta = − .1
p2 ' = (mu/2) ((1/A) cos(p1) + ((1/A) − A) cos(p2) − 1) − delta   mu = .3

Cursor position: (0.0798, 6.94)

Ready.
Choose an approximation with the mouse.
Ready.
Choose an approximation with the mouse.
Ready.

Figure 4.6: Phase diagram [15] for (4.7) with parameter values $A = 3, \delta = -0.1, \mu = 0.3$. There exist 4 equilibrium points – 1 in-phase source (EQPT1), 1 in-phase sink (EQPT2) and 2 non-in-phase saddles (EQPT3 and EQPT4).

We simplify these expressions using Table 4.3 and trigonometric identities to

$$\begin{aligned}\lambda_1 &= -\frac{\mu\sqrt{A^2-2}}{2\sqrt{2}}\sqrt{1-\cos(2x)} \\ \lambda_2 &= \frac{\mu\sqrt{A^2-2}}{2\sqrt{2}}\sqrt{1-\cos(2x)}\end{aligned}$$

for both EQPT3 and EQPT4, where

$$x = \pi - \cos^{-1}\left(\frac{A(\mu+2\delta)}{(A^2-2)\mu}\right)$$

Note that $\lambda_1 = -\lambda_2$. Once again there are two cases to consider - $A < \sqrt{2}$ and $A > \sqrt{2}$. For the former case the factor $\sqrt{A^2-2}$ will be imaginary and EQPT3 and EQPT4 will be nonlinear centers. In the latter case this factor will be real and EQPT3 and EQPT4 will be saddles (see Figure 4.6).

Unlike the first coupled phase oscillator model (4.2), this model exhibits behavior similar to that of the experiments. In particular, there exists a region of parameter space defined by (4.10) and $A > \sqrt{2}$ where there exists a stable phase-locked in-phase mode for (4.7). Furthermore, there exist no other stable dynamical features in this region. This model highlights the possible importance of the amplitudes of the respective oscillators for the existence of a stable phase-locked in-phase mode for the weakly coupled VDP system (2.1). Also, two qualitative comparisons can be made between this model and the weakly coupled VDP model (2.1). First, for both models the region of parameter space where stable phase-locked in-phase modes exist is not symmetric about the $\delta = 0$ axis but shifted left towards the second quadrant of parameter space. For this system this region exists exclusively for $\delta < 0$ when $\sqrt{2} < A < 2$. Secondly, this system exhibits only a single stable phase-locked in-phase mode while the VDP system exhibits two stable phase-locked in-phase modes for certain regions of parameter space.

We believe the success, according to our definition, of this model provides incentive for further study of more general phase oscillator models for the avian circadian system.

Chapter 5
Three Strongly Coupled VDP Oscillators

In Chapters 2 and 3 we investigated the dynamics in the in-phase subspace of the weakly coupled and detuned VDP system (2.1) via the two-variable expansion perturbation method and numerical Floquet theory and successfully determined regions of parameter space where stable phase-locked in-phase modes for (2.1) exist. Unfortunately we cannot expand our analysis to the complete dynamics of (2.1) due to computational complexity as a result of the 5-dimensional slow-flow's large dimensional size.

As an alternative to the VDP model, in Chapter 4 we proposed two simpler, lower dimensional coupled phase oscillator models for which we could study the complete dynamics. Now in this chapter we return to the VDP model but now consider the oscillators to be strongly coupled and detuned. This change in parameter regimes has the significant effect of simplifying the mathematics required for studying the complete dynamics of the system. That is, we will now be able to determine the existence and stability of all motions exhibited by the system and not just those living in the in-phase subspace.

In this chapter we study a system of three strongly coupled weakly-nonlinear ($\epsilon \ll 1$) VDP oscillators (x, y, and w)

$$\begin{aligned} \ddot{x} - \epsilon(1-x^2)\dot{x} + x &= \mu(w-x) \\ \ddot{y} - \epsilon(1-y^2)\dot{y} + y &= \mu(w-y) \\ \ddot{w} - \epsilon(1-w^2)\dot{w} + (1+\Delta)w &= \mu(x+y-2w) \end{aligned} \tag{5.1}$$

where a "dot" denotes differentiation with respect to time t. The x- and y-oscillators are taken to have identical uncoupled linear angular frequencies of unity while that of the w-oscillator is detuned from unity via the parameter Δ. The coupling between the oscillators is linear in the displacements with coupling parameter μ. The coupling and detuning are now considered "strong" in the sense that the parameters Δ and μ are $O(1)$.

Our analysis of (5.1) will differ from that discussed in Chapter 2 in two significant ways. The linear $\epsilon = 0$ system is now comprised of coupled simple harmonic oscillators and we will first need to perform a linear transformation into the linear normal mode coordinates for this system before applying any singular perturbation methods. Also, our bifurcation and stability results will be simplified by the introduction of a new parameter representing the ratio of detuning to coupling in the system.

Our analysis is motivated by and closely follows that of Storti & Rand ([23],[24]) where a similarly defined system of two coupled VDP oscillators was studied (see Chapter 6 for a review of their results).

<u>Linear Normal Modes</u>

We begin by rewriting the system (5.1) in matrix form as

$$\begin{bmatrix} \ddot{x} \\ \ddot{y} \\ \ddot{w} \end{bmatrix} + \begin{bmatrix} 1+\mu & 0 & -\mu \\ 0 & 1+\mu & -\mu \\ -\mu & -\mu & 2\mu+1+\Delta \end{bmatrix} \begin{bmatrix} x \\ y \\ w \end{bmatrix} = \epsilon \left(\begin{bmatrix} 1 & 0 & 0 \\ 0 & 1 & 0 \\ 0 & 0 & 1 \end{bmatrix} - \begin{bmatrix} x^2 & 0 & 0 \\ 0 & y^2 & 0 \\ 0 & 0 & w^2 \end{bmatrix} \right) \begin{bmatrix} \dot{x} \\ \dot{y} \\ \dot{w} \end{bmatrix}$$

or more compactly as

$$\underline{\ddot{\mathbf{u}}} + [A]\,\underline{\mathbf{u}} = \epsilon \left([I] - \left[\chi^2\right] \right) \underline{\dot{\mathbf{u}}} \tag{5.2}$$

where $\underline{\mathbf{u}} = \begin{bmatrix} x(t) & y(t) & w(t) \end{bmatrix}^T$. Setting $\epsilon = 0$, (5.2) reduces to the homogeneous linear system

$$\underline{\ddot{\mathbf{u}}} + [A]\,\underline{\mathbf{u}} = 0 \tag{5.3}$$

We now perform a linear normal mode analysis on (5.3). First we introduce a new parameter, s, defined as

$$s = \frac{\Delta}{2\mu} \tag{5.4}$$

The parameter s can be thought of as a measure of the ratio of detuning to coupling in the system. Next, we define new normal mode coordinates $v_i(t)$ via the linear transformation

$$\underline{\mathbf{u}} = [S]\,\underline{\mathbf{v}} = \begin{bmatrix} 1 & 1 & 1 \\ 1 & -1 & 1 \\ \alpha & 0 & \beta \end{bmatrix} \underline{\mathbf{v}} \tag{5.5}$$

where $\mathbf{v} = \begin{bmatrix} v_1(t) & v_2(t) & v_3(t) \end{bmatrix}^T$, $\alpha = -\frac{1}{2} - s + \sqrt{\frac{9}{4} + s + s^2}$, and $\beta = -\frac{1}{2} - s - \sqrt{\frac{9}{4} + s + s^2}$ (see Figure 5.1 for a comparison between α and β). Each column of the transformation (or change-of-basis) matrix $[S]$ is by definition an eigenvector of the matrix $[A]$. From left to right, and smallest to largest, the eigenvalues associated with each eigenvector are

$$\begin{aligned} \lambda_1 &= 1 + \mu\left(\frac{3}{2} + s - \sqrt{\frac{9}{4} + s + s^2}\right) \\ \lambda_2 &= 1 + \mu \\ \lambda_3 &= 1 + \mu\left(\frac{3}{2} + s + \sqrt{\frac{9}{4} + s + s^2}\right) \end{aligned} \tag{5.6}$$

Notice that while the eigenvalues depend on both μ and s, the transformation matrix $[S]$ depends only on the new parameter s. Furthermore, it is critical to note that the above definitions for α, β, λ_1, and λ_3 are correct *only* when restricting $\mu > 0$. For example, letting α^+ and α^- denote the values of α for positive and negative μ respectively, we find that $\alpha^+ = \alpha$ and $\alpha^- = \beta$. Likewise, for the other variables we have $\beta^- = \alpha$, $\lambda_1^- = \lambda_3$, and $\lambda_3^- = \lambda_1$.

Rewriting (5.2) in terms of the normal mode coordinates we have

$$[S]\,\ddot{\underline{\mathbf{v}}} + [A]\,[S]\,\underline{\mathbf{v}} = \epsilon\left([I] - \left[\chi^2\right]\right)[S]\,\dot{\underline{\mathbf{v}}}$$

where the appropriate substitutions have been made (via (5.5)) in the matrix $[\chi^2]$. Left multiplying both sides by $[S^{-1}]$ then yields

$$\ddot{\underline{\mathbf{v}}} + [\Lambda]\underline{\mathbf{v}} = \epsilon[S^{-1}]\left([I] - [\chi^2]\right)[S]\dot{\underline{\mathbf{v}}} \tag{5.7}$$

where $[\Lambda]$ is a diagonal matrix whose entries are the eigenvalues (5.6) of matrix $[A]$.

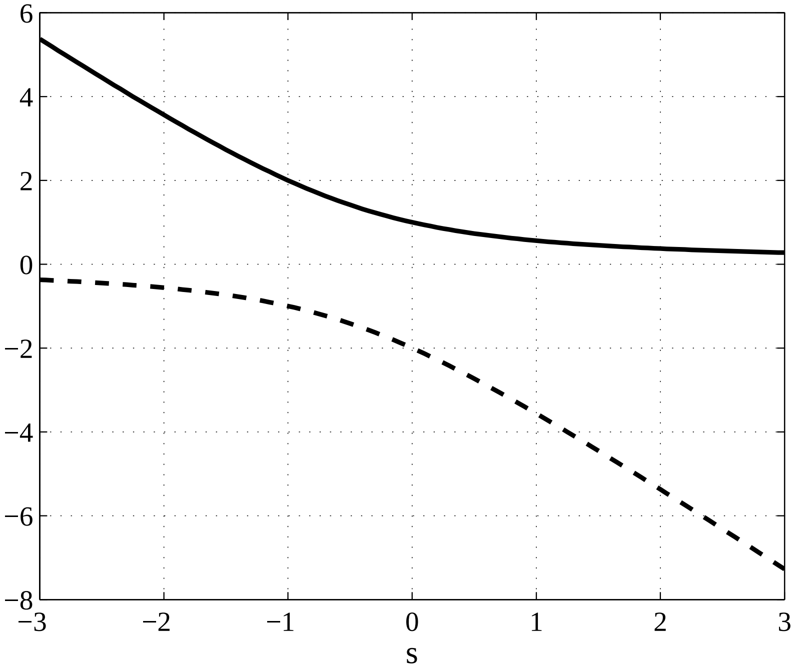

Figure 5.1: Comparison between α (solid line) and β (dashed line) terms that appear in the definition of the change-of-basis matrix $[S]$ for $\mu > 0$. Switch curves for $\mu < 0$.

PERTURBATION EXPANSION

The system (5.7) is now in a better form for the application of the two-variable expansion singular perturbation method [17]. We begin by defining two new time-scales. The first, slow-time, is defined as $\eta(t) = \epsilon t$, while the second, strained-time, is defined as $\xi(t) = \Omega t$. The frequency Ω is then expanded as $\Omega = 1 + \epsilon k_1 + O(\epsilon^2)$ to build in the frequency-amplitude relationship characteristic of nonlinear oscillators. Our analysis will be to $O(\epsilon)$ and all higher-order terms will be dropped.

We now consider our normal mode coordinates to be functions of these two new time-scales, i.e. $\underline{\mathbf{v}}(\eta, \xi)$. To differentiate $\underline{\mathbf{v}}$ with respect to time t we use the chain-rule to get

$$\dot{\underline{\mathbf{v}}} = \frac{d\underline{\mathbf{v}}}{d\xi}\dot{\xi} + \frac{d\underline{\mathbf{v}}}{d\eta}\dot{\eta} = \Omega\frac{d\underline{\mathbf{v}}}{d\xi} + \epsilon\frac{d\underline{\mathbf{v}}}{d\eta} = (1 + \epsilon k_1)\frac{d\underline{\mathbf{v}}}{d\xi} + \epsilon\frac{d\underline{\mathbf{v}}}{d\eta} + O(\epsilon^2) \tag{5.8}$$

Differentiating a second time gives

$$\ddot{\underline{\mathbf{v}}} = \Omega^2\frac{d^2\underline{\mathbf{v}}}{d\xi^2} + 2\epsilon\Omega\frac{d^2\underline{\mathbf{v}}}{d\xi d\eta} + O(\epsilon^2) = (1 + 2\epsilon k_1)\frac{d^2\underline{\mathbf{v}}}{d\xi^2} + 2\epsilon\frac{d^2\underline{\mathbf{v}}}{d\xi d\eta} + O(\epsilon^2) \tag{5.9}$$

Next, we expand our solution $\underline{\mathbf{v}}(\eta, \xi)$ as a power series in ϵ

$$\underline{\mathbf{v}}(\eta, \xi) = \underline{\mathbf{v}}_{\mathbf{0}}(\eta, \xi) + \epsilon\underline{\mathbf{v}}_{\mathbf{1}}(\eta, \xi) + O(\epsilon^2) \tag{5.10}$$

We now substitute (5.8), (5.9), and (5.10) into (5.7) and multiply everything out, keeping only terms of $O(\epsilon)$ or lower. The procedure now calls for equating the coefficients of each power of ϵ to zero. The lowest order equations are of the form

$$\frac{d^2 v_{i0}}{d\xi^2} + \omega_i^2 v_{i0} = 0$$

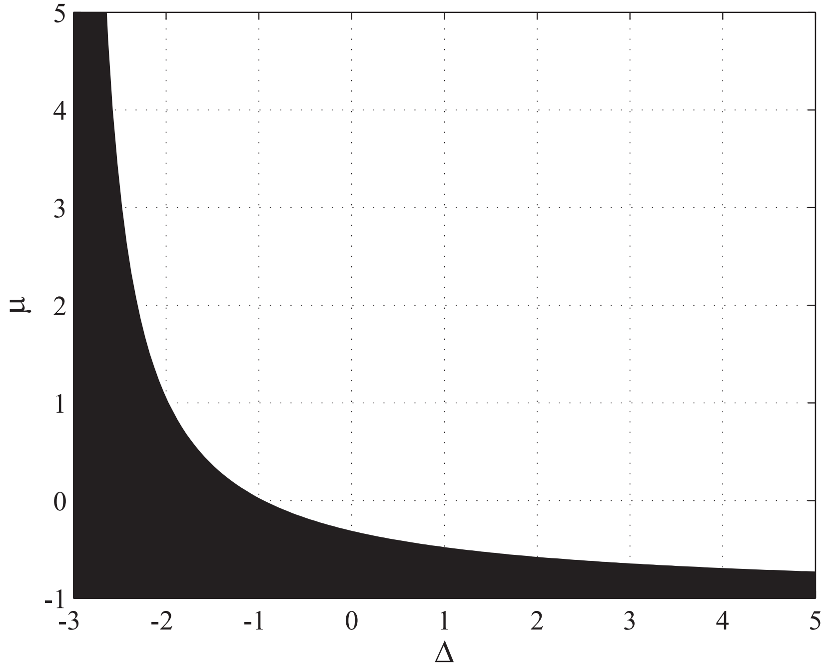

Figure 5.2: Plot of equation (5.12). The black region represents parameter values where our analysis is not valid due to the lowest order solutions (5.11) becoming non-oscillatory.

where $\omega_i = \sqrt{\lambda_i}$ and λ_i is the i^{th} eigenvalue of matrix $[A]$, as given in (5.6). These equations represent simple harmonic oscillators and we write their solutions in polar form as

$$v_{i0}(\eta, \xi) = R_i(\eta) \cos(\omega_i \xi - \theta_i(\eta)) \tag{5.11}$$

where the constants of integration (the amplitudes R_i and phases θ_i) are functionally dependent on slow-time. For the lowest order solutions (5.11) to remain oscillatory the eigenvalues (5.6) must remain positive. This restricts the validity of our analysis to a region of Δ-μ parameter space bounded by the curve (see Figures 5.2 and 5.3)

$$\mu = -\frac{\Delta + 1}{\Delta + 3} \tag{5.12}$$

Next we substitute (5.11) into the $O(\epsilon)$ equations. After some trigonometric sim-

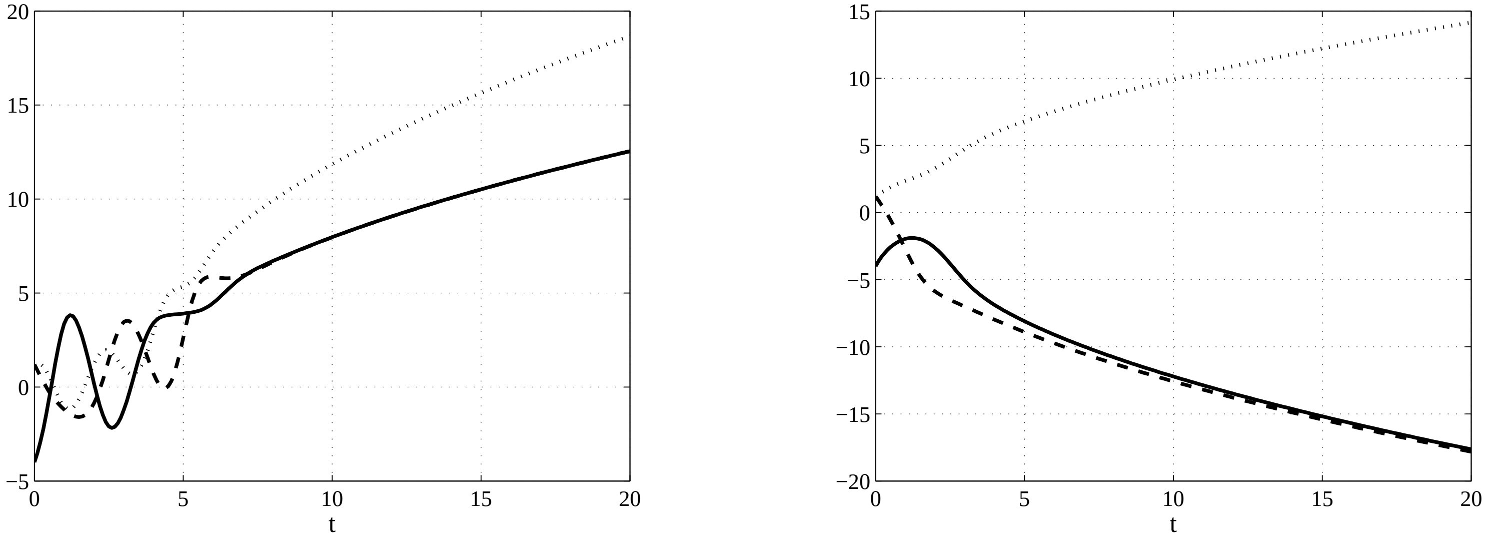

Figure 5.3: Numerical integrations (with $\epsilon = 0.1$) for the system (5.1) with parameter values $\Delta = -4$, $\mu = 3$ (left) and $\Delta = 3$, $\mu = -1$ (right). These parameter pairs lie outside the region of validity defined by (5.12) and our perturbation analysis would be incorrect since we assume the lowest-order solutions (5.11) to be harmonic oscillators. $x(t)$ = solid line; $y(t)$ = dashed line; $w(t)$ = dotted line.

plification, the resulting equations are of the form

$$\frac{d^2 v_{i1}}{d\xi^2} + \omega_i^2 v_{i1} = (...) \cos(\omega_i \xi) + (...) \sin(\omega_i \xi) + (...) \tag{5.13}$$

where the (...) in front of the trig terms represent constant, i.e. independent of ξ, equations of coefficients involving R_i, θ_i, and their respective derivatives. The (...) at the end of each equation represents equations of non-secular trig terms, i.e. terms whose frequencies are linear combinations of ω_1, ω_2, and ω_3 (see Appendix C for a full list of these terms). For the slow-flow equations to be uniformly valid for all time we must eliminate the secular $\cos(\omega_i \xi)$ and $\sin(\omega_i \xi)$ terms from the right-hand side of (5.13). Note that in determining secular terms we are ignoring the possibility that for certain parameter values additional terms may become secular. These special cases will be discussed in the final section of this chapter.

The elimination of secular terms results in six equations in six unknowns - $\frac{dR_i}{d\eta}$ and $\frac{d\theta_i}{d\eta}$ for $i = 1, 2, 3$ (see (5.14) and (5.15)). Solving these equations for the unknowns yields the polar slow-flow. However, we can simplify the polar slow-flow by changing dependent variables to the squares of the amplitudes. Defining $\rho_i = R_i^2$ and differentiating with respect to slow-time η we get

$$\frac{d\rho_i}{d\eta} = \frac{d\rho_i}{dR_i}\frac{dR_i}{d\eta} = 2R_i \frac{dR_i}{d\eta}$$

$$
\begin{aligned}
&-\frac{\omega_1}{4(\beta-\alpha)}\Bigg[8\beta k_1\cos\theta_1 R_1\omega_1 - 8\alpha k_1\cos\theta_1 R_1\omega_1 + 2\alpha\beta^2\sin\theta_1 R_1 R_3^2 - 2\beta\sin\theta_1 R_1 R_3^2 - 2\beta\sin\theta_1 R_1 R_2^2 - 8\beta\sin\theta_1\frac{dR_1}{d\eta}\\
&+8\alpha\sin\theta_1\frac{dR_1}{d\eta} - \beta\sin\theta_1 R_1^3 + \alpha^3\sin\theta_1 R_1^3 - 8\beta\cos\theta_1\frac{d\theta_1}{d\eta}R_1 + 8\alpha\cos\theta_1\frac{d\theta_1}{d\eta}R_1 + 4\beta\sin\theta_1 R_1 - 4\alpha\sin\theta_1 R_1\Bigg] = 0
\end{aligned}
$$

$$
-\frac{\omega_2}{4}\left[8k_1\cos\theta_2 R_2\omega_2 - 2\sin\theta_2 R_2 R_3^2 - 8\sin\theta_2\frac{dR_2}{d\eta} - \sin\theta_2 R_2^3 - 2\sin\theta_2 R_1^2 R_2 - 8\cos\theta_2\frac{d\theta_2}{d\eta}R_2 + 4\sin\theta_2 R_2\right] = 0
$$

$$
\begin{aligned}
&-\frac{\omega_3}{4(\beta-\alpha)}\Bigg[8\beta k_1\cos\theta_3 R_3\omega_3 - 8\alpha k_1\cos\theta_3 R_3\omega_3 - 8\beta\sin\theta_3\frac{dR_3}{d\eta} + 8\alpha\sin\theta_3\frac{dR_3}{d\eta} - \beta^3\sin\theta_3 R_3^3 + \alpha\sin\theta_3 R_3^3 + 2\alpha\sin\theta_3 R_2^2 R_3\\
&-2\alpha^2\beta\sin\theta_3 R_1^2 R_3 + 2\alpha\sin\theta_3 R_1^2 R_3 - 8\beta\cos\theta_3\frac{d\theta_3}{d\eta}R_3 + 8\alpha\cos\theta_3\frac{d\theta_3}{d\eta}R_3 + 4\beta\sin\theta_3 R_3 - 4\alpha\sin\theta_3 R_3\Bigg] = 0 \qquad (5.14)
\end{aligned}
$$

$$
\begin{aligned}
&-\frac{\omega_1}{4(\beta-\alpha)}\Bigg[8\beta k_1\sin\theta_1 R_1\omega_1-8\alpha k_1\sin\theta_1 R_1\omega_1-2\alpha\beta^2\cos\theta_1 R_1R_3^2+2\beta\cos\theta_1 R_1R_3^2+2\beta\cos\theta_1 R_1R_2^2+8\beta\cos\theta_1\frac{dR_1}{d\eta}\\
&-8\alpha\cos\theta_1\frac{dR_1}{d\eta}+\beta\cos\theta_1 R_1^3-\alpha^3\cos\theta_1 R_1^3-8\beta\sin\theta_1\frac{d\theta_1}{d\eta}R_1+8\alpha\sin\theta_1\frac{d\theta_1}{d\eta}R_1-4\beta\cos\theta_1 R_1+4\alpha\cos\theta_1 R_1\Bigg]=0
\end{aligned}
$$

$$
-\frac{\omega_2}{4}\Bigg[8k_1\sin\theta_2 R_2\omega_2+2\cos\theta_2 R_2R_3^2+8\cos\theta_2\frac{dR_2}{d\eta}+\cos\theta_2 R_2^3+2\cos\theta_2 R_1^2R_2-8\sin\theta_2\frac{d\theta_2}{d\eta}R_2-4\cos\theta_2 R_2\Bigg]=0
$$

$$
\begin{aligned}
&-\frac{\omega_3}{4(\beta-\alpha)}\Bigg[8\beta k_1\sin\theta_3 R_3\omega_3-8\alpha k_1\sin\theta_3 R_3\omega_3+8\beta\cos\theta_3\frac{dR_3}{d\eta}-8\alpha\cos\theta_3\frac{dR_3}{d\eta}+\beta^3\cos\theta_3 R_3^3-\alpha\cos\theta_3 R_3^3-2\alpha\cos\theta_3 R_2^2R_3\\
&+2\alpha^2\beta\cos\theta_3 R_1^2R_3-2\alpha\cos\theta_3 R_1^2R_3-8\beta\sin\theta_3\frac{d\theta_3}{d\eta}R_3+8\alpha\sin\theta_3\frac{d\theta_3}{d\eta}R_3-4\beta\cos\theta_3 R_3+4\alpha\cos\theta_3 R_3\Bigg]=0 \qquad (5.15)
\end{aligned}
$$

Rewriting the polar slow-flow in terms of ρ_i yields

$$\begin{aligned}
\frac{d\rho_1}{d\eta} &= \rho_1\left[A\rho_1 + B\rho_2 + C\rho_3 + 1\right] \\
\frac{d\rho_2}{d\eta} &= \rho_2\left[-\frac{1}{2}\rho_1 - \frac{1}{4}\rho_2 - \frac{1}{2}\rho_3 + 1\right] \\
\frac{d\rho_3}{d\eta} &= \rho_3\left[D\rho_1 + E\rho_2 + F\rho_3 + 1\right] \\
\frac{d\theta_i}{d\eta} &= k_1\omega_i
\end{aligned}$$

for $i = 1, 2, 3$ and where the coefficients $A = \frac{\alpha^3-\beta}{4(\beta-\alpha)}$, $B = \frac{-\beta}{2(\beta-\alpha)}$, $C = \frac{\beta(\alpha\beta-1)}{2(\beta-\alpha)}$, $D = \frac{-\alpha(\alpha\beta-1)}{2(\beta-\alpha)}$, $E = \frac{\alpha}{2(\beta-\alpha)}$, and $F = \frac{\alpha-\beta^3}{4(\beta-\alpha)}$ depend only on the parameter s.

We can reduce the dimension of the polar slow-flow by directly integrating the slow-flow phase equations to get

$$\theta_i(\eta) = k_1\omega_i\eta + \phi_i \tag{5.16}$$

where the ϕ_i are the constants of integration. Substituting (5.16) into (5.11) yields

$$v_{i0}(\eta,\xi) = R_i(\eta)\cos\left(\omega_i\xi - (k_1\omega_i\eta + \phi_i)\right) = R_i(\eta)\cos\left(\omega_i t - \phi_i\right) \tag{5.17}$$

where we have used the definitions of slow-time and strained-time. Thus, to $O(\epsilon)$, the lowest-order approximations to the normal modes contain no frequency-amplitude dependence and oscillate on the normal time-scale with constant phase.

Our final 3-dimensional slow-flow is now

$$\begin{aligned}
\frac{d\rho_1}{d\eta} &= \rho_1 \left[A\rho_1 + B\rho_2 + C\rho_3 + 1\right] \\
\frac{d\rho_2}{d\eta} &= \rho_2 \left[-\frac{1}{2}\rho_1 - \frac{1}{4}\rho_2 - \frac{1}{2}\rho_3 + 1\right] \\
\frac{d\rho_3}{d\eta} &= \rho_3 \left[D\rho_1 + E\rho_2 + F\rho_3 + 1\right]
\end{aligned} \tag{5.18}$$

Bifurcation and Stability Analysis

The form of the final slow-flow (5.18) allows for easy investigation of equilibrium points and their respective stabilities. Since each equation is quadratic in its respective variable there should exist at most 8 equilibrium points. Using MACSYMA we set the right-hand side of (5.18) equal to 0 and solve for ρ_1, ρ_2, and ρ_3 in closed-form (see Table 5.1). Recall that by definition ρ_i $(i = 1, 2, 3)$ are the squares of amplitudes. Thus one restriction we have on the existence of these equilibrium points is that their respective coordinates must remain positive. A second restriction is that they cannot exist for parameter values where their denominator vanishes.

The stability of an equilibrium point $(\rho_1, \rho_2, \rho_3) = (\rho_1^*, \rho_2^*, \rho_3^*)$ is determined by linearizing the slow-flow in the neighborhood of the equilibrium and investigating the eigenvalues of the linearized flow. The Jacobian of (5.18) evaluated at the equilibrium point is given by

$$\begin{bmatrix}
2A\rho_1^* + B\rho_2^* + C\rho_3^* + 1 & B\rho_1^* & C\rho_1^* \\
-\frac{\rho_2^*}{2} & -\frac{\rho_1^*}{2} - \frac{\rho_2^*}{2} - \frac{\rho_3^*}{2} + 1 & -\frac{\rho_2^*}{2} \\
D\rho_3^* & E\rho_3^* & D\rho_1^* + E\rho_2^* + 2F\rho_3^* + 1
\end{bmatrix} \tag{5.19}$$

An equilibrium point is considered stable if all the eigenvalues of (5.19) have neg-

Table 5.1: The 8 equilibrium points of the slow-flow (5.18).

EQPT	(ρ_1,ρ_2,ρ_3)
1	$(0,0,0)$
2	$\left(0,0,-\frac{1}{F}\right)$
3	$\left(-\frac{1}{A},0,0\right)$
4	$\left(-\frac{F-C}{AF-CD},0,\frac{D-A}{AF-CD}\right)$
5	$(0,4,0)$
6	$\left(0,\frac{4F+2}{F-2E},-\frac{4E+1}{F-2E}\right)$
7	$\left(\frac{4B+1}{2B-A},-\frac{4A+2}{2B-A},0\right)$
8	Omitted due to length.

ative real parts. Because the Jacobian matrix and all the equilibrium points depend solely on the parameter s, we can view the stability results in a simple 1-dimensional diagram (see Figure 5.4).

For each value of s in Figure 5.4 where a change of stability occurs we can use (5.4) to find a proportional relationship between Δ and μ. Each of these lines represents a bifurcation curve in Δ-μ parameter space and will divide the space into several regions, each with distinct dynamical behavior (see Figure 5.5).

Combining the stability results from Figure 5.4 with the bifurcation curves from Figure 5.5, we can create a table summarizing the stability of each equilibrium point in each region of parameter space (see Table 5.2). This table allows us to easily identify the types of bifurcations that occur as we transition between regions of parameter space. For example, when transitioning from Region IIIa to Region IIIb1, EQPT3 and EQPT7 undergo a supercritical pitchfork bifurcation. Likewise, transitioning from Region VIIIc to Region IX destroys EQPT4 in a saddle bifurcation.

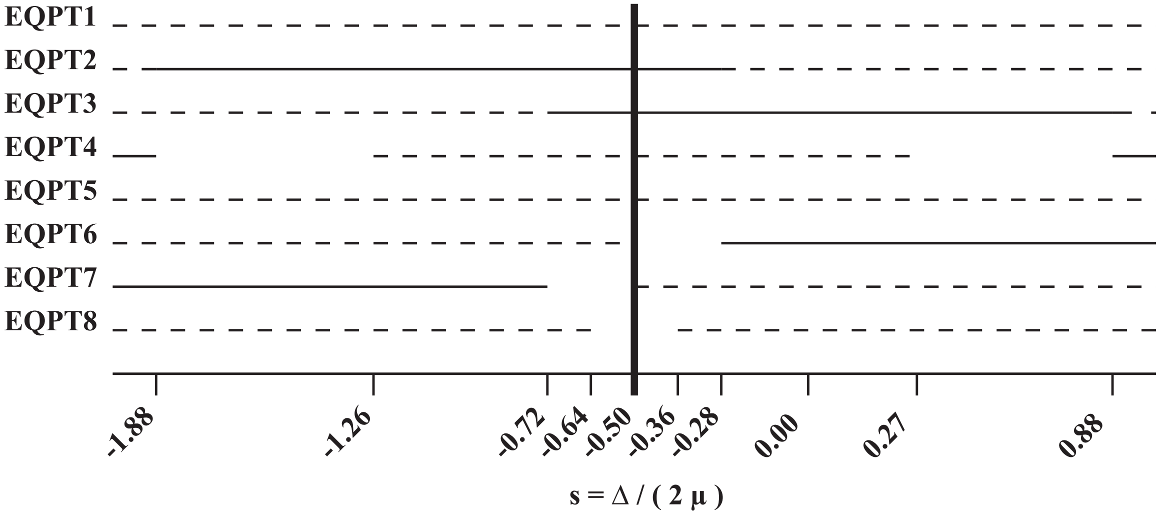

Figure 5.4: 1-dimensional stability chart for equilibrium points of the slow-flow (5.18) when $\mu > 0$. For $\mu < 0$ switch results for EQPT2 and EQPT3, and also for EQPT6 and EQPT7. stable = solid line; unstable = dashed line; non-existent = no line. Not drawn to scale.

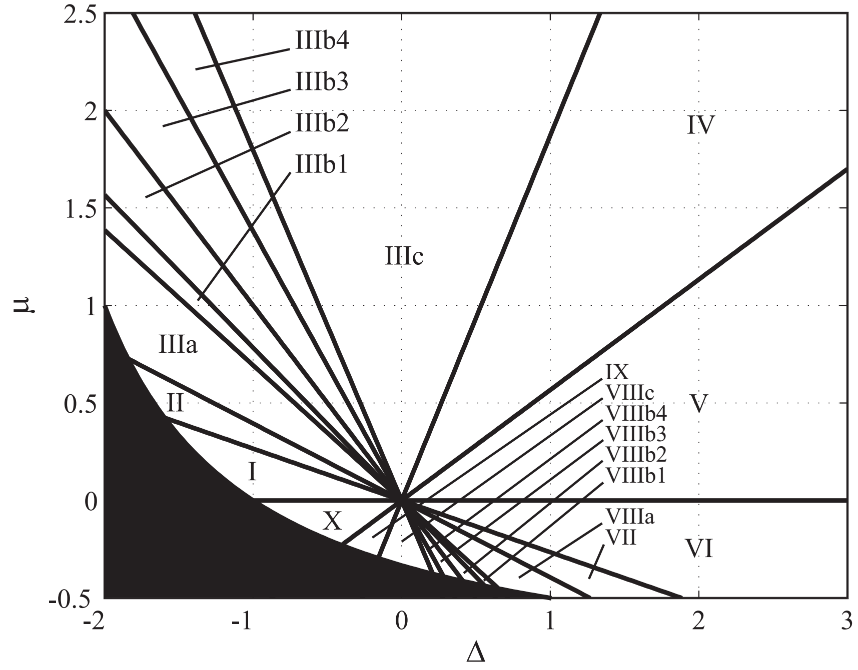

Figure 5.5: Bifurcation curves for the slow-flow (5.18) in Δ-μ parameter space. The black region represents parameter values where our analysis is not valid.

Table 5.2: Stability for equilibrium points of the slow-flow (5.18) in different regions of Δ-μ parameter space. stable = S; unstable = U; non-existent = X.

REGION	EQPT1	EQPT2	EQPT3	EQPT4	EQPT5	EQPT6	EQPT7	EQPT8
I	U	U	U	S	U	U	S	U
II	U	S	U	X	U	U	S	U
IIIa	U	S	U	U	U	U	S	U
IIIb1	U	S	S	U	U	U	X	U
IIIb2	U	S	S	U	U	U	X	X
IIIb3	U	S	S	U	U	X	U	X
IIIb4	U	S	S	U	U	X	U	U
IIIc	U	U	S	U	U	S	U	U
IV	U	U	S	X	U	S	U	U
V	U	U	U	S	U	S	U	U
VI	U	U	U	S	U	S	U	U
VII	U	U	S	X	U	S	U	U
VIIIa	U	U	S	U	U	S	U	U
VIIIb1	U	S	S	U	U	X	U	U
VIIIb2	U	S	S	U	U	X	U	X
VIIIb3	U	S	S	U	U	U	X	X
VIIIb4	U	S	S	U	U	U	X	U
VIIIc	U	S	U	U	U	U	S	U
IX	U	S	U	X	U	U	S	U
X	U	U	U	S	U	U	S	U

Discussion

Knowing the existence and stability of the equilibrium points for the slow-flow (5.18), we now transform back into the original x-, y-, and w-coordinates to understand their dynamical significance. In particular we look at two special invariant subspaces of (5.1) – the in-phase subspace defined by $x(t) = y(t)$ and the out-of-phase subspace defined by $x\left(t\right) = -y\left(t\right)$.

The in-phase subspace is given by

$$\begin{aligned} \ddot{x} - \epsilon\left(1 - x^2\right)\dot{x} + x &= \mu\left(w - x\right) \\ \ddot{w} - \epsilon\left(1 - w^2\right)\dot{w} + (1 + \Delta)w &= 2\mu\left(x - w\right) \end{aligned}$$

and exists for all parameter values. In terms of the normal mode coordinates the in-phase subspace becomes (via the inverse of (5.5))

$$\begin{bmatrix} v_1 \\ v_2 \\ v_3 \end{bmatrix} = \begin{bmatrix} \frac{2\beta x}{2(\beta-\alpha)} - \frac{w}{\beta-\alpha} \\ 0 \\ -\frac{2\alpha x}{2(\beta-\alpha)} + \frac{w}{\beta-\alpha} \end{bmatrix}$$

In the normal mode coordinates the subspace satisfies $v_2(t) = 0$, or in terms of the slow-flow, the two-dimensional invariant subspace defined by $\rho_2 = 0$. Therefore equilibrium points with $\rho_2 = 0$ (EQPT2 through EQPT4) represent in-phase modes for (5.1).

Next we look at the out-of-phase subspace. This subspace is given by

$$\begin{aligned} \ddot{x} - \epsilon\left(1 - x^2\right)\dot{x} + (1 + \mu)x &= 0 \\ w &= 0 \end{aligned}$$

In terms of the normal mode coordinates we have

$$\begin{bmatrix} v_1 \\ v_2 \\ v_3 \end{bmatrix} = \begin{bmatrix} 0 \\ x \\ 0 \end{bmatrix}$$

Thus the out-of-phase subspace is given by $v_1(t) = v_3(t) = 0$. This is equivalent to the 1-dimensional invariant subspace of the ρ_2-axis in the slow-flow. EQPT5 is the only equilibrium point representing an out-of-phase mode for (5.1).

Transforming back into the original coordinate system using (5.5) we have

$$\begin{aligned}
x(t) &= v_1(t) + v_2(t) + v_3(t) \\
&= R_1(\epsilon t)\cos(\omega_1 t - \phi_1) + R_2(\epsilon t)\cos(\omega_2 t - \phi_2) + R_3(\epsilon t)\cos(\omega_3 t - \phi_3) \\
y(t) &= v_1(t) - v_2(t) + v_3(t) \\
&= R_1(\epsilon t)\cos(\omega_1 t - \phi_1) - R_2(\epsilon t)\cos(\omega_2 t - \phi_2) + R_3(\epsilon t)\cos(\omega_3 t - \phi_3) \\
w(t) &= \alpha v_1(t) + \beta v_3(t) \\
&= \alpha R_1(\epsilon t)\cos(\omega_1 t - \phi_1) + \beta R_3(\epsilon t)\cos(\omega_3 t - \phi_3)
\end{aligned}$$

Phase-locked motions in the original system will consist of motions comprised of only a single mode, i.e. motions corresponding to slow-flow equilibrium points with 2 coordinates set equal to zero. In particular, equilibrium points EQPT2 and EQPT3 will correspond to phase-locked in-phase modes that are out-of-phase (in-phase) and in-phase (out-of-phase) with the w-oscillator respectively when $\mu > 0$ ($\mu < 0$). The remaining equilibrium points will in general correspond to quasi-periodic motions. Table 5.3 summarizes the various dynamical behaviors the slow-flow equilibrium points correspond to.

Table 5.3: Descriptions of the dynamical behaviors the slow-flow equilibrium points correspond to for $\mu > 0$.

EQPT	Description of Dynamical Behavior
1	trivial solution
2	x- and y-oscillators in-phase, out-of-phase with w-oscillator
3	x- and y-oscillators in-phase, in-phase with w-oscillator
4	x- and y-oscillators in-phase, quasi-periodic behavior
5	x- and y-oscillators out-of-phase, w-oscillator turned off
6,7,8	quasi-periodic behavior

According to Table 5.2 stable phase-locked in-phase modes for (5.1) exist in Regions II, IIIa - IIIc, and IV (for $\mu > 0$). Furthermore Regions IIIb1 through IIIb4 contain distinct stable phase-locked in-phase modes and no other stable dynamical features (see Figure 5.6). Therefore we can conclude that the strongly coupled and detuned VDP system (5.1) exhibits behavior like that of the experiments.

The regions containing two stable phase-locked in-phase modes and no other stable motions exist only when the x- and y- oscillators have a higher uncoupled natural frequency (i.e. $\Delta < 0$) than the w-oscillator (when $\mu > 0$). This is similar to results for the second coupled phase oscillator model (4.7) (when $\sqrt{2} < A < 2$) discussed in the previous chapter and it is tempting to assume that this is true as well for the weakly coupled and detuned VDP system (2.1) discussed in CHAPTER 2. A mathematical explanation for this could be that the even (cosine) coupling between the phase-difference variables in both the slow-flow (5.18) and the second phase oscillator model (4.7) cause the phase-locking region where only stable in-phase modes are found to exist only when the identical $\Delta < 0$. Had we instead used velocity coupling in our model (which would result in odd sine coupling between phase-difference variables ([16],[8])) perhaps our results would be different. Unfortunately the biological significance of this result is also unknown.

Figures 5.7 and 5.8 show the amplitudes and frequencies (respectively) for the

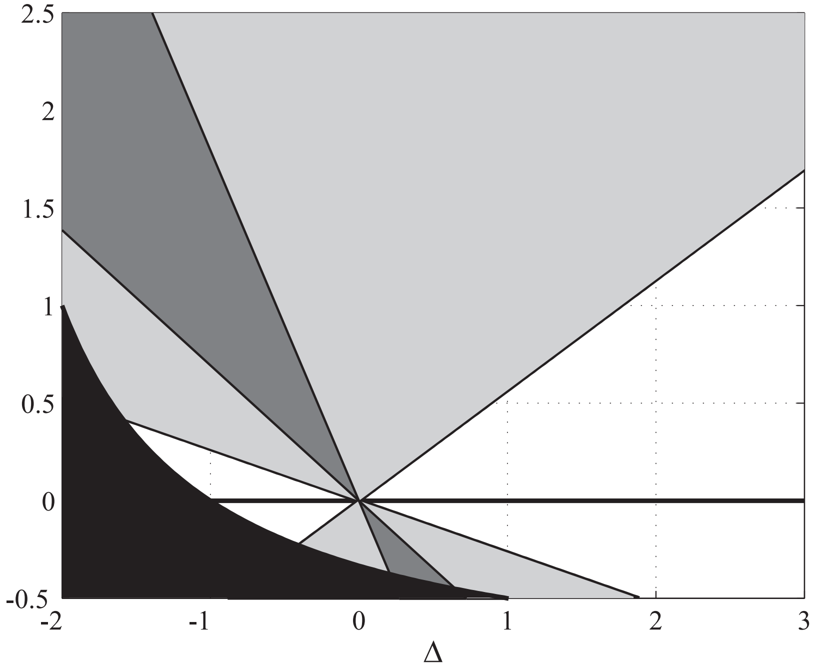

Figure 5.6: Regions of Δ-μ parameter space where stable phase-locked in-phase motions exist. light gray = 1 stable phase-locked in-phase motion plus stable quasi-periodic motion; dark gray = 2 stable phase-locked in-phase motions; black = analysis not valid.

stable phase-locked in-phase modes in Regions IIIb1 through IIIb4. From Figure 5.7 we see that the amplitudes of the eye oscillators for each motion differ by a factor of less than 2 over the entire parameter range. For the special parameter value of $s = -\frac{1}{2}$ the two motions have equal amplitudes. However, from Figure 5.8 we find that the frequencies of the motions vary significantly over this same region. For a fixed value of s, the frequency difference between the two phase-locked in-phase modes increases as the magnitudes of Δ and μ are increased. Therefore we conclude that the two phase-locked in-phase modes consist of a high-frequency mode that is out-of-phase with the w-oscillator (EQPT2) and a low-frequency mode that is in-phase with the w-oscillator (EQPT3) (when $\mu > 0$).

We now compare our analytical perturbation results to numerical integrations of the original system (5.1) to determine whether two distinct stable phase-locked

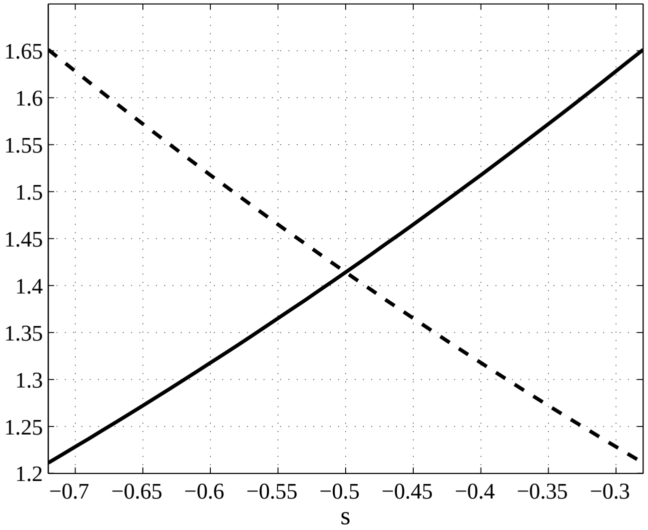

Figure 5.7: Plot of absolute values of amplitude ratios between w- and x-oscillators (with $\mu > 0$) for EQPT2 (solid curve) and EQPT3 (dashed curve) over parameter range (see Figure 5.6) where two stable phase-locked in-phase modes exist.

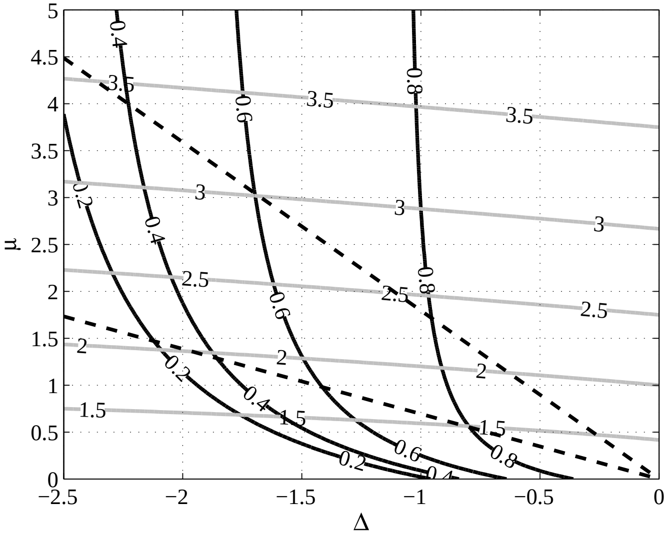

Figure 5.8: Plot of frequency contours for phase-locked in-phase modes associated with EQPT2 (ω_3, gray contours) and EQPT3 (ω_1, black contours) in Δ-μ parameter space. The dashed black line represents the boundary of the region of parameter space (see Figure 5.6) where two stable phase-locked in-phase modes exist.

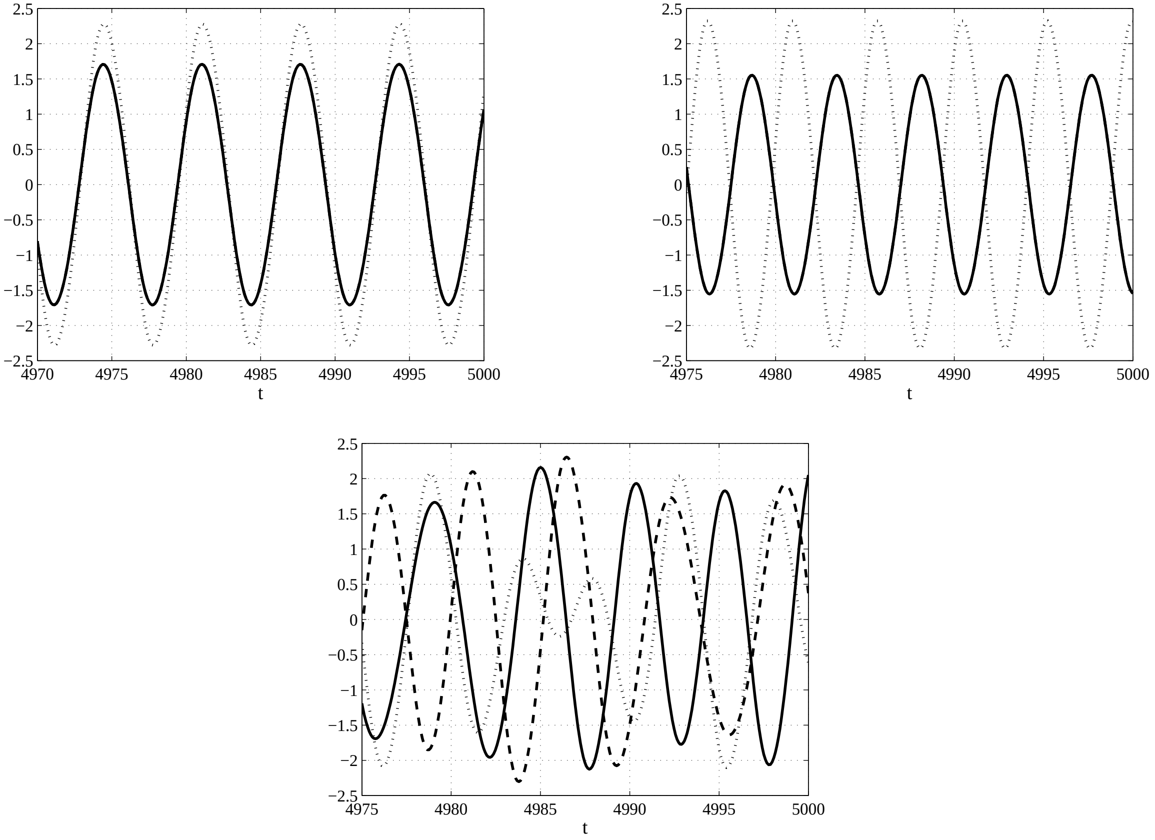

Figure 5.9: Numerical integrations (with $\epsilon = 0.1$) for the system (5.1) with parameter values $\Delta = -0.25$, $\mu = 0.3$ lying in Region IIIb3 of parameter space. $x(t)$ = solid line; $y(t)$ = dashed line; $w(t)$ = dotted line.

in-phase modes do exist in the same region of parameter space (see Figure 5.9).

An initial condition of $\begin{bmatrix} 0.1 & -0.1 & 0.15 & -0.15 & 0.1 & -0.05 \end{bmatrix}^T$ was used for the plot on the top-left, resulting in an in-phase motion that was both phase-locked and in-phase with the w-oscillator (i.e. EQPT3). For the top-right plot the initial condition was changed to $\begin{bmatrix} 0.1 & -0.1 & 0.15 & -0.15 & -0.1 & -0.05 \end{bmatrix}^T$. This initial condition resulted in an in-phase motion that was both phase-locked and out-of-phase with the w-oscillator (i.e. EQPT2). Table 5.4 compares the calculated versus predicted values for the frequencies of these motions. Our perturbation results agree quite well with the numerical integrations.

For the bottom plot an initial condition of $\begin{bmatrix} -0.1 & -0.1 & 0.15 & -0.15 & -0.1 & 0.05 \end{bmatrix}^T$ was used. However, instead of phase-locked in-phase motion, we find the system (5.1) exhibits stable quasi-periodic behavior not predicted by our perturbation analysis (see Table 5.2). We will discuss this plot more in the final section of this chapter.

Table 5.4: Calculated versus predicted frequencies for phase-locked in-phase modes in regions of Δ-μ parameter space where two such modes exist.

EQPT	Predicted $\omega(\frac{rad}{s})$	Calculated $\omega(\frac{rad}{s})$	%-Error
2	1.32288	1.32126	0.1
3	0.94868	0.94843	0.03

WEAK VS. STRONG COUPLING

There exists both qualitative and quantitative agreement between our perturbation results for the in-phase subspaces of the weakly and strongly coupled and detuned VDP systems. Recall from CHAPTER 2 that a Hopf bifurcation curve separates regions of parameter space where a stable quasi-periodic (or drift) motion exists from regions containing stable phase-locked behavior (see Figure 2.1 and Table 2.1 when moving between Regions I and IV). Furthermore, moving from Region IV into Region VI in Figure 2.1 sees the creation of an unstable LCD where there existed no LCD before. Compare this to moving from Region I to Region IIIa for the strongly-coupled system (see Figure 5.5 and Table 5.2). As we move from Region I to Region II a stable quasi-periodic motion (EQPT4) is destroyed while a phase-locked in-phase motion (EQPT2) becomes stable. Moving to Region III then brings the creation of a new unstable quasi-periodic motion (EQPT4 again).

We can quantitatively compare our results by first approximating the Hopf bifurcation curves (A.6) for the weakly-coupled system by their asymptotes. Keeping only the highest-order terms in (A.6) and solving for μ we get [19]

$$\begin{aligned}
\mu &= -\frac{2\left(7^{3/4}+\sqrt{59\sqrt{7}-119}-4\left(7^{1/4}\right)\right)}{9\left(7^{1/4}\right)}\delta \approx -0.531\delta \\
\mu &= \frac{2\left(-7^{3/4}+\sqrt{59\sqrt{7}-119}+4\left(7^{1/4}\right)\right)}{9\left(7^{1/4}\right)}\delta \approx 1.133\delta \\
\mu &= -\frac{2\left(-7^{3/4}+\sqrt{59\sqrt{7}+119}-4\left(7^{1/4}\right)\right)}{9\left(7^{1/4}\right)}\delta \approx -0.789\delta \\
\mu &= \frac{2\left(7^{3/4}+\sqrt{59\sqrt{7}+119}+4\left(7^{1/4}\right)\right)}{9\left(7^{1/4}\right)}\delta \approx 3.743\delta
\end{aligned} \tag{5.20}$$

For the strongly-coupled system's slow-flow (5.18) we look at the bifurcation curves separating Regions I and II, Regions IV and V, Regions II and IIIa, and Regions IIIc and IV, given by

$$\begin{aligned}
\mu &= \frac{1}{2}\left(-\frac{\sqrt{\sqrt{7}+5}}{2}-\frac{1}{2}\right)^{-1}\Delta \approx -0.266\Delta \\
\mu &= \frac{1}{2}\left(\frac{\sqrt{\sqrt{7}+5}}{2}-\frac{1}{2}\right)^{-1}\Delta \approx 0.567\Delta
\end{aligned} \tag{5.21}$$

$$\begin{aligned}\mu &= \frac{1}{2}\left(-\frac{\sqrt{-\sqrt{7}+5}}{2}-\frac{1}{2}\right)^{-1}\Delta \approx -0.395\Delta\\ \mu &= \frac{1}{2}\left(\frac{\sqrt{-\sqrt{7}+5}}{2}-\frac{1}{2}\right)^{-1}\Delta \approx 1.871\Delta\end{aligned}$$

respectively (see Figure 5.4 and Table 5.2).

Note that in Chapter 2 the square of the linear natural frequency for the w-oscillator is given as $1+2\epsilon\delta+O(\epsilon^2)$ while in this chapter we have used $1+\Delta$ instead. Substituting $\delta=\frac{\Delta}{2}$ into (5.20) results in the same equations as (5.21). Therefore the Hopf bifurcation curves from the weakly-coupled in-phase slow-flow (2.4) are asymptotic to the 4 bifurcation curves (5.21) (representing saddle-node or pitchfork bifurcations) from the slow-flow (5.18).

Internal Resonance

For certain values of the parameters Δ and μ the frequencies of the linear normal modes satisfy $a\omega_1+b\omega_2+c\omega_3=0$ for some integers a, b, and c. When this happens, new terms on the right-hand side of (5.13) become secular and must be removed to derive a valid slow-flow. On, and near, these parameter pairs our previously derived slow-flow (5.18) is not valid.

For the system (5.1) there exist 3 such resonances (to lowest order):

$$\begin{aligned}3\omega_1-\omega_3 &= 0 \qquad (5.22)\\ \omega_1-2\omega_2+\omega_3 &= 0\\ -\omega_1-2\omega_2+\omega_3 &= 0\end{aligned}$$

The first resonance occurs in the first mode where the terms $\cos(\omega_3\xi-2\omega_1\xi)$ and $\sin(\omega_3\xi-2\omega_1\xi)$ become secular and in the third mode where the terms $\cos(3\omega_1)$

and $\sin(3\omega_1)$ become secular. The second resonance is found in the second mode where the terms $\cos(\omega_3\xi - \omega_2\xi + \omega_1\xi)$ and $\sin(\omega_3\xi - \omega_2\xi + \omega_1\xi)$ become secular and in the third mode where the terms $\cos(2\omega_2\xi - \omega_1\xi)$ and $\sin(2\omega_2\xi - \omega_1\xi)$ become secular. Finally, the third resonance occurs in all three modes. In the first mode the terms $\cos(\omega_3\xi - 2\omega_2\xi)$ and $\sin(\omega_3\xi - 2\omega_2\xi)$ become secular, while in the second mode the terms $\cos(\omega_3\xi - \omega_2\xi - \omega_1\xi)$ and $\sin(\omega_3\xi - \omega_2\xi - \omega_1\xi)$ become secular, and in the third mode the terms $\cos(2\omega_2\xi + \omega_1\xi)$ and $\sin(2\omega_2\xi + \omega_1\xi)$ become secular.

In terms of the parameters Δ and μ the resonances satisfy

$$\begin{aligned} 81\mu^2 - (46\Delta + 192)\mu + 9\Delta^2 - 64\Delta - 64 &= 0 \qquad (5.23) \\ \mu^2 - (6\Delta + 8)\mu + \Delta^2 - 8\Delta &= 0 \qquad (5.24) \end{aligned}$$

where (5.23) corresponds to the resonant condition (5.22) and (5.24) corresponds to the other two resonances (see Figure 5.10). These last two resonances exist on separate branches of the curve and only coexist at a point of tangency, $(\Delta, \mu) = (8, 0)$, between (5.24) and the $\omega_1 = 0$ curve (5.12) where the condition $2\omega_1 + \omega_2 - \omega_3 = 0$ is satisfied.

The two resonance curves intersect at the points

$$\begin{aligned} (\Delta, \mu) &= \left(-\frac{4\sqrt{30} - 15}{17}, \frac{52 - 15\sqrt{30}}{17\sqrt{30} - 136} \right) \\ &\approx (0.7032, -0.40641) \\ (\Delta, \mu) &= \left(\frac{4\sqrt{30} + 15}{17}, -\frac{52 + 15\sqrt{30}}{17\sqrt{30} + 136} \right) \\ &\approx (-0.58556, 2.17111) \end{aligned}$$

where the condition $\omega_1 + \omega_2 - \omega_3 = 0$ is satisfied.

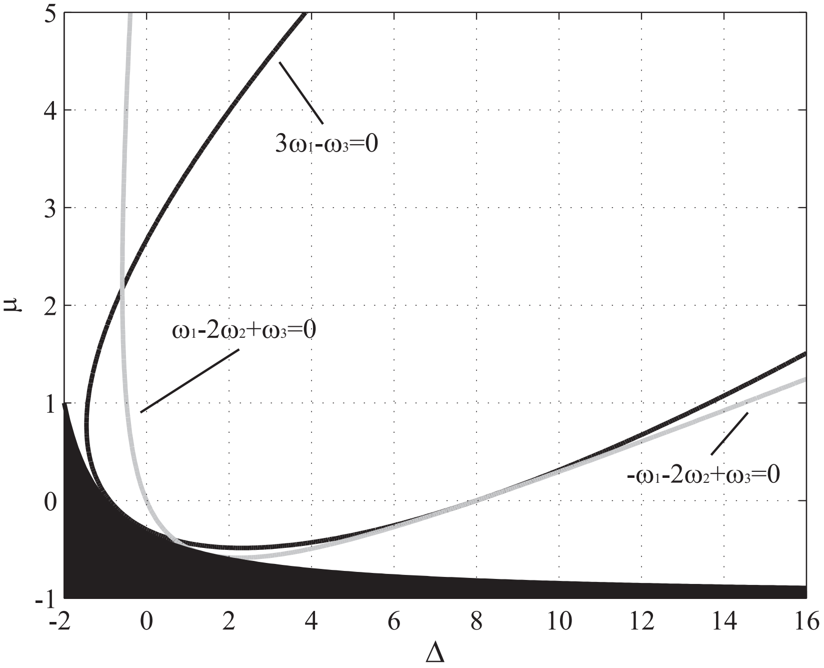

Figure 5.10: Resonance curves (5.23) (black line) and (5.24) (gray line) in Δ-μ parameter space. The black X represents the parameter pair chosen for numerical integrations in Figure 5.9. The black region represents parameter values where our analysis is not valid.

The black X in Figure 5.10 represents the parameter values chosen for the numerical integrations in Figure 5.9. We see that the values lie very close to the resonance curve (5.24). Therefore it is conceivable that the unexpected stable quasi-periodic behavior encountered in our numerical integrations is somehow related to the existence of this resonance. A new slow-flow valid near this resonance curve would need to be derived to further investigate the quasi-periodic motion's existence.

CHAPTER 6
TWO STRONGLY COUPLED VDP OSCILLATORS WITH 3:1 INTERNAL RESONANCE

At the conclusion of CHAPTER 5 we hypothesized that a numerical integration of (5.1) exhibiting an unpredicted stable quasi-periodic motion could possibly be explained by the existence of an internal resonance for the system. That is, the parameter values chosen for the numerical integration were such that the frequencies of the approximate normal modes (5.17) for (5.1) approximately satisfied $\omega_1 - 2\omega_2 + \omega_3 = 0$, one of three internal resonances (to lowest order) for (5.1).

In this chapter we make a mathematical aside from the biological modeling to study a lower-dimensional system ([23], [24]) similar to (5.1) for which there exists a single internal resonance. For this system we find that for parameter values approximately satisfying the resonance condition there exist periodic motions not predicted by a previous perturbation analysis ([23], [24]). These periodic motions are created and destroyed in phase space mainly through the bifurcation of a torus (i.e. a quasi-periodic motion) into two periodic motions. We apply the two-variable expansion perturbation method to this system to derive a new slow-flow that is valid for parameters near where the resonance condition is satisfied. Then using regular perturbation methods we determine the boundary for the region of parameter space where these previously unpredicted periodic motions exist and check our results using numerical methods.

The system under study consists of two strongly coupled and detuned weakly-nonlinear ($\epsilon \ll 1$) VDP oscillators x and w and is given by

$$\begin{aligned} \ddot{x} - \epsilon(1 - x^2)\dot{x} + x &= \mu(w - x) \\ \ddot{w} - \epsilon(1 - w^2)\dot{w} + (1 + \Delta)w &= \mu(x - w) \end{aligned} \tag{6.1}$$

The x-oscillator has an uncoupled frequency of unity while that of the w-oscillator is detuned via the parameter Δ. The coupling between the oscillators is linear in the displacements with coupling parameter μ. The coupling and detuning are considered “strong” as the parameters μ and Δ are $O(1)$.

The system (6.1) was originally studied by Storti & Rand ([23], [24]) and we summarize their results before investigating the existence of the internal resonance for the system.

<u>SUMMARY OF STORTI & RAND’S WORK</u>

Preparation of the system (6.1) for application of the two-variable expansion singular perturbation method follows closely the procedure described in CHAPTER 5 for the system of three strongly coupled and detuned VDP oscillators. However, we now follow Storti & Rand ([23], [24]) by defining the $\epsilon = 0$ linear normal mode coordinates for (6.1) via the orthonormal linear transformation

$$\underline{\mathbf{u}} = [S]\,\underline{\mathbf{v}} = \begin{bmatrix} \alpha & \beta \\ -\beta & \alpha \end{bmatrix} \underline{\mathbf{v}} \tag{6.2}$$

where $\underline{\mathbf{v}} = \begin{bmatrix} v_1(t) & v_2(t) \end{bmatrix}^T$. To determine α and β we require

$$\begin{bmatrix} 1+\mu & -\mu \\ -\mu & \mu+1+\Delta \end{bmatrix} \begin{bmatrix} \alpha \\ -\beta \end{bmatrix} = \lambda_1 \begin{bmatrix} \alpha \\ -\beta \end{bmatrix} \tag{6.3}$$

and the condition $\alpha^2 + \beta^2 = 1$ to be satisfied, where

$$\begin{aligned} \lambda_1 &= 1 + \mu \left(1 + s - \sqrt{1 + s^2}\right) \\ \lambda_2 &= 1 + \mu \left(1 + s + \sqrt{1 + s^2}\right) \end{aligned} \tag{6.4}$$

are the eigenvalues of the matrix in (6.3) and the parameter s is defined by (5.4). Solving this system of three equations yields

$$\begin{aligned} \alpha^2 &= \frac{1 + s^2 + s\sqrt{1 + s^2}}{2 + 2s^2} \\ \beta^2 &= \frac{1 + s^2 - s\sqrt{1 + s^2}}{2 + 2s^2} \end{aligned}$$

Note that these are different definitions than used in the original work ([23], [24]) where we believe there was a mix-up between eigenvectors and their associated eigenvalues (see Figure 6.1 for a comparison between the two sets of definitions). Fortunately, the error does appear to affect any results. Also, we must be mindful to distinguish between positive and negative μ. For $\mu > 0$ we find $\alpha = +\sqrt{\alpha^2}$ and $\beta = -\sqrt{\beta^2}$ while for $\mu < 0$ we find $\alpha = -\sqrt{\beta^2}$ and $\beta = -\sqrt{\alpha^2}$.

Applying the two-variable expansion perturbation method to the transformed system results in lowest-order solutions of the form

$$v_{i0}(t) = R_i(\epsilon t) \cos\left(\omega_i t - \phi_i\right) \tag{6.5}$$

where $\omega_i = \sqrt{\lambda_i}$ $(i = 1, 2)$ and the amplitudes R_i are functionally dependent on slow-time ϵt. Therefore we find that the lowest-order approximate normal modes contain no frequency-amplitude dependence and to $O(\epsilon)$ oscillate on the normal time-scale with constant phase. This is similar to our result in CHAPTER 5 for three strongly coupled VDP oscillators.

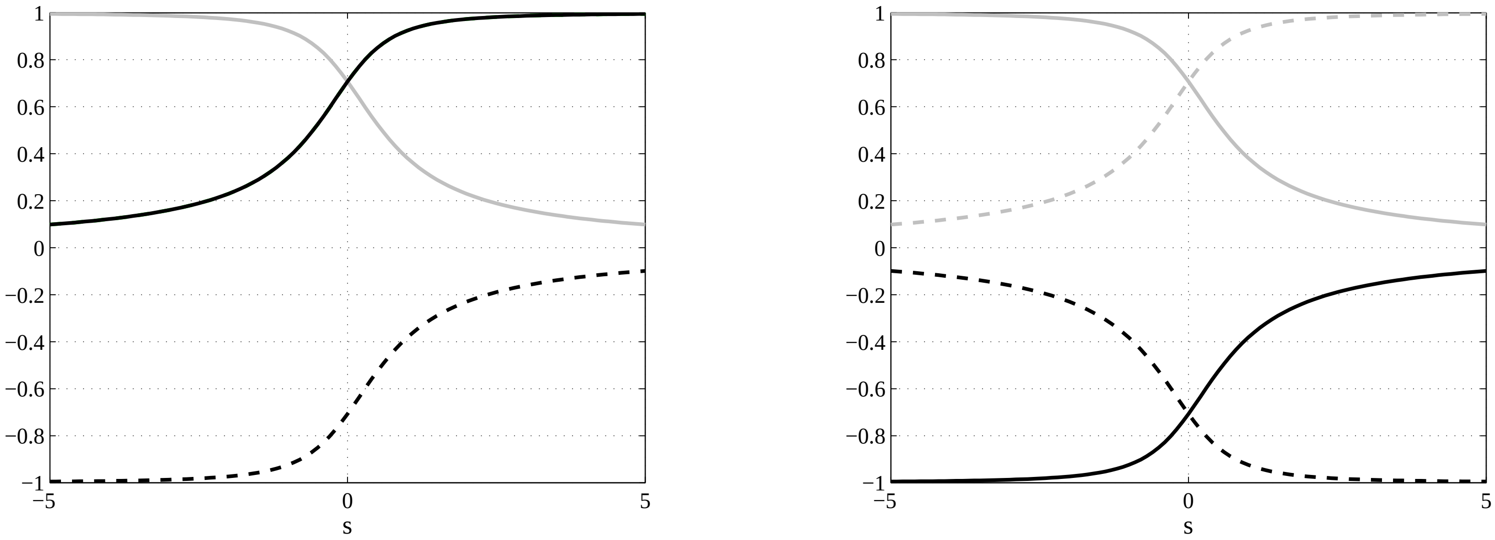

Figure 6.1: Comparison between definitions of α and β (black curves, solid and dashed respectively) with a and b (gray curves, solid and dashed respectively) from ([23],[24]) for $\mu > 0$ (left) and $\mu < 0$ (right). Note that there is partial agreement between the definitions ($\alpha = b$) when $\mu > 0$.

For the perturbation method to work we require the lowest-order solutions (6.5) to remain oscillatory. That is, we require $\omega_i > 0$, and hence $\lambda_i > 0$ $(i = 1, 2)$. Substituting $s = \frac{\Delta}{2\mu}$ into (6.4) and performing some algebraic manipulation yields the equation (see Figure 6.2)

$$\mu = -\frac{\Delta + 1}{\Delta + 2} \tag{6.6}$$

which restricts the region of Δ-μ parameter space where our analysis is valid.

The amplitudes of the lowest-order solutions vary with respect to slow-time according to the 2-dimensional slow-flow ([23],[24])

$$\begin{aligned} \frac{dR_1}{d\eta} &= \frac{R_1}{2}\left[1 - AR_2^2 - CR_1^2\right] \\ \frac{dR_2}{d\eta} &= \frac{R_2}{2}\left[1 - AR_1^2 - CR_2^2\right] \end{aligned} \tag{6.7}$$

where $A = \alpha^2\beta^2$ and $C = \frac{1}{4}(\beta^4 + \alpha^4)$.

The form of the slow-flow (6.7) allows us to easily solve for equilibrium points in closed-form by setting the right-hand side of (6.7) equal to zero and solving for R_1^* and R_2^* (see Table 6.1).

Transforming back into the original coordinate system using (6.2) we have

$$\begin{aligned} x(t) &= \alpha v_1 + \beta v_2 \\ &= \alpha R_1(\epsilon t)\cos(\omega_1 t - \phi_1) + \beta R_2(\epsilon t)\cos(\omega_2 t - \phi_2) \\ w(t) &= -\beta v_1 + \alpha v_2 \\ &= -\beta R_1(\epsilon t)\cos(\omega_1 t - \phi_1) + \alpha R_2(\epsilon t)\cos(\omega_2 t - \phi_2) \end{aligned}$$

Phase-locked motions for (6.1) will consist of motions comprised of only a single mode, i.e. motions corresponding to slow-flow equilibrium points with 1 coordinate

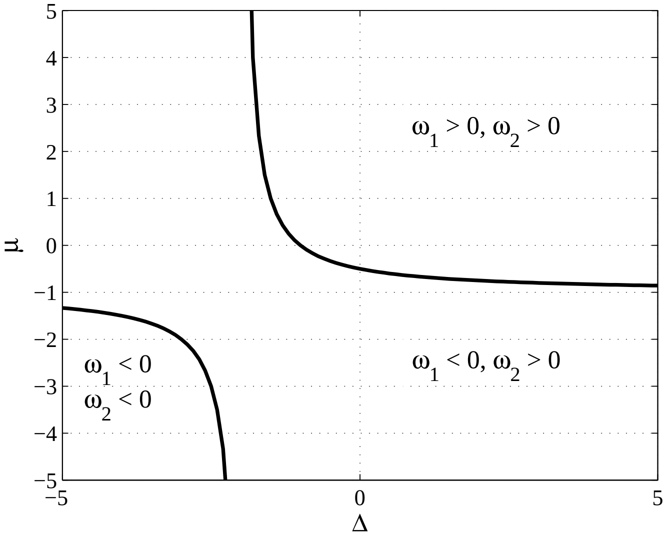

Figure 6.2: For the lowest-order solutions (6.5) to remain oscillatory we require $\omega_i > 0$ $(i = 1, 2)$. This restricts the validity of our analysis to a region of Δ-μ parameter space bounded by the curve (6.6) (black curve).

set equal to zero. From Table 6.1 we see that EQPT2 and EQPT3 correspond to phase-locked motions. Moreover, because the coefficients α and β in (6.8) have opposite signs (see Figure 6.1) we conclude that EQPT2 corresponds to an out-of-phase (in-phase) phase-locked motion for $\mu > 0$ $(\mu < 0)$ while EQPT3 corresponds to an in-phase (out-of-phase) phase-locked motion for $\mu > 0$ $(\mu < 0)$. EQPT4 will in general represent quasi-periodic behavior as it is comprised of two modes with non-commensurable frequencies. Table 6.2 summarizes the dynamical behavior for (6.1) that each slow-flow equilibrium point corresponds to.

We now investigate the 2-dimensional slow-flow phase space using the PPLANE ODE software for MATLAB [15]. We start with $s^2 = \frac{1}{4}$ (see Figure 6.3) where we find that all solution trajectories for (6.7) approach an equilibrium point on either the R_1 (EQPT3) or R_2 (EQPT2) axes while EQPT4 is a saddle. Increasing the parameter to $s^2 = \frac{1}{2}$ creates a structurally-unstable line of non-isolated equilibrium points connecting EQPT2 and EQPT3 (see Figure 6.4). Substituting $s^2 = \frac{1}{2}$ into

Table 6.1: The 9 equilibrium points of the slow-flow (6.7) ([23],[24]).

EQPT	(R_1^*, R_2^*)
1	$(0, 0)$
2	$\left(0, \pm\sqrt{\frac{1}{C}}\right)$
3	$\left(\pm\sqrt{\frac{1}{C}}, 0\right)$
4	$\left(\pm\sqrt{\frac{1}{A+C}}, \pm\sqrt{\frac{1}{A+C}}\right)$

Table 6.2: Descriptions of the dynamical behavior in (6.1) that each equilibrium point of the slow-flow (6.7) corresponds to for $\mu > 0$.

EQPT	Description of Dynamical Behavior
1	trivial solution
2	x- and w-oscillators out-of-phase
3	x- and w-oscillators in-phase
4	quasi-periodic behavior

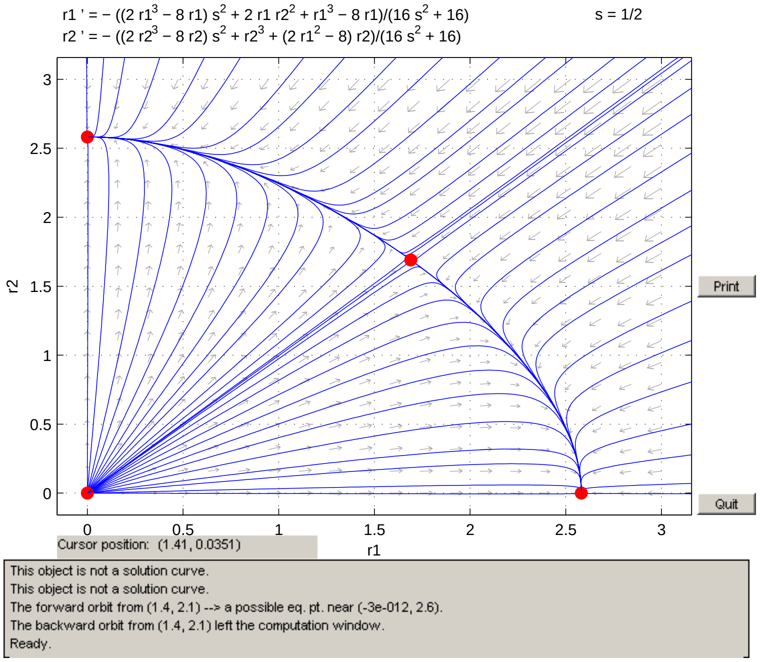
$r1' = -((2\,r1^3 - 8\,r1)\,s^2 + 2\,r1\,r2^2 + r1^3 - 8\,r1)/(16\,s^2 + 16)$ s = 1/2

$r2' = -((2\,r2^3 - 8\,r2)\,s^2 + r2^3 + (2\,r1^2 - 8)\,r2)/(16\,s^2 + 16)$

Cursor position: (1.41, 0.0351)

This object is not a solution curve.
This object is not a solution curve.
The forward orbit from (1.4, 2.1) --> a possible eq. pt. near (-3e-012, 2.6).
The backward orbit from (1.4, 2.1) left the computation window.
Ready.

Figure 6.3: Phase portrait for the slow-flow (6.7) with $s^2 = \frac{1}{4}$. EQPT2 and EQPT3 are stable while EQPT4 is a saddle.

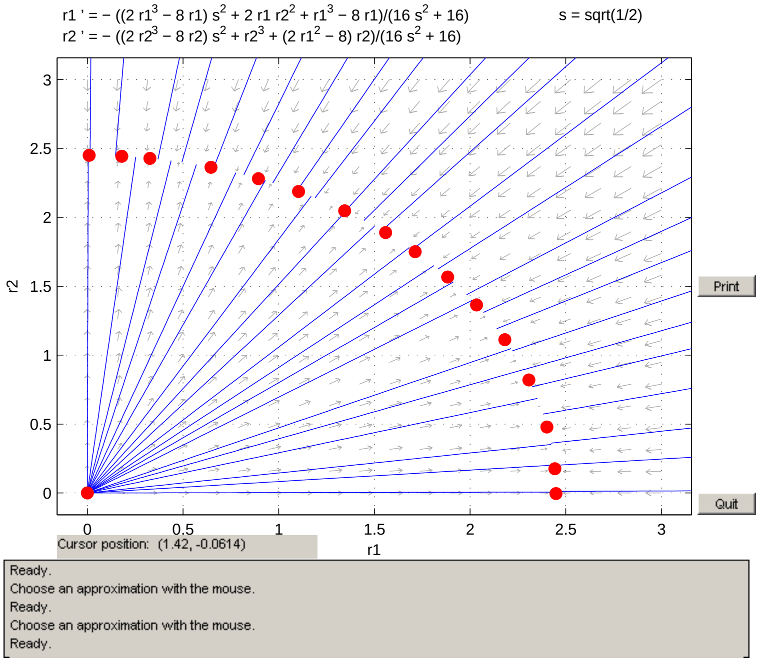
$r1' = -((2\,r1^3 - 8\,r1)\,s^2 + 2\,r1\,r2^2 + r1^3 - 8\,r1)/(16\,s^2 + 16)$ s = sqrt(1/2)

$r2' = -((2\,r2^3 - 8\,r2)\,s^2 + r2^3 + (2\,r1^2 - 8)\,r2)/(16\,s^2 + 16)$

Cursor position: (1.42, -0.0614)

Ready.
Choose an approximation with the mouse.
Ready.
Choose an approximation with the mouse.
Ready.

Figure 6.4: Phase portrait for the slow-flow (6.7) with $s^2 = \frac{1}{2}$. There exists a line of non-isolated equilibrium points connecting EQPT2 and EQPT3 and satisfying $R_1^{*2} + R_2^{*2} = 6$.

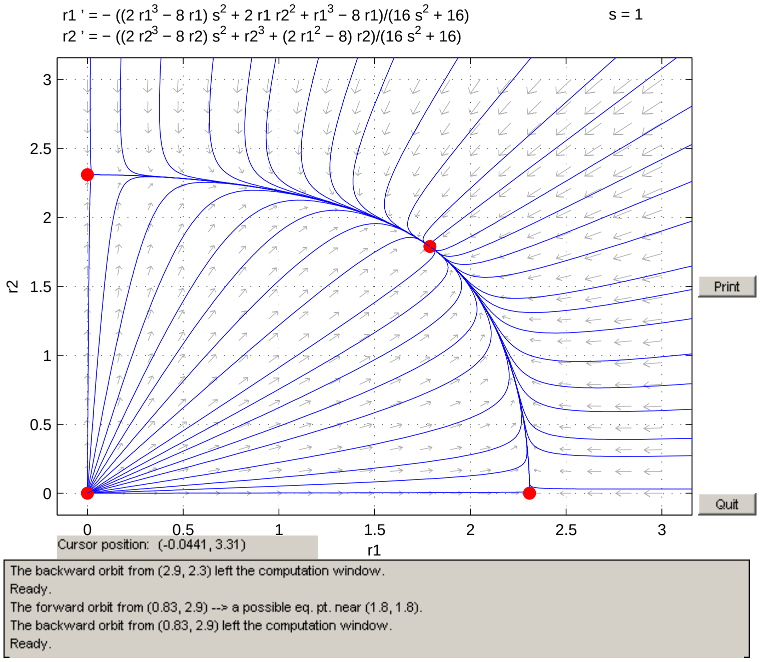
r1 ' = − ((2 r1^3 − 8 r1) s^2 + 2 r1 r2^2 + r1^3 − 8 r1)/(16 s^2 + 16)
r2 ' = − ((2 r2^3 − 8 r2) s^2 + r2^3 + (2 r1^2 − 8) r2)/(16 s^2 + 16)

s = 1

Cursor position: (-0.0441, 3.31)

The backward orbit from (2.9, 2.3) left the computation window.
Ready.
The forward orbit from (0.83, 2.9) --> a possible eq. pt. near (1.8, 1.8).
The backward orbit from (0.83, 2.9) left the computation window.
Ready.

Figure 6.5: Phase portrait for the slow-flow (6.7) with $s^2 = 1$. The stabilities of the equilibrium points have now flipped. EQPT4 is a global sink while EQPT2 and EQPT3 are saddles.

(6.7) we find this curve of equilibrium points satisfies the equation $R_1^{*2} + R_2^{*2} = 6$ ([23],[24]). If we continue to increase the parameter to $s^2 = 1$ we find that the stabilities of the equilibrium points have flipped and now EQPT4 is a global sink while EQPT2 and EQPT3 are saddles (see Figure 6.5). For all parameter values the origin is unstable.

Linearizing the slow-flow (6.7) about each equilibrium point confirms these qualitative results ([23],[24]). Therefore we conclude that $s^2 = \frac{1}{2}$ is a critical bifurcation value. When $s^2 < \frac{1}{2}$ the system exhibits stable phase-locked in-phase or out-of-phase motion while for $s^2 > \frac{1}{2}$ there exists stable quasi-periodic motion ([23],[24]) (see Figure 6.6 for numerical examples). Using (5.4) the critical bifurcation value $s^2 = \frac{1}{2}$ yields two bifurcation curves in Δ-μ parameter space (see Figure 6.7) given by

$$\mu = \pm \frac{\sqrt{2}}{2} \Delta \tag{6.8}$$

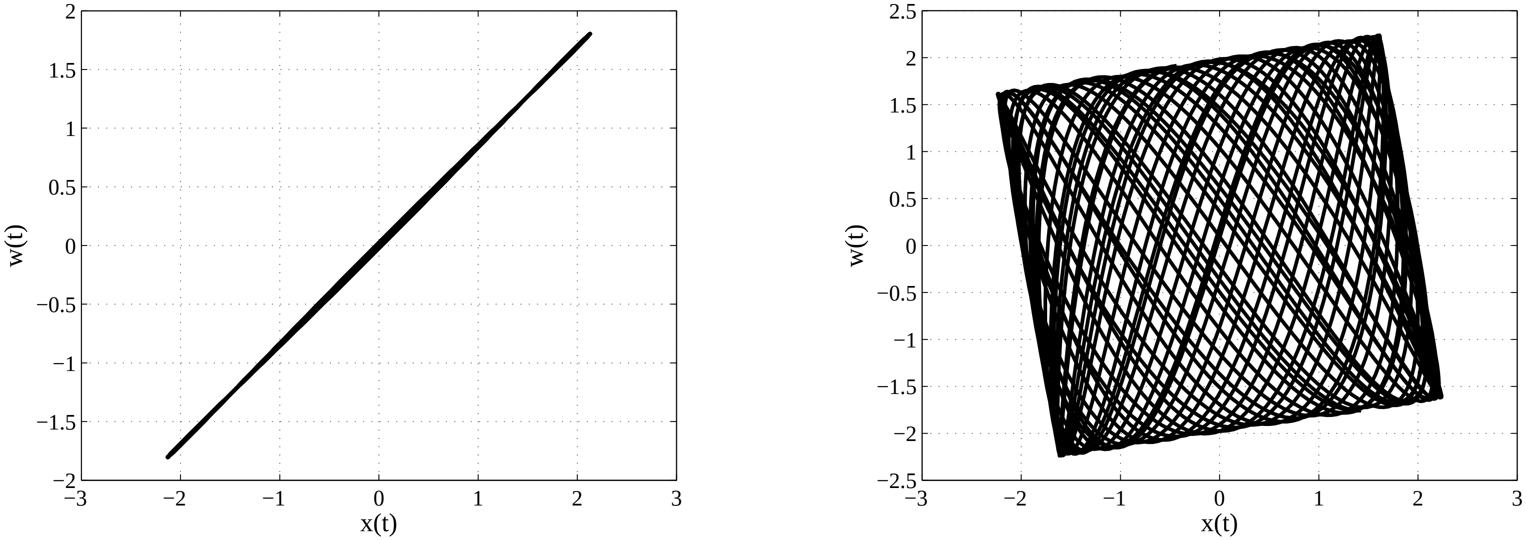

Figure 6.6: Examples of dynamical behavior found in the system (6.1) – phase-locked in-phase motion (left) and quasi-periodic motion (right). Numerical integrations were performed with random initial conditions and parameter values $\Delta = 1$, $\mu = 3$ ($s^2 = \frac{1}{36}$) and $\Delta = 6$, $\mu = 1$ ($s^2 = 9$) respectively and plotted in $x(t)$-$w(t)$ configuration space.

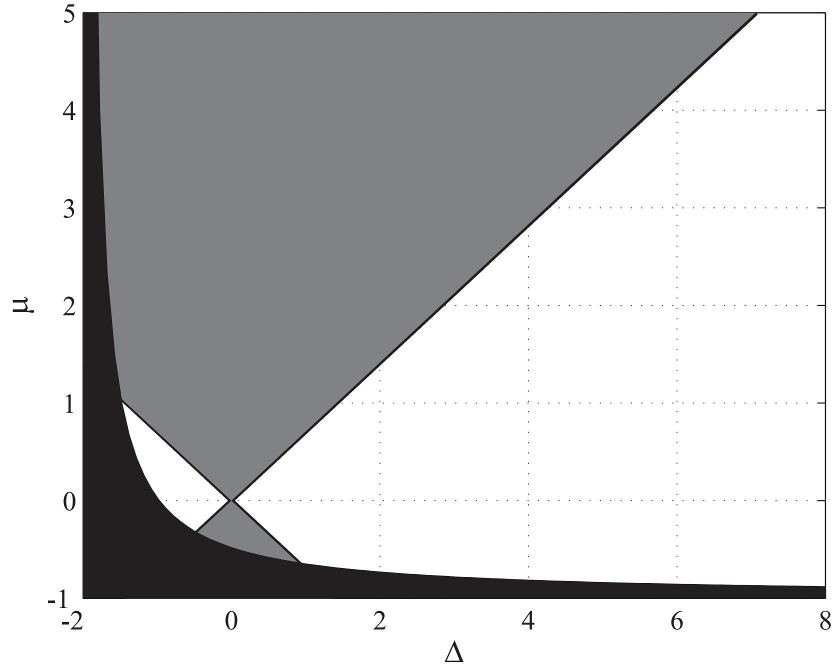

Figure 6.7: Bifurcation curves (6.8) for the slow-flow (6.7). The gray region represents parameter values where there exist stable phase-locked in-phase and out-of-phase motions for (6.1), while the black region represents parameter values where our analysis is not valid due to the lowest order solutions (6.5) becoming non-oscillatory.

INVESTIGATION OF 3:1 RESONANCE

For certain parameter values the linear normal mode frequencies satisfy $3\omega_1 - \omega_2 = 0$. This causes new terms to become secular during application of the two-variable expansion perturbation method thereby requiring the derivation of a new slow-flow for these parameters [23]. When applying the perturbation method to (6.1) terms of the form $\cos(2\omega_1\xi - \omega_2\xi)$ and $\sin(2\omega_1\xi - \omega_2\xi)$ now become secular for the first mode and $\cos(3\omega_1\xi)$ and $\sin(3\omega_1\xi)$ become secular for the second mode [23].

To locate where in parameter space the condition $3\omega_1 - \omega_2 = 0$ holds we substitute into this $\omega_i = \sqrt{\lambda_i}$ where λ_i $(i = 1, 2)$ is defined by (6.4). After some algebraic manipulation this results in a curve in parameter space along which the 3:1 resonance condition is satisfied (see Figure 6.8) and is given by

$$36\mu^2 - 64\Delta\mu - 128\mu + 9\Delta^2 - 64\Delta - 64 = 0 \tag{6.9}$$

To illustrate the impact the 3:1 resonance has on the expected dynamical behavior for the system (6.1) we look at regions of parameter space where the slow-flow (6.7) predicts stable quasi-periodic behavior (i.e. $s^2 > \frac{1}{2}$). For any pair of parameter values in this region all solution trajectories are expected to approach a stable torus residing in the 4-dimensional phase space of (6.1) (see the right graph in Figure 6.6). However, for parameter values satisfying (6.9) the stable torus has been replaced by a periodic motion (see Figure 6.9).

We now derive a new slow-flow that will be valid on and *near* the 3:1 resonance curve (6.9) by substituting $\omega_2 = 3\omega_1 + \epsilon\gamma$ before the removal of secular terms in the two-variable expansion method [14]. The new parameter γ allows us to detune slightly off the true resonance and is taken to be $O(\epsilon)$. After this substitution is

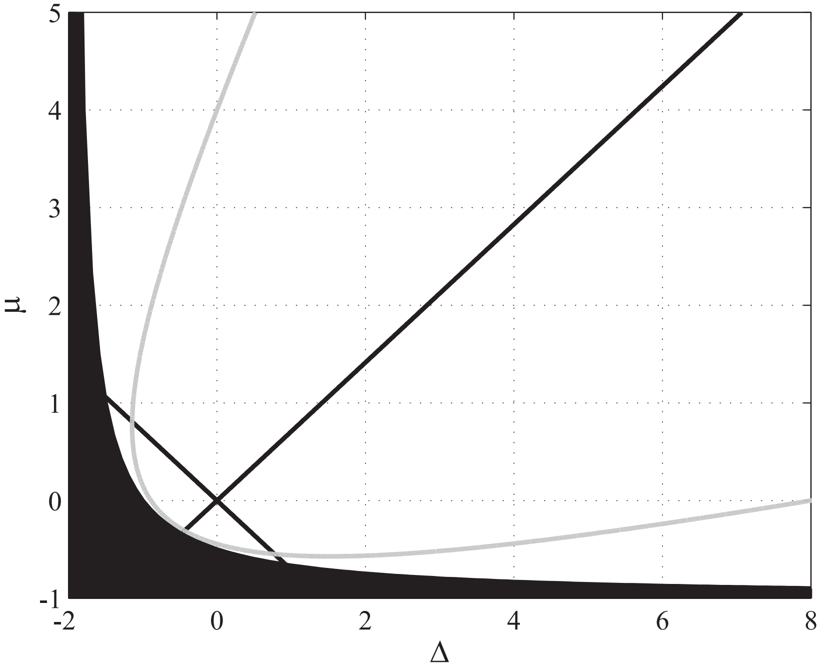

Figure 6.8: Plot of the 3:1-resonance curve (6.9) (gray curve) with bifurcation curves (6.8) for the slow-flow (6.7). The black region represents parameter values where our analysis is not valid due to the lowest order solutions (6.5) becoming non-oscillatory.

made the new lowest-order solutions are

$$\begin{aligned} v_{10}(\eta,\xi) &= R_1(\eta)\cos\left(\omega_1\xi - \theta_1(\eta)\right) \\ v_{20}(\eta,\xi) &= R_2(\eta)\cos\left(3\omega_1\xi - \theta_2(\eta)\right) \end{aligned} \tag{6.10}$$

Substituting these equations into the new $O(\epsilon)$ equations and eliminating secular terms yields a new 4-dimensional slow-flow. Unfortunately we can no longer eliminate both slow-flow phase equations by directly integrating them as was possible for the original slow-flow (6.7). Instead, we reduce the dimension by 1 by defining a new phase-difference variable $\Phi = \theta_2 - 3\theta_1$ giving us the 3-dimensional 3:1

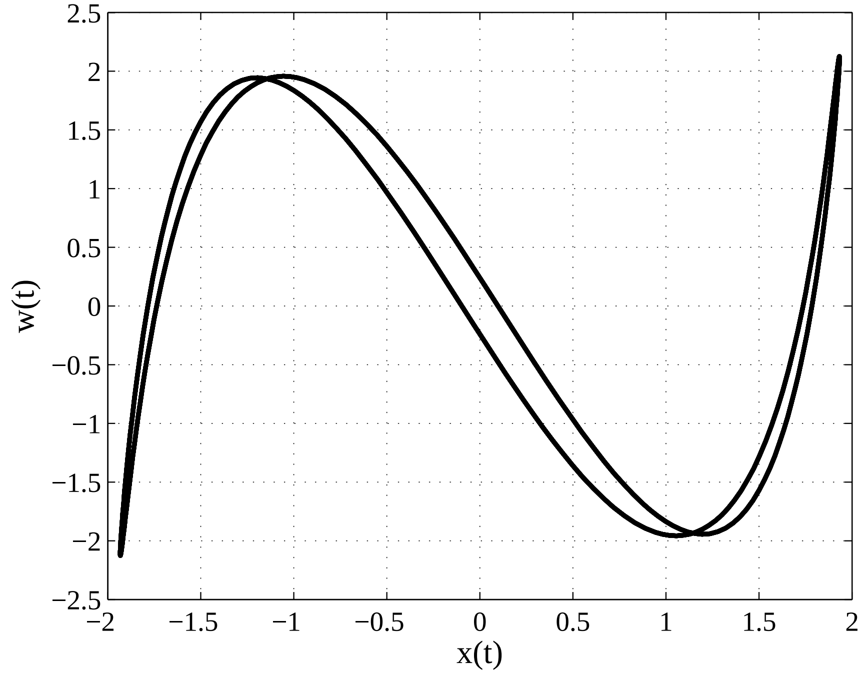

Figure 6.9: Numerical integration of (6.1) performed with random initial conditions and parameter values $\Delta = 14$, $\mu \approx 0.8081$ ($s^2 \approx 8.6623$) satisfying (6.9) and exhibiting stable 3:1-periodic motion. Plotted in $x(t)$-$w(t)$ configuration space.

resonance slow-flow

$$\begin{aligned}
\frac{dR_1}{d\eta} &= \frac{R_1}{2}\left[1 - AR_2^2 - CR_1^2\right] - 3BR_1^2R_2\cos\Phi \\
\frac{dR_2}{d\eta} &= \frac{R_2}{2}\left[1 - AR_1^2 - CR_2^2\right] - BR_1^3\cos\Phi \\
\frac{d\Phi}{d\eta} &= B\frac{R_1}{R_2}(9R_2^2 + R_1^2)\sin\Phi - \gamma
\end{aligned} \tag{6.11}$$

where $B = \frac{1}{24}\alpha\beta(\alpha^2 - \beta^2)$, and $A = \alpha^2\beta^2$ and $C = \frac{1}{4}(\beta^4 + \alpha^4)$ are as previously defined.

We now investigate the 3-dimensional phase space of the 3:1 resonance slow-flow (6.11) using the MATDS software for MATLAB [7]. We select parameter values $(s, \gamma) = (-2.5, 0.4)$ living in a region of parameter space (see Figure 6.7) where the

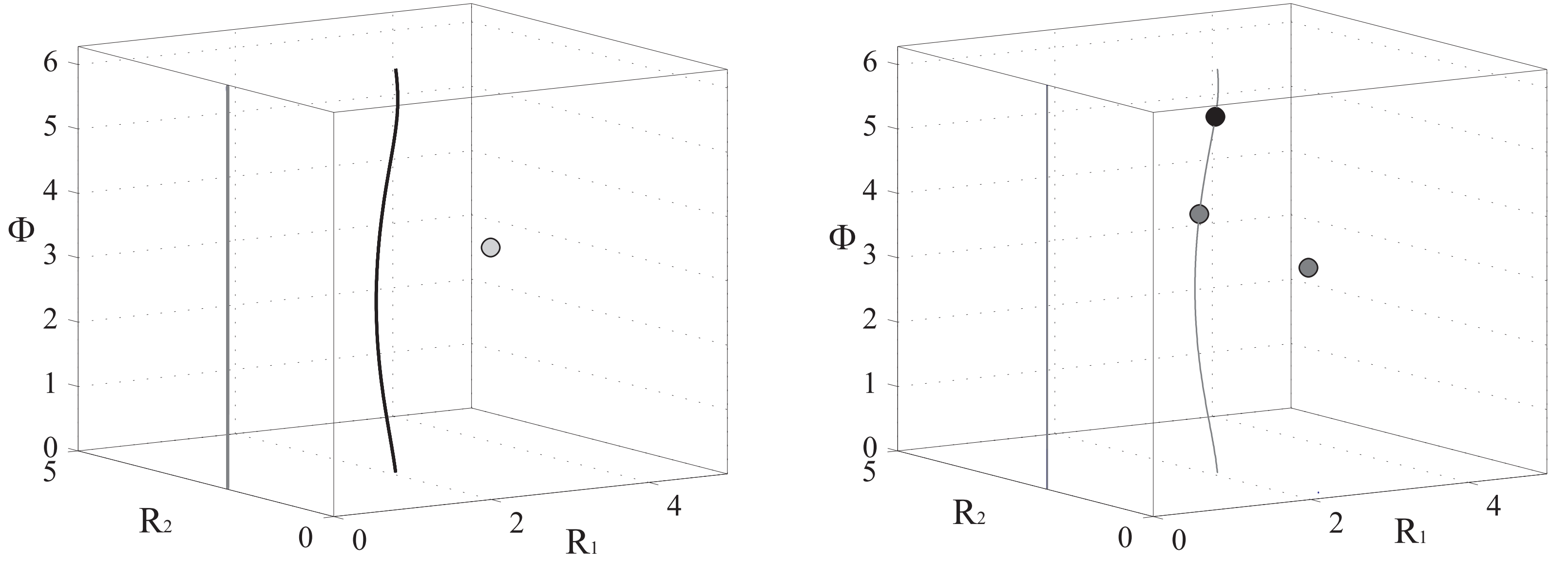

Figure 6.10: 3-dimensional phase space for the 3:1 resonance slow-flow (6.11) with $s = -2.5$ (i.e. $s^2 = 6.25$), $\gamma = 0.4$ (left) and $\gamma = 0.2$ (right). The left plot shows that when the detuning from the resonance curve (6.9) is significantly large ($\gamma = 0.4$) the phase space is dominated by three dynamical features – an unstable LCD (gray line) living in the invariant $R_1 = 0$ plane, an unstable equilibrium point (gray circle) lying near, but not on, the singular $R_2 = 0$ plane, and a stable LCD (black curve). As we decrease the detuning to $\gamma = 0.2$ (right plot) an infinite-period bifurcation occurs along the stable LCD resulting in the creation of one new stable (black circle) and one new unstable equilibrium point.

original slow-flow (6.7) predicts the existence of stable quasi-periodic behavior for (6.1). We find that the phase space is dominated by three dynamical features – an unstable LCD (i.e. a limit cycle that is cyclic in Φ) living in the invariant $R_1 = 0$ plane, an unstable equilibrium point near, but not on, the singular $R_2 = 0$ plane, and a stable LCD (see Figure 6.10). We identify the stable LCD with EQPT4 for the original slow-flow (6.7). That is, the stable quasi-periodic motion predicted by (6.7) now appears as a stable LCD for the 3:1 resonance slow-flow (6.11). Likewise, we identify the unstable LCD with EQPT2 for (6.7). While it is tempting to then identify the unstable equilibrium point with EQPT3 we cannot because EQPT3 lives in the $R_2 = 0$ plane which is now singular. That is, the approximate normal mode defined by (6.10) ceases to exist near the 3:1 resonance (see [10] for discussion of a similar result for a system of coupled oscillators with cubic nonlinearity).

Instead, the unstable equilibrium point corresponds a 3:1 periodic motion for the original system (6.1) since

$$\frac{d\Phi}{d\eta} = 0 \Rightarrow \Phi(\eta) = \theta_2(\eta) - 3\theta_1(\eta) = k$$

where k is the constant of integration. Plugging this back into (6.10) yields

$$\begin{aligned} v_{10}(\eta, \xi) &= R_1(\eta)\cos Z(t) \\ v_{20}(\eta, \xi) &= R_2(\eta)\cos\left(3Z(t) - k\right) \end{aligned}$$

where $Z(t) = \omega_1\xi - \theta_1(\eta)$. Therefore a motion comprised of both modes will now be periodic with a period equal to 2π.

As we decrease the detuning parameter to $\gamma = 0.2$ the flow along the stable LCD slows down until an infinite-period bifurcation occurs. Afterwards we are left with 3 equilibrium points, 1 of which is now stable, and the unstable LCD in the $R_1 = 0$ plane. This stable equilibrium point represents a stable 3:1-periodic motion for (6.1) where the original slow-flow (6.7) predicted only quasi-periodic behavior.

Further numerical investigation indicates that this infinite-period bifurcation along the stable LCD is the primary way in which a stable 3:1-periodic motion for (6.1) is created from a stable quasi-periodic motion.

Next we select parameter values $(s, \gamma) = (-.5, 0.2)$ from a region of parameter space where the original slow-flow (6.7) predicts the existence of stable phase-locked behavior and unstable quasi-periodic behavior. We find that two equilibrium points are once again born in an infinite-period bifurcation along the LCD we have identified with a quasi-periodic motion for (6.1), but because this quasi-periodic motion was unstable this bifurcation now results in two unstable 3:1-periodic motions (see Figure 6.11). There also exists a stable LCD living in the invariant $R_1 = 0$ plane and a stable equilibrium point near the singular $R_2 = 0$ surface. The former is once again identified with EQPT2 indicating that there exits a stable 1:1 out-of-phase periodic motion even in the presence of the 3:1 resonance. The latter equilibrium point represents a stable 3:1-periodic motion for (6.1) where the x- and w-oscillators are nearly in-phase with each other.

A SECOND PERTURBATION

We now attempt to determine the boundary for the region of Δ-μ parameter space about the 3:1 resonance curve (6.9) where the previously unpredicted periodic motions exist. This boundary will correspond to an infinite-period bifurcation occurring along a stable LCD for the 3:1 resonance slow-flow (6.11). We proceed by modifying the 3:1 slow-flow equations (6.11) by considering the terms B and γ

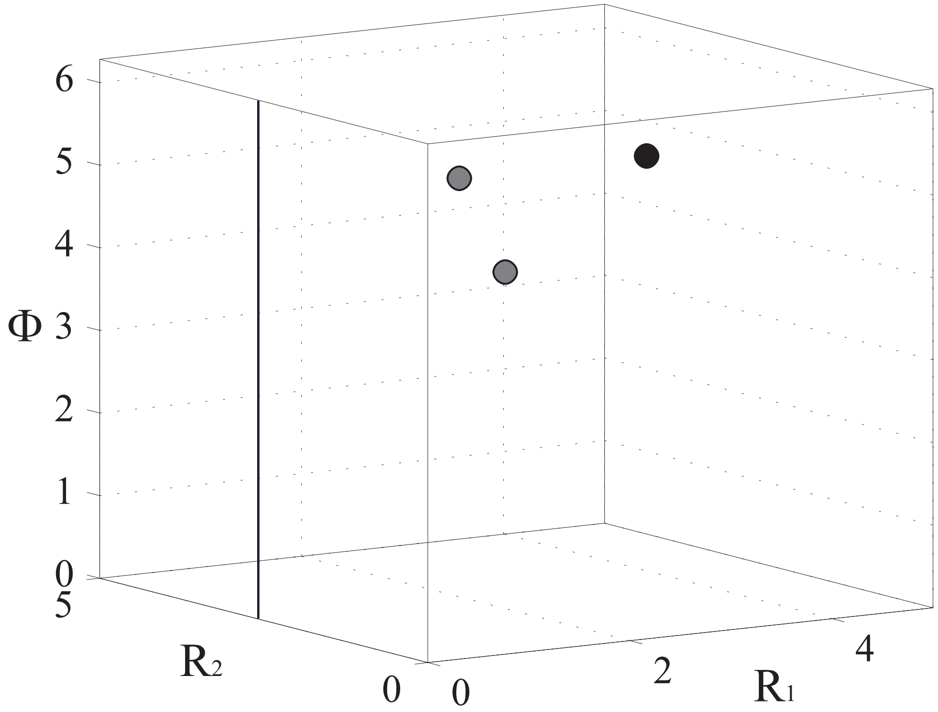

Figure 6.11: 3-dimensional phase space for the 3:1 resonance slow-flow (6.11) with $s = -0.5$ (i.e. $s^2 = -0.25$), $\gamma = 0.2$. The plot shows that when the detuning from the resonance curve (6.9) is small ($\gamma = 0.2$) the phase space exhibits three equilibrium points, one of which is stable (black circle), and a stable LCD (black line) living in the invariant $R_1 = 0$ plane. The two unstable equilibrium points are born in an infinite-period bifurcation occurring along an unstable LCD.

to be $O(\tilde{\epsilon})$ where $\tilde{\epsilon} \ll 1$. This new slow-flow is given by

$$\begin{aligned}
\frac{dR_1}{d\eta} &= \frac{R_1}{2}\left[1 - AR_2^2 - CR_1^2\right] - \tilde{\epsilon}3BR_1^2R_2\cos\Phi \\
\frac{dR_2}{d\eta} &= \frac{R_2}{2}\left[1 - AR_1^2 - CR_2^2\right] - \tilde{\epsilon}BR_1^3\cos\Phi \\
\frac{d\Phi}{d\eta} &= \tilde{\epsilon}\left[B\frac{R_1}{R_2}(9R_2^2 + R_1^2)\sin\Phi - \gamma\right]
\end{aligned} \tag{6.12}$$

It is natural to assume γ to be small as it is a detuning parameter. Our motivation for assuming B to be small is two-fold. With B and γ both small, the lowest order $\tilde{\epsilon} = 0$ slow-flow is simply the original slow-flow (6.7). That is, the new slow-flow

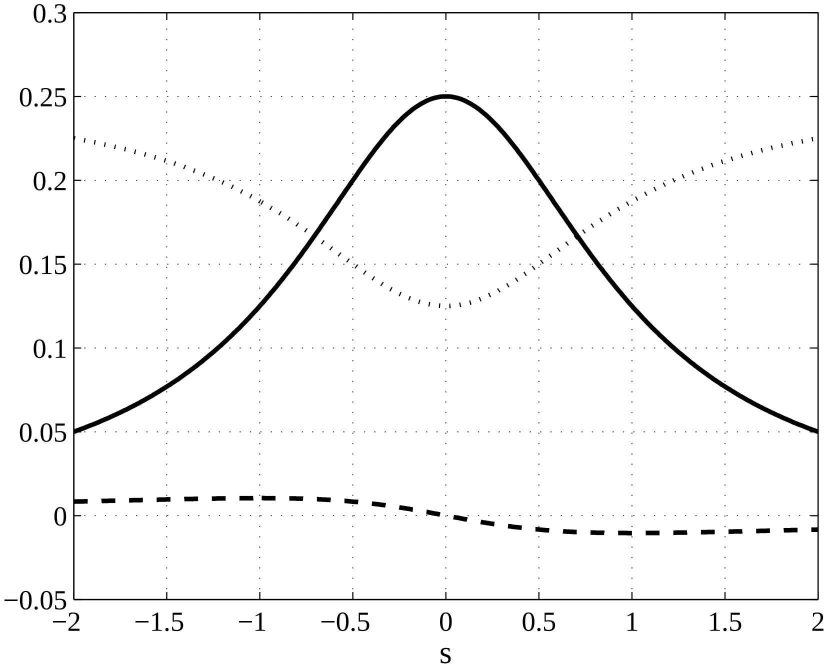

Figure 6.12: Plot of slow-flow coefficients versus the parameter s. A = solid line; B = dashed line; C = dotted line.

(6.12) can be considered a perturbation to the original slow-flow (6.7). A numerical justification is that the maximum value of $|B|$ as a function of s is only $\frac{1}{96}$ (see Figure 6.12).

We now investigate the new slow-flow (6.12) via regular perturbation. We expand the variables $R_i = R_{i0} + \tilde{\epsilon} R_{i1} + O(\tilde{\epsilon}^2)$ $(i = 1, 2)$ and $\Phi = \Phi_0 + \tilde{\epsilon}\Phi_1 + O(\tilde{\epsilon}^2)$ and substitute them into (6.12). After Taylor-expanding the equations in terms of $\tilde{\epsilon}$, the lowest order new slow-flow is

$$\begin{aligned} \frac{dR_{10}}{d\eta} &= \frac{R_{10}}{2}\left[1 - AR_{20}^2 - CR_{10}^2\right] \\ \frac{dR_{20}}{d\eta} &= \frac{R_{20}}{2}\left[1 - AR_{10}^2 - CR_{20}^2\right] \\ \frac{d\Phi_0}{d\eta} &= 0 \end{aligned} \tag{6.13}$$

The slow-flows on R_{10} and R_{20} are the same as those on R_1 and R_2 in the non-3:1 resonance slow-flow (6.7) and therefore the equilibrium points of (6.13) are easy to calculate (see Table 6.3).

From our numerical investigations of the 3-dimensional phase space for (6.11) we expect the boundaries of the envelope we seek to correspond to infinite-period bifurcations occurring along an LCD having non-negligible values for R_1 and R_2 (as opposed to the LCD living in the $R_1 = 0$ plane). We identify this LCD with a line of non-isolated equilibrium points for (6.13) given by (see Table 6.3)

$$(R_{10}, R_{20}, \phi_0) = \left(\sqrt{\frac{1}{C+A}}, \sqrt{\frac{1}{C+A}}, k_0\right) \tag{6.14}$$

Substituting (6.14) back into the expanded slow-flow equations the next lowest order new slow-flow becomes

$$\begin{aligned}
\frac{dR_{11}}{d\eta} &= -\frac{A\sqrt{A+C}R_{21} + C\sqrt{A+C}R_{11} + 3B\cos k_0}{(A+C)^{\frac{3}{2}}} \\
\frac{dR_{21}}{d\eta} &= -\frac{(C^2+AC)R_{21} + (AC+A^2)R_{11} + B\sqrt{A+C}\cos k_0}{(A+C)^2} \\
\frac{d\Phi_1}{d\eta} &= \frac{10B\sin k_0 - (C+A)\gamma}{A+C}
\end{aligned} \tag{6.15}$$

Recall that the infinite-period bifurcations we are interested in occur in phase space along an LCD. Moreover, the slow-flow (6.15) on Φ_1 is uncoupled from the slow-flows on R_{11} and R_{21}, allowing us to study it without considering R_{11} and R_{21}. The right-hand side of (6.15) is secular and requiring it to vanish gives

$$\frac{10B\sin k_0 - (C+A)\gamma}{A+C} = 0$$

Table 6.3: The 9 equilibrium points of the lowest-order slow-flow (6.13). k_0 is a constant.

EQPT	$(R_{10}^*, R_{20}^*, \Phi_0^*)$
1	$(0, 0, k_0)$
2	$\left(0, \pm\sqrt{\frac{1}{C}}, k_0\right)$
3	$\left(\pm\sqrt{\frac{1}{C}}, 0, k_0\right)$
4	$\left(\pm\sqrt{\frac{1}{A+C}}, \pm\sqrt{\frac{1}{A+C}}, k_0\right)$

Solving this for $\sin k_0$ gives

$$\sin k_0 = -\frac{6\gamma s^2 + 9\gamma}{5s} \tag{6.16}$$

where we have replaced A, B, and C by their respective definitions. Taking the arcsine of (6.16) will generally result in 2 values for k_0 leading to 2 different equilibrium points (6.14). The infinite-period bifurcation will correspond to a double root of the arcsin of (6.16) which occurs when $|\sin k_0| = 1$. Solving this condition for γ yields

$$\gamma = \pm\frac{5s}{6s^2 + 9} \tag{6.17}$$

This equation represents two curves in γ-s parameter space along which infinite-period bifurcations of the equilibrium point (6.14) occur (see Figure 6.13). We can also use the relationship $\omega_2 = 3\omega_1 + \epsilon\gamma$ to view the bifurcation curves (6.17) in the original Δ-μ parameter space (see Figure 6.14).

We now check our perturbation results via numerical integration of the system (6.1) for two different parameter pairs near the 3:1 resonance region boundary (see Figure 6.15). For the first set of parameters numerical integration confirms the existence of a stable 3:1-periodic motion for the system *near*, but not on, the actual resonance curve (6.9) (see Figure 6.16). Therefore we find the effects of the

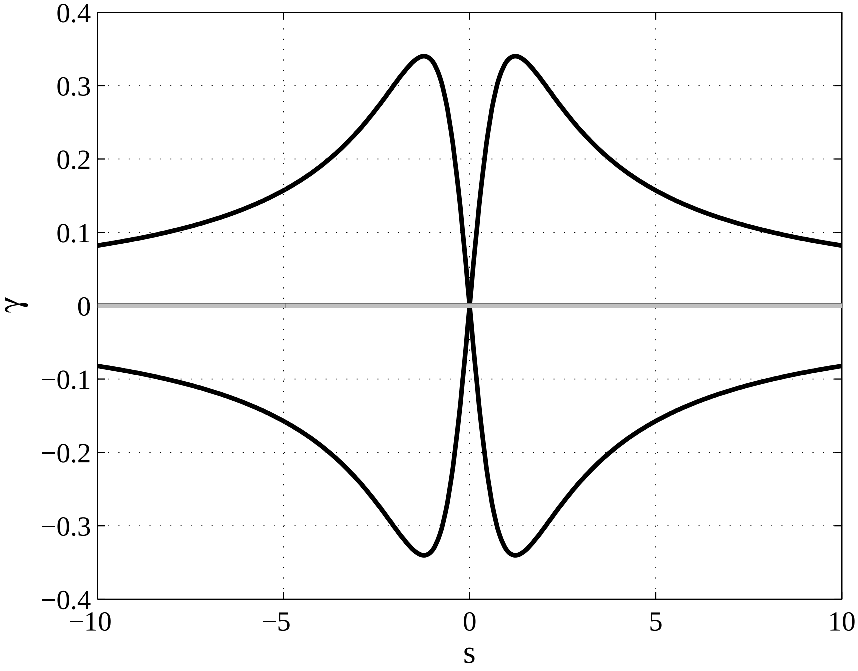

Figure 6.13: Bifurcation curves (6.17) for the new slow-flow (6.12). Given a value for the parameter s there exists a maximum detuning from the true 3:1 resonance curve (6.9) for which 3:1 periodic motions will exist. Infinite-period bifurcation = black line; 3:1 resonance curve (6.9) = gray line.

3:1 resonance are not confined to only the resonance curve (6.9) in parameter space, but an open region about this curve. For the second set of parameters, just on the other side of the resonance region boundary, the periodic motion has become quasi-periodic. Therefore (6.17) correctly predicts the bifurcation of a stable quasi-periodic motion into two 3:1-periodic motions (one stable, one unstable) for these parameter values.

SECOND PERTURBATION VS. AUTO2000 RESULTS

While numerical integration of the original system (6.1) confirms the results of our second perturbation method for certain parameter values, we now wish to check our results against a numerical bifurcation analysis for the 3:1 resonance slow-flow equations (6.11) using the AUTO2000 software package [6].

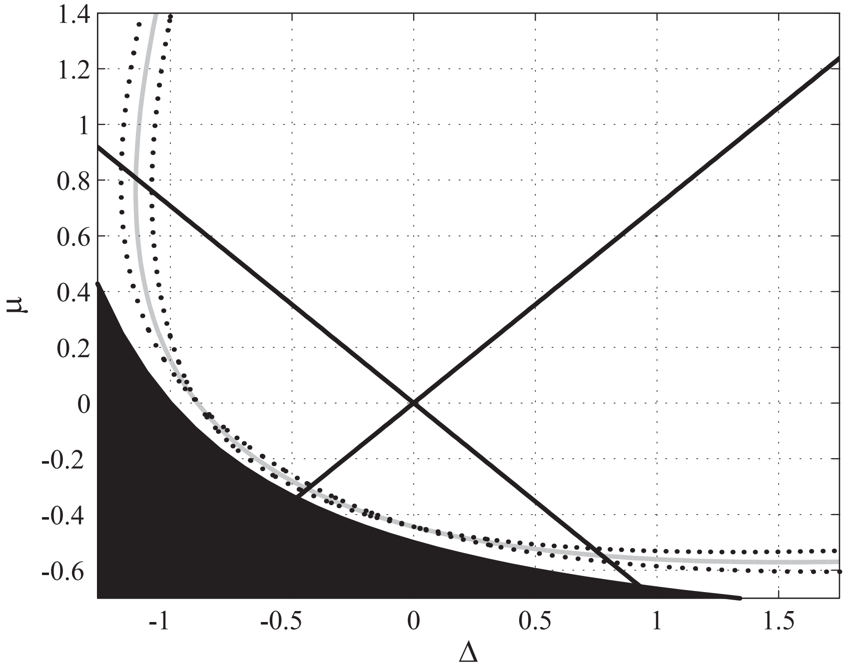

Figure 6.14: Bifurcation curves (6.17) for the new slow-flow (6.12) in Δ-μ parameter space (with $\epsilon = 0.5$ to enhance visibility). Infinite-period bifurcation curves = black dots; 3:1 resonance curve (6.9) = gray curve; bifurcation curves 6.8 for original slow-flow (6.7) = black lines. The black region represents parameter values where our analysis is not valid because the lowest-order approximations to the normal modes (6.5) are no longer periodic.

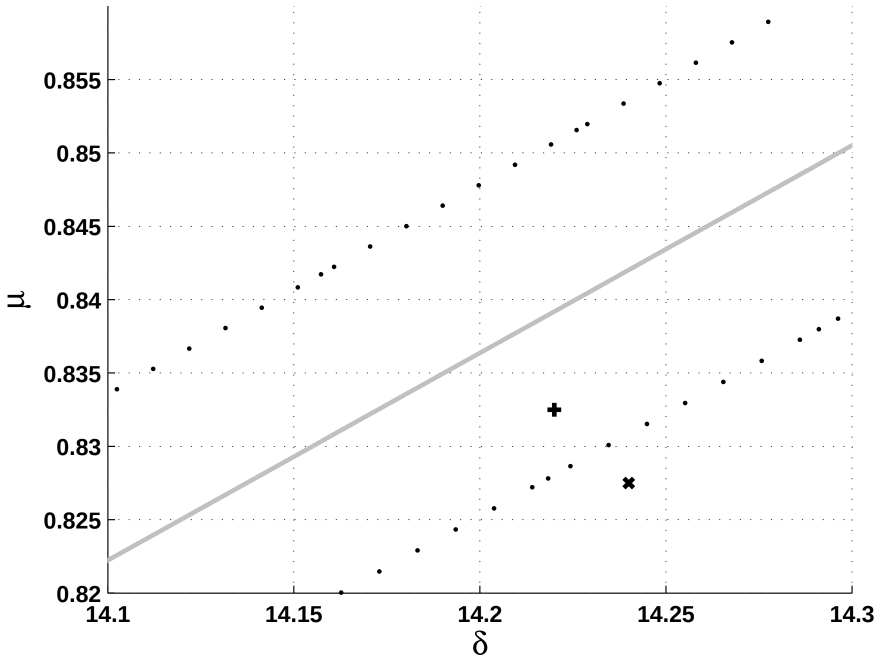

Figure 6.15: Parameter values used for the numerical integrations of (6.1) in Figure 6.16. $(\Delta, \mu) = (14.22, 0.8325)$ = plus sign; $(\Delta, \mu) = (14.24, 0.8275)$ = X; infinite-period bifurcation curves = black dots; 3:1 resonance curve (6.9) = gray line.

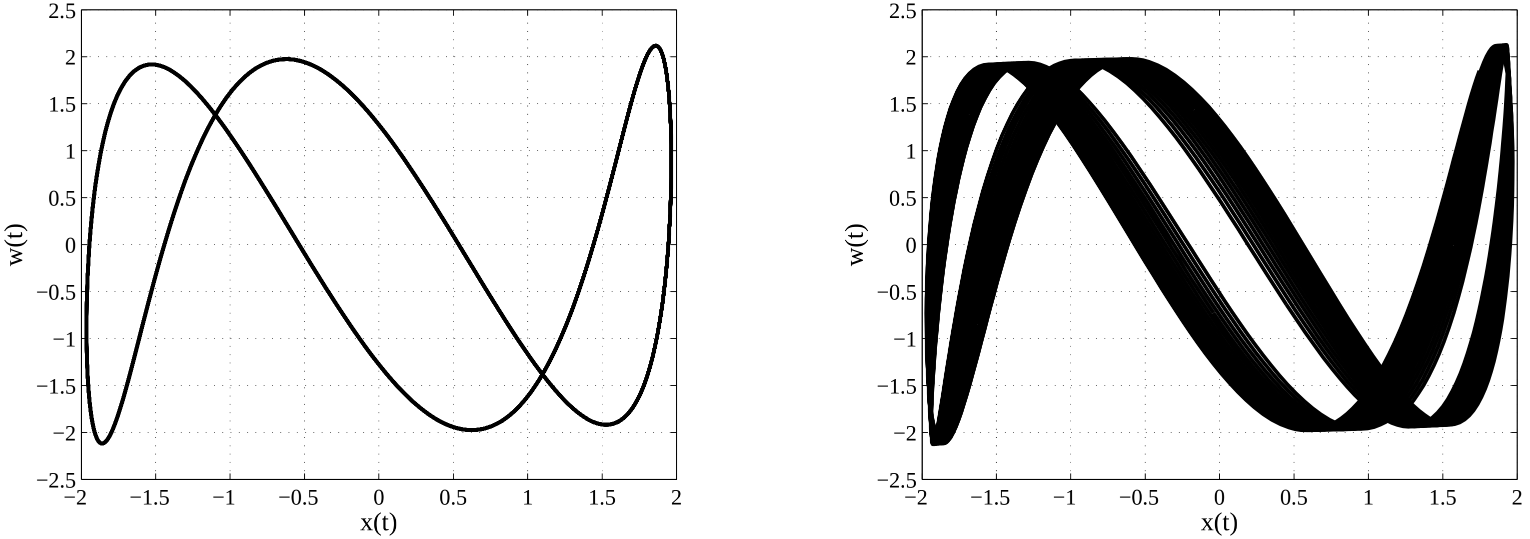

Figure 6.16: Numerical integrations of (6.1) performed with random initial conditions, $\epsilon = 0.1$, and parameter values $\Delta = 14.22$, $\mu = 0.8325$ ($s^2 \approx 72.94$) (left) and $\Delta = 14.24$, $\mu = 0.8275$ ($s^2 \approx 74.03$) (right) (see Figure 6.15). The left graph is an example of a stable 3:1-periodic motion that exists for parameter values within the boundary defined by (6.17). The right graph is an example of how a 3:1-periodic motion "fattens" into a quasi-periodic motion when we change parameter values and cross the boundary. Plotted in $x(t)$-$w(t)$ configuration space.

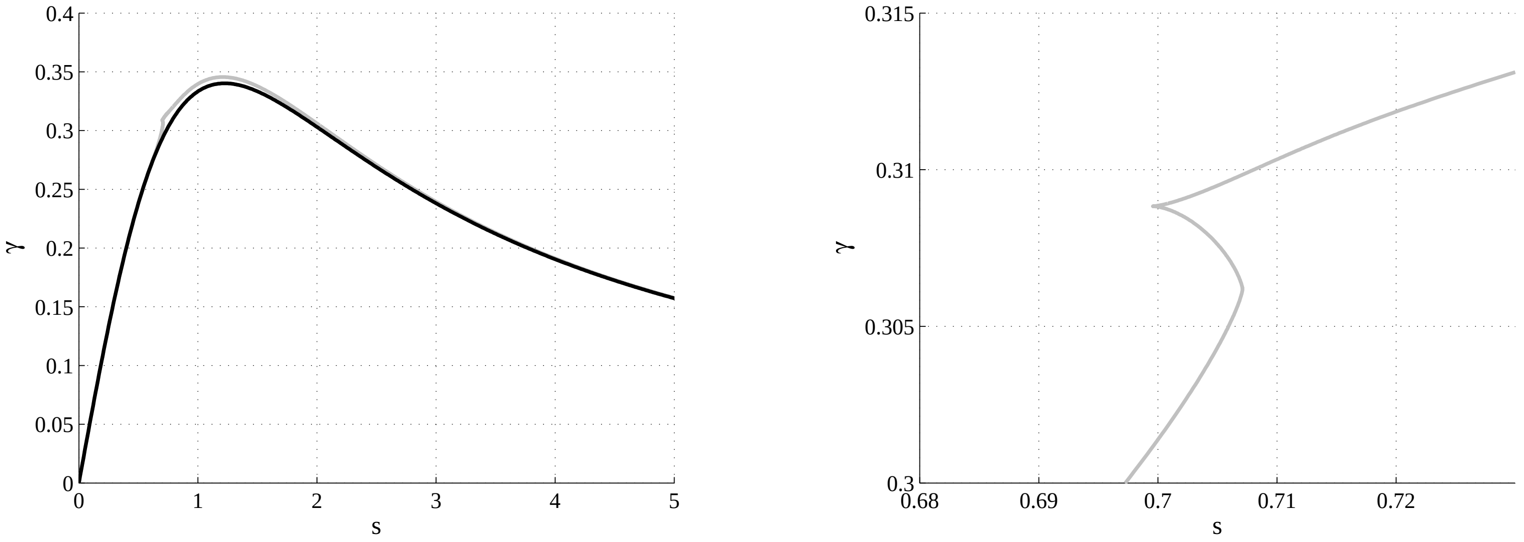

Figure 6.17: Comparison between infinite-period bifurcation curve (6.17) found via second perturbation method (black curve) and numerical results from AUTO2000 software package (gray curve). The two curves agree quite well for very small or very large values of the parameter s. For the approximate interval $0.7 < s < 2.2$ (6.17) underestimates the numerical curve and does not exhibit cusp and fold points like the numerically computed curve does.

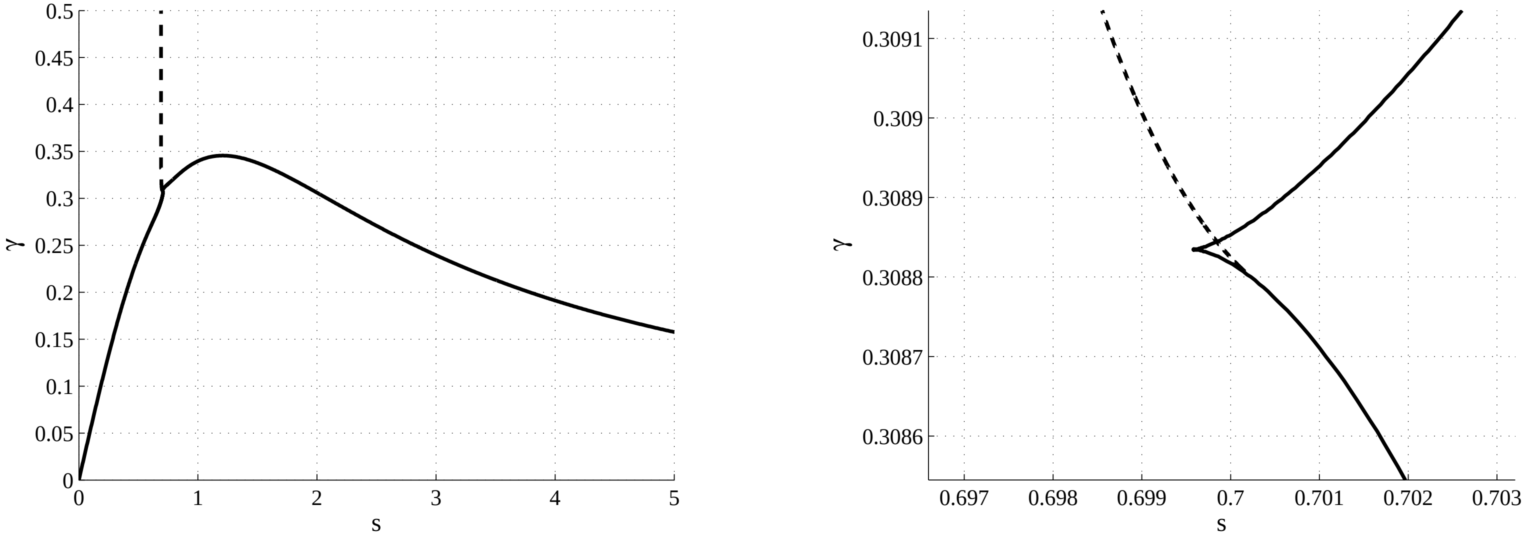

Figure 6.18: Numerical bifurcation curves computed with AUTO2000 for the slow-flow (6.11). The solid curve represents infinite-period bifurcations occurring along an LCD while the dashed curve represents Hopf bifurcations of the equilibrium point for (6.11) that lies near the singular $R_2 = 0$ plane. The Hopf bifurcation appears to be a second method for the creation of a stable 3:1 periodic motion for parameter values near the resonance curve (6.9).

Figure 6.17 shows a comparison between the approximate infinite-period bifurcation curve (6.17) computed via our regular perturbation method and the numerical bifurcation curve computed with AUTO2000 through numerical continuation of one of the two equilibrium points of (6.11) involved in the infinite-period bifurcation.

The existence of unexpected fold and cusp points in the numerically computed infinite-period bifurcation curve motivated us to perform numerical continuations on all other equilibrium points for (6.11) that we did not consider when applying our regular perturbation method. Figure 6.18 shows that there appears to exist a previously undetected Hopf bifurcation curve that originates near the cusp point. Numerical investigation reveals that the equilibrium point for (6.11) that lies near the singular $R_2 = 0$ plane (see Figure 6.10) undergoes a Hopf bifurcation along this new curve. This appears to be a second method for the creation of a stable 3:1 periodic motion for parameter values near the resonance curve (6.9). However, we do not investigate this Hopf bifurcation in more detail in this dissertation.

CHAPTER 7
CONCLUSIONS

Our goal for this dissertation has been to derive a simple mathematical model for the circadian system of Japanese quail that exhibits behavior similar to that seen in the experiments of Steele, et al. [22]. Each model involved indirectly coupling two identical oscillators, representing the rhythmic production of melatonin in each eye, via a third, detuned “extra-ocular” oscillator that combined the rhythmic melatonin production of the “neuroendocrine loop” with the melatonin present in the bloodstream.

We proposed 4 different mathematical models for the circadian system. Two systems were comprised of coupled weakly-nonlinear VDP oscillators while the other two were comprised of coupled phase oscillators. For each system we asked whether it agreed with the experiments. Steele, et al. experimentally showed that the ocular melatonin rhythms were both in-phase and stable [22]. These results support the conjecture that the eyes are the site of the primary pacemakers for the Japanese quail’s circadian system. We identified these pacemaking in-phase ocular melatonin rhythms with stable phase-locked in-phase modes for each system. For a model to agree with the experiments it must exhibit stable phase-locked in-phase modes for some set of parameters.

We have shown that 3 of the models, the weakly coupled VDP system (CHAPTERS 2 and 3), the second coupled phase oscillator system (CHAPTER 4), and the strongly coupled VDP system (CHAPTER 5), agree with the experiments. Only the first coupled phase oscillator system (CHAPTER 4) did not.

An interesting common dynamical feature for the systems that agreed with the experiments was a phase-locking region exhibiting stable in-phase modes that was not symmetric with respect to the detuning of the extra-ocular oscillator. That is, the phase-locking region was shifted left so that a larger proportion of parameter values where stable in-phase modes exist lie within the second quadrant of parameter space rather than the first (see Figures 3.1, 4.4, and 5.6). Moreover, phase-locking regions where *only* stable in-phase modes and no other stable dynamical motions are found exist exclusively in the second-quadrant of parameter space for the second phase oscillator (CHAPTER 4) and strongly coupled VDP (CHAPTER 5) systems.

What biological significance can we attach to this? If we were to conjecture that the in-phase ocular melatonin rhythms should be globally stable, then our results raise the interesting question of what the relative uncoupled frequency difference is between the ocular melatonin rhythms and the rhythmic production of melatonin by the neuroendocrine loop. Under this conjecture the second phase oscillator (4.7) and strongly coupled VDP (5.1) systems indicate that the uncoupled ocular melatonin rhythms should have a higher frequency, and thus lower period, than the uncoupled neuroendocrine loop's rhythm. This result suggests a possible measurement to be made by experimental biologists, and that is to experimentally determine the relative frequencies of the uncoupled ocular and extra-ocular oscillators. Our models predict that the uncoupled ocular frequencies will be higher.

Another interesting dynamical feature for the second phase oscillator system (4.7) is the potential importance of the amplitudes of oscillation on the existence of stable phase-locked in-phase modes. For this system there existed a minimum parameter value $A = \sqrt{2}$, which represented the ratio of amplitudes between the extra-ocular and a single ocular oscillator for the VDP model, for the system to exhibit stable phase-locked in-phase modes. Moreover, for the strongly coupled VDP system (5.1) the ratio of amplitudes for stable in-phase modes in phase-locking regions where *only* stable in-phase modes and no other stable dynamical motions are found, were similar to the minimum parameter value required in (4.7). These properties of the models compare favorably to experimental results [26] that have shown that when free-running, the ratio of plasma melatonin secreted by the neuroendocrine loop to that secreted by one eye in Japanese quail is approximately equal to 2.

APPENDIX A

Bifurcation Curves for the In-Phase Slow-Flow

Let $(R_1, R_3, \phi_1) = (r_1, r_3, \phi)$ represent an undetermined in-phase slow-flow equilibrium point for the in-phase slow-flow (2.4)-(2.6). Unfortunately we cannot solve for equilibrium points in closed-form due to the nonlinear nature of the in-phase slow-flow. Instead we look for curves in δ-μ parameter space representing saddle-node (or infinite-period) or Hopf bifurcations of equilibrium points. The following is taken directly from [19].

We begin by finding 2 linearly independent equations involving only the amplitudes r_1 and r_3 that must be satisfied by the equilibrium point in question. These equations have previously been derived in Chapter 2 and are given by (3.5) and (3.6). Next, using MACSYMA, we eliminate r_3 from (3.5) and (3.6). After neglecting any unnecessary factors, the resulting equation is simplified by substituting $r_1 = \sqrt{\rho_1}$ giving us

$$\begin{aligned}
&9\rho_1^6 - 156\rho_1^5 - 32\mu^2\rho_1^4 - 128\delta\mu\rho_1^4 - 128\delta^2\rho_1^4 + 1072\rho_1^4 - 576\mu^2\rho_1^3 - 3648\rho_1^3 \\
&+6912\mu^4\rho_1^2 + 10240\delta\mu^3\rho_1^2 + 14336\delta^2\mu^2\rho_1^2 + 7168\mu^2\rho_1^2 + 8192\delta^3\mu\rho_1^2 \\
&+7168\delta\mu\rho_1^2 + 4096\delta^4\rho_1^2 + 7168\delta^2\rho_1^2 + 6144\rho_1^2 - 36864\mu^4\rho_1 - 53248\delta\mu^3\rho_1 \\
&-69632\delta^2\mu^2\rho_1 - 21504\mu^2\rho_1 - 32768\delta^3\mu\rho_1 - 20480\delta\mu\rho_1 - 16384\delta^4\rho_1 \\
&-20480\delta^2\rho_1 - 4096\rho_1 + 36864\mu^4 + 16384\delta\mu^3 + 16384\delta^2\mu^2 + 16384\mu^2 \\
&= 0 \qquad \text{(A.1)}
\end{aligned}$$

Since a saddle-node (or infinite-period) bifurcation will occur at a double root, we require the derivative of (A.1) with respect to ρ_1 to be satisfied as well.

$$\begin{aligned}
&54\rho_1^5 - 780\rho_1^4 - 128\mu^2\rho_1^3 - 512\delta\mu\rho_1^3 - 512\delta^2\rho_1^3 + 4288\rho_1^3 - 1728\mu^2\rho_1^2 \\
&-10944\rho_1^2 + 13824\mu^4\rho_1 + 20480\delta\mu^3\rho_1 + 28672\delta^2\mu^2\rho_1 + 14336\mu^2\rho_1 \\
&+16384\delta^3\mu\rho_1 + 14336\delta\mu\rho_1 + 8192\delta^4\rho_1 + 14336\delta^2\rho_1 + 12288\rho_1 - 36864\mu^4 \\
&-53248\delta\mu^3 - 69632\delta^2\mu^2 - 21504\mu^2 - 32768\delta^3\mu - 20480\delta\mu - 16384\delta^4 \\
&-20480\delta^2 - 4096 = 0
\end{aligned} \tag{A.2}$$

We now eliminate ρ_1 from (A.1) and (A.2) to obtain an equation in terms of δ and μ only

$$\begin{aligned}
&45349632\mu^{14} + 221709312\delta\mu^{13} + 690508800\delta^2\mu^{12} + 9027936\mu^{12} \\
&+4924759904\delta^3\mu^{11} + 38320128\delta\mu^{11} + 2529857536\delta^4\mu^{10} + 1058273328\delta^2\mu^{10} \\
&-4323051\mu^{10} + 34209955584\delta^5\mu^9 + 2316472232\delta^3\mu^9 - 5105708\delta\mu^9 \\
&+38276136969\delta^6\mu^8 + 4535224322\delta^4\mu^8 - 3590948484\delta^2\mu^8 + 539217\mu^8 \\
&+35418275584\delta^7\mu^7 + 7219445766\delta^5\mu^7 - 6330432320\delta^3\mu^7 + 3036832\delta\mu^7 \\
&+27457617928\delta^8\mu^6 + 9198796806\delta^6\mu^6 - 8063788884\delta^4\mu^6 + 8802064\delta^2\mu^6 \\
&-12636\mu^6 + 17592483849\delta^9\mu^5 + 9121628167\delta^7\mu^5 - 3803212858\delta^5\mu^5 \\
&+7835616\delta^3\mu^5 - 183192\delta\mu^5 + 9308733344\delta^{10}\mu^4 + 7016693768\delta^8\mu^4 \\
&+4000742246\delta^6\mu^4 - 33819044\delta^4\mu^4 - 841176\delta^2\mu^4 - 81\mu^4 + 392167424\delta^{11}\mu^3 \\
&+4109107209\delta^9\mu^3 + 813588487\delta^7\mu^3 - 3334912\delta^5\mu^3 - 1019520\delta^3\mu^3 \\
&+2640\delta\mu^3 + 1289748481\delta^{12}\mu^2 + 1773404161\delta^{10}\mu^2 + 65590272\delta^8\mu^2 \\
&+7929600\delta^6\mu^2 + 231360\delta^4\mu^2 + 20304\delta^2\mu^2 + 29360128\delta^{13}\mu + 51904512\delta^{11}\mu \\
&+30167040\delta^9\mu + 7749632\delta^7\mu + 889344\delta^5\mu + 35328\delta^3\mu + 16\delta\mu
\end{aligned}$$

$$+4194304\delta^{14} + 8650752\delta^{12} + 6033408\delta^{10} + 1937408\delta^{8} + 296448\delta^{6}$$

$$+17664\delta^{4} + 16\delta^{2} = 0 \tag{A.3}$$

This equation plots as two triangular regions in δ-μ parameter space (see Figure 2.1). The sides of the triangular regions represent either saddle-node or infinite-period bifurcations (see [19] for a complete description).

Next we look for curves representing Hopf bifurcations. These bifurcations correspond to a stable equilibrium point losing its stability as 2 of its eigenvalues cross the imaginary axis. We once again look at an undetermined equilibrium point $(R_1, R_3, \phi_1) = (r_1, r_3, \phi)$. The linearized flow near this equilibrium point is given via the Jacobian of (2.4)-(2.6) evaluated at the point.

$$\begin{bmatrix} \frac{1}{3} - \frac{3r_1^2}{8} & -\frac{\mu \sin\phi}{2} & -\frac{\mu r_3 \cos\phi}{2} \\ \mu \sin\phi & \frac{1}{3} - \frac{3r_3^2}{8} & \mu r_1 \cos\phi \\ \frac{\mu r_3 \cos\phi}{2r_1^2} + \frac{\mu \cos\phi}{r_3} & -\frac{\mu r_1 \cos\phi}{r_3^2} - \frac{\mu \cos\phi}{2r_1} & \frac{\mu r_3 \sin\phi}{2r_1} - \frac{\mu r_1 \sin\phi}{r_3} \end{bmatrix}$$

The Jacobian can be simplified by using equations (3.2) and (3.3) to eliminate $\cos\phi$ and $\sin\phi$. The resulting characteristic equation of the Jacobian, which contains only r_1 and r_3, is of the form

$$\lambda^3 + c_2\lambda^2 + c_1\lambda + c_0 = 0 \tag{A.4}$$

For a Hopf bifurcation to occur, there must exist a pair of purely imaginary eigenvalues satisfying (A.4). This requires the characteristic equation to have the form [17]

$$\lambda^3 - \alpha\lambda^2 + \beta^2\lambda - \beta^2\alpha = 0$$

or in terms of the coefficients of (A.4)

$$c_0 = c_1 c_2 \tag{A.5}$$

Now we eliminate r_1 and r_3 using equations (3.6) and (A.1). First we use (3.6) to eliminate r_3 from (A.5) to get

$$\begin{aligned}
&8019\rho_1^8 - 138672\rho_1^7 + 11232\mu^2\rho_1^6 + 44928\delta\mu\rho_1^6 + 44928\delta^2\rho_1^6 + 963468\rho_1^6\\
&-101376\mu^2\rho_1^5 - 405504\delta\mu\rho_1^5 - 405504\delta^2\rho_1^5 - 3380832\rho_1^5 + 6912\mu^4\rho_1^4\\
&+55296\delta\mu^3\rho_1^4 + 165888\delta^2\mu^2\rho_1^4 + 195456\mu^2\rho_1^4 + 221184\delta^3\mu\rho_1^4 + 781824\delta\mu\rho_1^4\\
&+110592\delta^4\rho_1^4 + 781824\delta^2\rho_1^4 + 6014784\rho_1^4 - 36864\mu^4\rho_1^3 - 294912\delta\mu^3\rho_1^3\\
&-884736\delta^2\mu^2\rho_1^3 + 455168\mu^2\rho_1^3 - 1179648\delta^3\mu\rho_1^3 + 1820672\delta\mu\rho_1^3\\
&-589824\delta^4\rho_1^3 + 1820672\delta^2\rho_1^3 - 4143616\rho_1^3 + 27648\mu^4\rho_1^2 + 221184\delta\mu^3\rho_1^2\\
&+663552\delta^2\mu^2\rho_1^2 - 1459200\mu^2\rho_1^2 + 884736\delta^3\mu\rho_1^2 - 5836800\delta\mu\rho_1^2\\
&+442368\delta^4\rho_1^2 - 5836800\delta^2\rho_1^2 - 1290240\rho_1^2 + 294912\mu^2\rho_1 + 1179648\delta\mu\rho_1\\
&+1179648\delta^2\rho_1 + 1867776\rho_1 + 524288\mu^2 + 2097152\delta\mu + 2097152\delta^2\\
&+524288 = 0
\end{aligned}$$

where $\rho_1 = r_1^2$. Then we use (A.1) to eliminate ρ_1 from this equation giving us

$$\begin{aligned}
&206046997776\mu^{16} + 128246239872\delta\mu^{15} - 10552996535 04\delta^2\mu^{14}\\
&+151716144096\mu^{14} - 4792910330880\delta^3\mu^{13} - 959470912224\delta\mu^{13}\\
&-10067384941056\delta^4\mu^{12} - 4022175416544\delta^2\mu^{12} - 76183604811\mu^{12}\\
&-13620666378240\delta^5\mu^{11} - 8422624949760\delta^3\mu^{11} - 1162076374872\delta\mu^{11}\\
&-11038023456768\delta^6\mu^{10} - 9771098692608\delta^4\mu^{10} - 2453769115848\delta^2\mu^{10}\\
&-53727633963\mu^{10} - 1633265565696\Delta^7\mu^9 - 5111334563328\delta^5\mu^9 \ldots
\end{aligned}$$

$$
\begin{aligned}
&\ldots - 2698414682336\delta^3\mu^9 - 3687306193 08\delta\mu^9 + 10450239639552\delta^8\mu^8 \\
&+4596633773568\delta^6\mu^8 - 930295796592\delta^4\mu^8 - 500042378940\delta^2\mu^8 \\
&-10567871928\mu^8 + 189553130864464\delta^9\mu^7 + 146545847009 28\delta^7\mu^7 \\
&+2928072365568\delta^5\mu^7 - 65251243872\delta^3\mu^7 - 43666800936\delta\mu^7 \\
&+20325924864000\delta^{10}\mu^6 + 197347953254 40\delta^8\mu^6 + 6459457683968\delta^6\mu^6 \\
&+646749530928\delta^4\mu^6 - 25863482760\delta^2\mu^6 - 842897393\mu^6 \\
&+15864307384320\delta^{11}\mu^5 + 18526299439104\delta^9\mu^5 + 7894980157440\delta^7\mu^5 \\
&+1385895931968\delta^5\mu^5 + 75604570176\delta^3\mu^5 - 1221626868\delta\mu^5 \\
&+9417278619648\delta^{12}\mu^4 + 12970012852224\delta^{10}\mu^4 + 6670762715136\delta^8\mu^4 \\
&+1563045302976\delta^6\mu^4 + 151762831008\delta^4\mu^4 + 2639537484\delta^2\mu^4 \\
&-16895076\mu^4 + 4277139406848\Delta^{13}\mu^3 + 6902205382656\delta^{11}\mu^3 \\
&+4225522688000\delta^9\mu^3 + 1243790340096\delta^7\mu^3 + 175856646912\delta^5\mu^3 \\
&+9882465920\delta^3\mu^3 + 1040635 68\delta\mu^3 + 1433187385344\delta^{14}\mu^2 \\
&+2690954035200\delta^{12}\mu^2 + 1939282108416\delta^{10}\mu^2 + 685956946944\delta^8\mu^2 \\
&+123792201984\delta^6\mu^2 + 10341576000\delta^4\mu^2 + 273469584\delta^2\mu^2 \\
&+1086528\mu^2 + 328866988032\delta^{15}\mu + 711039909888\delta^{13}\mu \\
&+596824129536\delta^{11}\mu + 250006241280\delta^9\mu + 55862845440\delta^7\mu \\
&+6480411648\delta^5\mu + 338812032\delta^3\mu + 5262144\delta\mu \\
&+41108373504\delta^{16} + 101577129984\delta^{14} + 99470688256\delta^{12} \\
&+50001248256\delta^{10} + 13965711360\delta^8 + 2160137216\delta^6 \\
&+169406016\delta^4 + 5262144\delta^2 + 43264 = 0
\end{aligned}
\tag{A.6}
$$

This equation plots as 4 curves originating *near* the corners of the triangular regions defined by (A.3) (see Figures 2.1 and A.1).

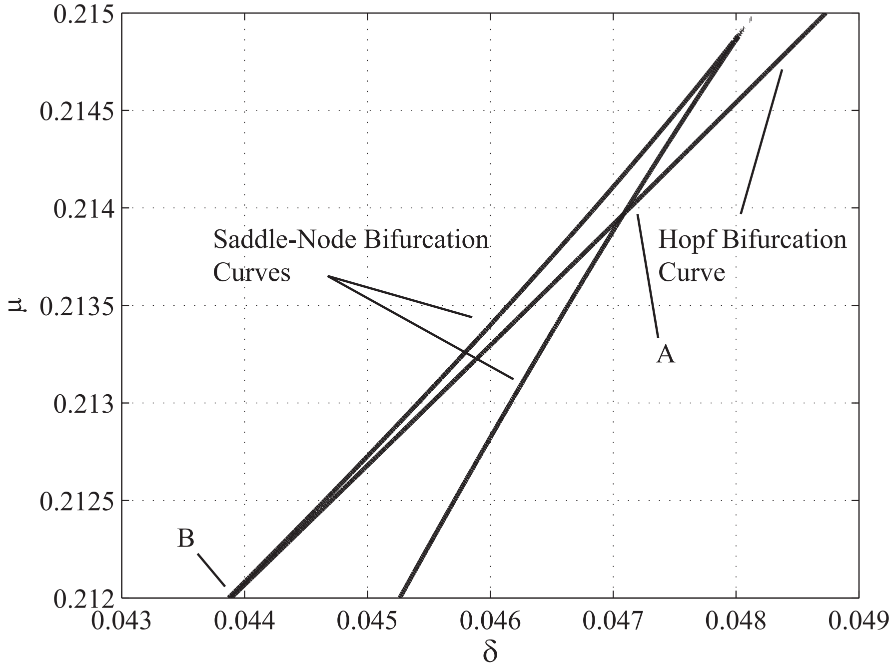

Figure A.1: Close-up view of intersection of saddle-node (A.3) and Hopf (A.6) bifurcation curves. The curves intersect at point A and are tangent at point B.

APPENDIX B

MATLAB Code for Numerical Floquet Analysis

```
function y = floquet_inphase()
%% SET-UP
% Clear screen and workspace variables, start timer.
clear; clc; tic;
% Define parameter space grid size.
step_size = .025;
% Define nonlinearity parameter epsilon.
epsilon = 0.1;
% Initialize results counter.
counter = 1;
% Initialize vector to store results.
results = zeros((1/step_size)*(.5/step_size)+1,5);

%% NUMERICAL FLOQUET ANALYSIS
for mu = [step_size:step_size:.5]
    % Restrict to region of parameter space where we expect
    % periodic motions to exist.
    for delta = [max([-.5 -2*mu]):step_size:mu]

        % Initialize variables.
        begin_time = 0;
        period = 0;
        sol = 0;

        % Define parameter vector.
        parameters = [epsilon;delta;mu];

        % Define options for ode45 numerical integration.
        options = odeset('Events',@EVENTS,'AbsTol',1e-7,...
            'RelTol',1e-4);

        % Numerically integrate in-phase subspace equations.
        sol = ode45(@inphase,[0 1250],[0;2;-2;-.1],options,...
            parameters);

        % Calculate the period of the steady-state solution
        % and the time at which it begins.
        [period,begin_time] = calculate_period(sol);

        % If the numerical integration does not settle down
        % to a steady-state, skip the rest of the loop and
        % go to next (delta,mu) pair.
        if period == 0
            % No periodic motion exists.
```

```
            results(counter,:) = [delta mu 0 period 0];
            counter = counter + 1;
            continue;
        end

        % Find numerical representation of steady-state
        % periodic motion.
        interval = [begin_time-.01:.01:begin_time+period+.01];
        inphase_mode = [interval' deval(sol,interval)'];

        % Calculate the monodromy matrix.
        C = monodromy_matrix(period,begin_time,inphase_mode,...
            parameters);

        % Calculate the eigenvalues of the monodromy matrix.
        eigenvalues = sort(eig(C));

        % Determine stability of periodic motion by checking
        % if any eigenvales have norm > 1.
        if((abs(eigenvalues(end))-1) > 1e-3)
            % Motion is unstable.
            results(counter,:) = [delta mu 1 period...
                abs(eigenvalues(end))];
            counter = counter + 1;
        else
            % Motion is stable.
            results(counter,:) = [delta mu 2 period...
                abs(eigenvalues(end))];
            counter = counter + 1;
        end
    end
end

% Plot results.
floquet_plot(results);

% Save results to .mat file for later use.
%save output results;

% Stop timer.
toc;

% Return results vector at completion.
y = results;

%% SUBFUNCTIONS
```

```
%% CALCULATE_PERIOD
function [period,begin_time] = calculate_period(sol)

intervals = abs(diff(sol.ye,1,2));
indices = find(vnorm(intervals,1) < 1e-3);

if ~isempty(indices)
    period = sol.xe(indices(end)) - sol.xe(indices(end)-1);
    begin_time = sol.xe(indices(end)-1);
else
    period = 0;
    begin_time = 0;
end

%% MONODROMY_MATRIX
function C = monodromy_matrix(period,begin_time,...
    inphase_mode,parameters)

C = zeros(6,6);
I = eye(6);
options = odeset('AbsTol',1e-7,'RelTol',1e-4);

for i = 1:6
    [T,Y] = ode45(@inphase_variational,[0 period],I(:,i),...
        options,begin_time,inphase_mode,parameters);
    C(:,i) = Y(end,:)';
end

%% FLOQUET_PLOT
function y = floquet_plot(results)

figure(1);hold on;

for i = 1:length(results)
    if(results(i,3)==0)
        plot(results(i,1),results(i,2),'bx','LineWidth',6);
    elseif(results(i,3)==1)
        plot(results(i,1),results(i,2),'rx','LineWidth',6);
    else
        plot(results(i,1),results(i,2),'gx','LineWidth',6);
    end
end

xlabel('\delta'); ylabel('\mu');
grid on;
axis([-.5 .5 0 .5]);
```

```
test = get(gca,'XLabel');
set(test,'FontSize',14,'FontName','Times');
test = get(gca,'YLabel');
set(test,'FontSize',14,'FontName','Times');
set(gca,'FontSize',12,'FontName','Times');

y = 1;

%% IN-PHASE EQUATIONS
function y = inphase(t,x,p)

y = [x(2);
     p(1)*(1-x(1)^2)*x(2) - x(1) + p(1)*p(3)*(x(3)-x(1));
     x(4);
     p(1)*(1-x(3)^2)*x(4) - (1+p(1)*p(2))^2*x(3)...
     + p(1)*2*p(3)*(x(1)-x(3))];

%% VARIATIONAL EQUATIONS
function y = inphase_variational(t,x,begin_time,inphase_mode,p)

temp = interp1q(inphase_mode(:,1),inphase_mode(:,2:5),...
     begin_time+t);

y = [x(2);
     (-p(1)*p(3) - (1 + 2*p(1)*temp(1)*temp(2)))*x(1)...
     + p(1)*(1-temp(1)^2)*x(2) + p(1)*p(3)*x(5);
     x(4);
     (-p(1)*p(3) - (1 + 2*p(1)*temp(1)*temp(2)))*x(3)...
     + p(1)*(1-temp(1)^2)*x(4) + p(1)*p(3)*x(5);
     x(6);
     (-2*p(1)*p(3) - ((1 + p(1)*p(2))^2 ...
     + 2*p(1)*temp(3)*temp(4)))*x(5)...
     + p(1)*(1-temp(3)^2)*x(6) + p(1)*p(3)*x(1)...
     + p(1)*p(3)*x(3)];

%% EVENTS
function [value, isterminal, direction] = EVENTS(t,y,p)

value = y(1);
isterminal = 0;
direction = +1;
```

Figure B.1: MATLAB code for performing numerical Floquet analysis on the in-phase mode in CHAPTER 2.

APPENDIX C

Table C.1: Coefficients of nonsecular terms in (5.13) for the first normal mode.

Frequency	Cosine Terms	Sine Terms
$2\omega_3 + \omega_1$	$-\frac{\beta(\alpha\beta-1)\sin(2\theta_3+\theta_1)R_1R_3^2(2\omega_3+\omega_1)}{4(\beta-\alpha)}$	$\frac{\beta(\alpha\beta-1)\cos(2\theta_3+\theta_1)R_1R_3^2(2\omega_3+\omega_1)}{4(\beta-\alpha)}$
$2\omega_3 - \omega_1$	$-\frac{\beta(\alpha\beta-1)\sin(2\theta_3-\theta_1)R_1R_3^2(2\omega_3-\omega_1)}{4(\beta-\alpha)}$	$\frac{\beta(\alpha\beta-1)\cos(2\theta_3-\theta_1)R_1R_3^2(2\omega_3-\omega_1)}{4(\beta-\alpha)}$
$\omega_3 + 2\omega_2$	$\frac{\beta\sin(\theta_3+2\theta_2)R_2^2R_3(\omega_3+2\omega_2)}{4(\beta-\alpha)}$	$-\frac{\beta\cos(\theta_3+2\theta_2)R_2^2R_3(\omega_3+2\omega_2)}{4(\beta-\alpha)}$
$\omega_3 - 2\omega_2$	$\frac{\beta\sin(\theta_3-2\theta_2)R_2^2R_3(\omega_3-2\omega_2)}{4(\beta-\alpha)}$	$-\frac{\beta\cos(\theta_3-2\theta_2)R_2^2R_3(\omega_3-2\omega_2)}{4(\beta-\alpha)}$
$\omega_3 + 2\omega_1$	$-\frac{(\alpha-1)(\alpha+1)\beta\sin(\theta_3+2\theta_1)R_1^2R_3(\omega_3+2\omega_1)}{4(\beta-\alpha)}$	$\frac{(\alpha-1)(\alpha+1)\beta\cos(\theta_3+2\theta_1)R_1^2R_3(\omega_3+2\omega_1)}{4(\beta-\alpha)}$
$\omega_3 - 2\omega_1$	$-\frac{(\alpha-1)(\alpha+1)\beta\sin(\theta_3-2\theta_1)R_1^2R_3(\omega_3-2\omega_1)}{4(\beta-\alpha)}$	$\frac{(\alpha-1)(\alpha+1)\beta\cos(\theta_3-2\theta_1)R_1^2R_3(\omega_3-2\omega_1)}{4(\beta-\alpha)}$
$2\omega_2 + \omega_1$	$\frac{\beta\sin(2\theta_2+\theta_1)R_1R_2^2(2\omega_2+\omega_1)}{4(\beta-\alpha)}$	$-\frac{\beta\cos(2\theta_2+\theta_1)R_1R_2^2(2\omega_2+\omega_1)}{4(\beta-\alpha)}$
$2\omega_2 - \omega_1$	$\frac{\beta\sin(2\theta_2-\theta_1)R_1R_2^2(2\omega_2-\omega_1)}{4(\beta-\alpha)}$	$-\frac{\beta\cos(2\theta_2-\theta_1)R_1R_2^2(2\omega_2-\omega_1)}{4(\beta-\alpha)}$
$3\omega_3$	$-\frac{(\beta-1)\beta(\beta+1)\sin(3\theta_3)R_3^3\omega_3}{4(\beta-\alpha)}$	$\frac{(\beta-1)\beta(\beta+1)\cos(3\theta_3)R_3^3\omega_3}{4(\beta-\alpha)}$
ω_3	$-\frac{\beta\sin(\theta_3)R_3(\beta^2R_3^2-R_3^2-2R_2^2+2\alpha^2R_1^2-2R_1^2)\omega_3}{4(\beta-\alpha)}$	$\frac{\beta\cos\theta_3R_3(\beta^2R_3^2-R_3^2-2R_2^2+2\alpha^2R_1^2-2R_1^2)\omega_3}{4(\beta-\alpha)}$
$3\omega_1$	$\frac{(\beta-\alpha^3)\sin(3\theta_1)R_1^3\omega_1}{4(\beta-\alpha)}$	$-\frac{(\beta-\alpha^3)\cos(3\theta_1)R_1^3\omega_1}{4(\beta-\alpha)}$

Table C.2: Coefficients of nonsecular terms in (5.13) for the second normal mode.

Frequency	Cosine Terms	Sine Terms
$2\omega_3 + \omega_2$	$\frac{1}{4}\sin(2\theta_3 + \theta_2) R_2 R_3^2 (2\omega_3 + \omega_2)$	$-\frac{1}{4}\cos(2\theta_3 + \theta_2) R_2 R_3^2 (2\omega_3 + \omega_2)$
$2\omega_3 - \omega_2$	$\frac{1}{4}\sin(2\theta_3 - \theta_2) R_2 R_3^2 (2\omega_3 - \omega_2)$	$-\frac{1}{4}\cos(2\theta_3 - \theta_2) R_2 R_3^2 (2\omega_3 - \omega_2)$
$\omega_3 + \omega_2 + \omega_1$	$\frac{1}{2}\sin(\theta_3 + \theta_2 + \theta_1) R_1 R_2 R_3 (\omega_3 + \omega_2 + \omega_1)$	$-\frac{1}{2}\cos(\theta_3 + \theta_2 + \theta_1) R_1 R_2 R_3 (\omega_3 + \omega_2 + \omega_1)$
$\omega_3 + \omega_2 - \omega_1$	$\frac{1}{2}\sin(\theta_3 + \theta_2 - \theta_1) R_1 R_2 R_3 (\omega_3 + \omega_2 - \omega_1)$	$-\frac{1}{2}\cos(\theta_3 + \theta_2 - \theta_1) R_1 R_2 R_3 (\omega_3 + \omega_2 - \omega_1)$
$\omega_3 - \omega_2 + \omega_1$	$\frac{1}{2}\sin(\theta_3 - \theta_2 + \theta_1) R_1 R_2 R_3 (\omega_3 - \omega_2 + \omega_1)$	$-\frac{1}{2}\cos(\theta_3 - \theta_2 + \theta_1) R_1 R_2 R_3 (\omega_3 - \omega_2 + \omega_1)$
$\omega_3 - \omega_2 - \omega_1$	$\frac{1}{2}\sin(\theta_3 - \theta_2 - \theta_1) R_1 R_2 R_3 (\omega_3 - \omega_2 - \omega_1)$	$-\frac{1}{2}\cos(\theta_3 - \theta_2 - \theta_1) R_1 R_2 R_3 (\omega_3 - \omega_2 - \omega_1)$
$\omega_2 + 2\omega_1$	$\frac{1}{4}\sin(\theta_2 + 2\theta_1) R_1^2 R_2 (\omega_2 + 2\omega_1)$	$-\frac{1}{4}\cos(\theta_2 + 2\theta_1) R_1^2 R_2 (\omega_2 + 2\omega_1)$
$\omega_2 - 2\omega_1$	$\frac{1}{4}\sin(\theta_2 - 2\theta_1) R_1^2 R_2 (\omega_2 - 2\omega_1)$	$-\frac{1}{4}\cos(\theta_2 - 2\theta_1) R_1^2 R_2 (\omega_2 - 2\omega_1)$
$3\omega_2$	$\frac{1}{4}\sin(3\theta_2) R_2^3 \omega_2$	$-\frac{1}{4}\cos(3\theta_2) R_2^3 \omega_2$

Table C.3: Coefficients of nonsecular terms in (5.13) for the third normal mode.

Frequency	Cosine Terms	Sine Terms
$2\omega_3+\omega_1$	$\frac{\alpha(\beta-1)(\beta+1)\sin(2\theta_3+\theta_1)R_1R_3^2(2\omega_3+\omega_1)}{4(\beta-\alpha)}$	$-\frac{\alpha(\beta-1)(\beta+1)\cos(2\theta_3+\theta_1)R_1R_3^2(2\omega_3+\omega_1)}{4(\beta-\alpha)}$
$2\omega_3-\omega_1$	$\frac{\alpha(\beta-1)(\beta+1)\sin(2\theta_3-\theta_1)R_1R_3^2(2\omega_3-\omega_1)}{4(\beta-\alpha)}$	$-\frac{\alpha(\beta-1)(\beta+1)\cos(2\theta_3-\theta_1)R_1R_3^2(2\omega_3-\omega_1)}{4(\beta-\alpha)}$
$\omega_3+2\omega_2$	$-\frac{\alpha\sin(\theta_3+2\theta_2)R_2^2R_3(\omega_3+2\omega_2)}{4(\beta-\alpha)}$	$\frac{\alpha\cos(\theta_3+2\theta_2)R_2^2R_3(\omega_3+2\omega_2)}{4(\beta-\alpha)}$
$\omega_3-2\omega_2$	$-\frac{\alpha\sin(\theta_3-2\theta_2)R_2^2R_3(\omega_3-2\omega_2)}{4(\beta-\alpha)}$	$\frac{\alpha\cos(\theta_3-2\theta_2)R_2^2R_3(\omega_3-2\omega_2)}{4(\beta-\alpha)}$
$\omega_3+2\omega_1$	$\frac{\alpha(\alpha\beta-1)\sin(\theta_3+2\theta_1)R_1^2R_3(\omega_3+2\omega_1)}{4(\beta-\alpha)}$	$-\frac{\alpha(\alpha\beta-1)\cos(\theta_3+2\theta_1)R_1^2R_3(\omega_3+2\omega_1)}{4(\beta-\alpha)}$
$\omega_3-2\omega_1$	$\frac{\alpha(\alpha\beta-1)\sin(\theta_3-2\theta_1)R_1^2R_3(\omega_3-2\omega_1)}{4(\beta-\alpha)}$	$-\frac{\alpha(\alpha\beta-1)\cos(\theta_3-2\theta_1)R_1^2R_3(\omega_3-2\omega_1)}{4(\beta-\alpha)}$
$2\omega_2+\omega_1$	$-\frac{\alpha\sin(2\omega_2+\omega_1)R_1R_2^2(2\omega_2+\omega_1)}{4(\beta-\alpha)}$	$\frac{\alpha\cos(2\omega_2+\omega_1)R_1R_2^2(2\omega_2+\omega_1)}{4(\beta-\alpha)}$
$2\omega_2-\omega_1$	$-\frac{\alpha\sin(2\omega_2-\omega_1)R_1R_2^2(2\omega_2-\omega_1)}{4(\beta-\alpha)}$	$\frac{\alpha\cos(2\omega_2-\omega_1)R_1R_2^2(2\omega_2-\omega_1)}{4(\beta-\alpha)}$
$3\omega_3$	$\frac{(\beta^3-\alpha)\sin(3\theta_3)R_3^3\omega_3}{4(\beta-\alpha)}$	$-\frac{(\beta^3-\alpha)\cos(3\theta_3)R_3^3\omega_3}{4(\beta-\alpha)}$
$3\omega_1$	$\frac{(\alpha-1)\alpha(\alpha+1)\sin(3\theta_1)R_1^3\omega_1}{4(\beta-\alpha)}$	$-\frac{(\alpha-1)\alpha(\alpha+1)\cos(3\theta_1)R_1^3\omega_1}{4(\beta-\alpha)}$
ω_1	$\frac{\alpha\sin\theta_1R_1(2\beta^2R_3^2-2R_3^3-2R_2^2+\alpha^2R_1^2-R_1^2)\omega_1}{4(\beta-\alpha)}$	$-\frac{\alpha\cos\theta_1R_1(2\beta^2R_3^2-2R_3^3-2R_2^2+\alpha^2R_1^2-R_1^2)\omega_1}{4(\beta-\alpha)}$

BIBLIOGRAPHY

[1] Camacho, E.T., Rand, R.H., and Howland, H., “Dynamics of two van der Pol oscillators coupled via a bath.” *Int. J. Solids Struct.* 41 (2004): 2133-2143.

[2] Cassone, V. and Menaker, M., “Is the Avian Circadian System a Neuroendocrine Loop?” *J. Exp. Zoo.* 232 (1984): 539-549.

[3] Cesari, L., *Asymptotic Behavior and Stability Problems in Ordinary Differential Equations*. Academic Press Inc., New York, New York, 1963.

[4] Chakraborty, T., *Bifurcation analysis of two weakly coupled Van der Pol oscillators*. Doctoral thesis, Cornell University, 1986.

[5] Chakraborty, T. and Rand, R.H., “The transition from phase locking to drift in a system of two weakly coupled van der Pol oscillators.” *Int. J. Nonlinear Mech.* 23 (1988): 369-276.

[6] Doedel, E.J., Paffenroth, R.C., Champneys, A.R., Fairgrieve, T.F., Kuznetsov, Y.A., Oldeman, B.E., Sandstede, B., and Wang, X., *AUTO 2000: Continuation and Bifurcation Software for Ordinary Differential Equations (with HomCont)*. July 30, 2002. <http://indy.cs.concordia.ca/auto/>.

[7] Govorukhin, V.N., *MATDS - MATLAB based program for dynamical systems investigation*. Last Updated: 20 May 2004. Accessed: 31 Mar 2008. <http://kvm.math.rsu.ru/matds/>.

[8] Ivanchenko, M.V., Osipov, G.V., Shalfeev, V.D., and Kurths, J., “Synchronization of two non-scalar-coupled limit-cycle oscillators.” *Physica D* 189 (2004): 8-30.

[9] Janik, D., Dittami, J., and Gwinner, E., “The Effect of Pinealectomy on Circadian Plasma Melatonin Levels in House Sparrows and European Starlings.” *J. Biol. Rhythms* 7 (1992): 277-286.

[10] Li, X., Ji, J.C., and Hansen, C.H., “Non-linear normal modes and their bifurcation of a two DOF system with quadratic and cubic non-linearity.” *Int. J. Non Linear Mech.* 41 (2006): 1028-1038.

[11] Love, T., *Cambridge University Engineering Department - Matlab: faster scripts*. Last Updated: May 2008. Accessed: 29 May 2008. <http://www-h.eng.cam.ac.uk/help/tpl/programs/Matlab/faster_scripts.html>

[12] Low, L.A., Reinhall, P.G., Storti, D.W., and Goldman, E.B., “Coupled van der Pol oscillators as a simplified model for generation of neural patterns for jellyfish locomotion.” *Struct. Control Health Monit.* 13 (2006): 417-429.

[13] Moore-Ede, M.C., Sulzman, F.M., and Fuller, C.A., *The Clocks That Time Us – Physiology of the Circadian Timing System.* Harvard University Press, Cambridge, Massachusetts, 1982.

[14] Nayfeh, A.H. and Mook, D.T., *Nonlinear Oscillations.* John Wiley & Sons, New York, New York, 1979.

[15] Polking, John C. *ODE Software for MATLAB.* Last Updated: 23 April 2002. Accessed: 31 Mar 2008. <http://math.rice.edu/∼dfield/>.

[16] Rand, R.H. and Holmes, P.J., "Bifurcation of Periodic Motions in Two Weakly Coupled van der Pol Oscillators." *Int. J. Nonlinear Mechanics* 15 (1980): 387-399.

[17] Rand, R.H., *Lecture notes in nonlinear vibrations (version 45).* The Internet-First University Press, Ithaca, New York, 2004. <http://dspace.library.cornell.edu/handle/1813/79>.

[18] Rompala, K., Rand, R.H., and Howland, H., "Dynamics of Three Coupled van der Pol Oscillators with Application to Circadian Rhythms." *Proceedings of the 2005 ASME International Design Engineering Technical Conferences, Sept.24-28, 2005, Long Beach, CA*, paper no. DETC2005-84017.

[19] Rompala, K., *Dynamics of Three Coupled van der Pol Oscillators with Application to Circadian Rhythms.* Masters thesis, Cornell University, 2006.

[20] Rompala, K., Rand, R.H., and Howland, H., "Dynamics of Three Coupled van der Pol Oscillators with Application to Circadian Rhythms." *Comm. Nonlinear Sci. Num. Sim.* 12 (2007): 794-803.

[21] Smith, W., *MATLAB Central File Exchange - Vector norm.* MATLAB Central File Exchange. Accessed 31 Mar 2008. <http://www.mathworks.com/matlabcentral/fileexchange/loadFile.do?objectId=10708&objectType=File>

[22] Steele, C.T., Zivkovic, B.D., Sipoes, T., and Underwood, H., "Ocular clocks are tightly coupled and act as pacemakers in the circadian system of Japanese quail." *Am. J. Physiol. Regul. Integrat. Comp. Physiol.* 284 (2003): R208-R218.

[23] Storti, D.W., *A Study of the Motions of Two Strongly Coupled van der Pol Oscillators.* Masters thesis, Cornell University, 1981.

[24] Storti, D.W. and Rand, R.H., "Dynamics of Two Strongly Coupled Van der Pol Oscillators." *Int. J. Nonlinear Mechanics* 17 (1982): 143-152.

[25] Strogatz, S.H., *Nonlinear Dynamics and Chaos: With Applications to Physics, Biology, Chemistry, and Engineering*. Perseus Books, Cambridge, Massachusetts, 1994.

[26] Underwood, H., Binkley, S., Siopes, T., and Mosher, K., "Melatonin rhythms in the eyes, pineal bodies, and blood of japanese quail (Coturnix coturnix japonica)." *Gen. Comp. Endocrinol.* 56 (1984): 70-81.

[27] Underwood, H., and Edmonks, K., "The circadian rhythm of thermoregulation in Japanese quail. III. Effects of melatonin administration." *J. Bio. Rhy.* 10 (1985): 284-298.

[28] Underwood, H., Steele, C.T., and Zivkovic, B., "Circadian Organization and the Role of the Pineal in Birds." *Microsc. Res. Tech.* 53 (2001): 48-62.

[29] Wu, H., Lu, J., and Bai-Lian, L., "A Coupled Oscillatory Model Mimicking Avian Circadian Regulatory Systems." *J. Biol. Phys.* 26 (2000): 261-272.